

# A Physics-compatible solver for turbidity currents

G. Gonzalez de Diego

Technische Universiteit Delft



# A PHYSICS-COMPATIBLE SOLVER FOR TURBIDITY CURRENTS

by

**G. Gonzalez de Diego**

in partial fulfillment of the requirements for the degree of

**Master of Science**  
in Aerodynamics and Wind Energy  
at the Delft University of Technology.

Supervisors:	Dr. ir. M.I. Gerritsma	TU Delft
	Dr. ir. A. Palha da Silva Clérigo,	TU Eindhoven
Thesis committee:	Prof. dr. S. Hickel,	TU Delft
	Dr. S. J. Hulshoff,	TU Delft
	Dr. ir. C. J. Simao Ferreira	TU Delft

*This thesis is confidential and cannot be made public until December 31, 2017.*

An electronic version of this thesis is available at <http://repository.tudelft.nl/>.



# PREFACE

Working on this thesis over the last year has introduced me into the fascinating world of physics-compatible methods. The guidance of Marc and Artur could not have been better. The freedom that my supervisors have given me to investigate on my own account has allowed me to start developing a scientific mindset and to value the beauty of numerical analysis. This would not have been possible without their knowledge, their dedication and the value they have given to my work. I am extremely grateful for all of this.

Working in Aerospace would have been real boring without the basement and its company. I thank you all, not only for being the necessary distraction that every hard endeavor needs, but also for the fascinating/geeky chats we've had.

To Anisa, I thank you for your love and care. To my father, my sister and my grandmother, your love and support remains unforgotten.

*G. Gonzalez de Diego  
Delft, May 2017*



# ABSTRACT

Turbidity currents are an essential agent of sediment transport from shallow to deeper waters. Detailed measurements of the velocity field or particle concentration are only available by means of accurate numerical simulations. In this thesis, a DNS solver for turbidity currents is presented based on the MEEVC scheme, a mass, energy, enstrophy and vorticity conserving solver for the 2D incompressible Navier-Stokes equations with periodic boundary conditions. The construction of the solver consists of two separate steps: the prescription of slip boundary conditions and the implementation of a transport equation for the particle phase.

Tangential velocity boundary conditions cannot be imposed strongly because the velocity is sought in the function space  $H(\text{div})$ . To this end, three methods are proposed for the weak enforcement of the tangential velocity component by means of vorticity boundary conditions. Of these methods, kinematic Neumann boundary conditions prove to be the most effective and are used for the construction of a turbidity current solver. An equilibrium Eulerian approach for the particle phase is implemented and the resulting solver is proved to satisfy the discrete energy balance equations up to a residual. This residual does not accumulate over time and no artificial dissipation of energy is introduced into the system. The 2D lock exchange test case is computed and comparisons are made with reference results. The numerical results indicate that the solver is capable of capturing the essential dynamics of the flow in coarse grids.



# CONTENTS

<b>1</b>	<b>Introduction</b>	<b>1</b>
1.1	Turbidity currents . . . . .	1
1.2	Physics-compatible methods . . . . .	1
1.3	The MEEVC scheme. . . . .	2
1.4	Objective and scope of the thesis . . . . .	3
1.5	Methodology . . . . .	3
1.5.1	The FEniCS project . . . . .	3
<b>2</b>	<b>Prescription of boundary conditions</b>	<b>5</b>
2.1	Introduction . . . . .	5
2.1.1	Prescription of vorticity boundary conditions . . . . .	5
2.1.2	Overview of this chapter . . . . .	6
2.2	Formulation of the problem. . . . .	6
2.2.1	Formulation of the Navier-Stokes equations . . . . .	6
2.2.2	Weak formulation . . . . .	7
2.2.3	Normal velocity boundary conditions . . . . .	7
2.2.4	Vorticity boundary conditions . . . . .	7
2.3	Spatial discretization . . . . .	9
2.4	Temporal discretization. . . . .	11
2.5	Numerical schemes . . . . .	12
2.5.1	MEEVC with kinematic Dirichlet boundary conditions . . . . .	12
2.5.2	MEEVC with kinematic Neumann boundary conditions . . . . .	13
2.5.3	MEEVC with dynamic Neumann boundary conditions . . . . .	13
2.6	Conservation properties . . . . .	13
2.6.1	Conservation of mass . . . . .	14
2.6.2	Conservation of vorticity. . . . .	14
2.6.3	Conservation of kinetic energy. . . . .	15
2.6.4	Conservation of enstrophy. . . . .	15
2.7	Numerical test cases . . . . .	16
2.7.1	Taylor-Green vortex. Order of accuracy of the schemes. . . . .	16
2.7.2	Dipole Collision . . . . .	17
2.8	Concluding remarks . . . . .	23
<b>3</b>	<b>Development of a solver for turbidity currents</b>	<b>25</b>
3.1	Introduction . . . . .	25
3.1.1	High-resolution computations of turbidity currents . . . . .	25
3.1.2	Overview of this chapter . . . . .	25
3.2	Modeling considerations . . . . .	25
3.2.1	Modeling possibilities for dilute suspensions . . . . .	26
3.2.2	Equilibrium Eulerian equations for a dilute suspension . . . . .	27
3.3	The 2D lock exchange flow . . . . .	28
3.3.1	Boundary conditions. . . . .	29
3.4	Finite element discretization . . . . .	30
3.5	Energy balance . . . . .	32
3.5.1	Conservation of energy at the continuous level . . . . .	32
3.5.2	Conservation of energy at the discrete level . . . . .	33
3.6	Numerical results . . . . .	35
3.7	Concluding remarks . . . . .	38

<b>4</b>	<b>Conclusions and further research</b>	<b>41</b>
4.1	Prescription of slip boundary conditions . . . . .	41
4.2	Development of a solver for turbidity currents . . . . .	42
<b>A</b>	<b>A compatibility condition for kinematic Neumann boundary conditions</b>	<b>43</b>
A.1	Implementation . . . . .	43
A.2	Numerical test case. The dipole collision. . . . .	44
<b>B</b>	<b>An alternative <math>(\vec{u}, \omega, p)</math> formulation. Comparison with the MEEVC scheme.</b>	<b>45</b>
B.1	Description of the alternative $(\vec{u}, \omega)$ formulation. Discretization and conservation properties. . .	45
B.2	The dipole collision . . . . .	46
<b>C</b>	<b>Tabulated results.</b>	<b>49</b>
C.1	Dipole collision. Comparison of approaches for the prescription of vorticity boundary conditions for the MEEVC scheme. . . . .	49
C.2	Dipole collision. Comparison of the MEEVC and alt scheme. . . . .	50
	<b>Bibliography</b>	<b>53</b>

# 1

## INTRODUCTION

The origin of this project can be traced back to a request from the Applied Geology department for a numerical solver for turbidity currents. The conservation properties of the MEEVC scheme, a *physics-compatible* numerical scheme for 2D incompressible flow, made it an ideal candidate from which to build a solver for turbidity currents. This project consists in the extension of the MEEVC scheme to solve the 2D incompressible Navier-Stokes equations coupled with a transport equation for the particle phase in wall-bounded domains.

In this chapter, a description is given of turbidity currents and physics-compatible discretizations. Subsequently, the MEEVC scheme is introduced and a brief explanation of why it is considered a physics-compatible method is given. The next section explains the objectives and the scope of the thesis. Finally, a section on methodology is included.

### 1.1. TURBIDITY CURRENTS

A turbidity current is a particle-laden flow which is driven by the density differences caused by spatial variations of the particle concentration. The particles are typically immersed in water and are suspended by the fluid's turbulence. Turbidity currents are important in many areas of geophysics because they represent an essential agent of sediment transport from shallow to deeper water. In a more industrial context, turbidity currents receive attention due to the fact that the deposits of turbidity currents, also known as turbidites, form an important class of hydrocarbon reservoirs [1].

Turbidity currents and more general gravity currents have been modeled following a wide variety of approaches that range from simple conceptual models to full-scale Navier-Stokes equations coupled with a further set of equations that account for the particle phase [2].

### 1.2. PHYSICS-COMPATIBLE METHODS

Physics-compatible (or structure-preserving) methods can be defined as numerical methods that aim to preserve a set of qualitative and global features of a differential equation when it is discretized, such as conservation laws or symmetries. In contrast with the more traditional approach to numerical analysis, in which a scheme is constructed with the objective of keeping local truncation errors as low as possible, the discrete dynamical system which results from a physics-compatible method can have the same properties as its continuous counterpart [3].

For the specific case of the incompressible Navier-Stokes equations, the physics of the system are described in terms of conservation laws; for the case of the primitive  $(\vec{u}, p)$  formulation, the equations correspond with conservation of mass and momentum. The physical fidelity of a numerical solver will depend on its capability to represent conservation laws correctly. For example, turbulent flow computations require an accurate reproduction of the energy cascade and, to this end, conservation of kinetic energy in the inviscid limit is fundamental, for both DNS [4] and LES [5] simulations.

Over the years, many different approaches have been proposed for the construction of discrete conservation statements, such as staggered methods and skew-symmetrization of the convective operator [6]. Staggered mesh methods, first introduced by Harlow and Welch [7], distribute different variables over different locations of the mesh. Staggered methods can yield discrete conservation statements of primary and secondary variables in both structured and unstructured meshes [6]. Preserving the skew-symmetry of the con-

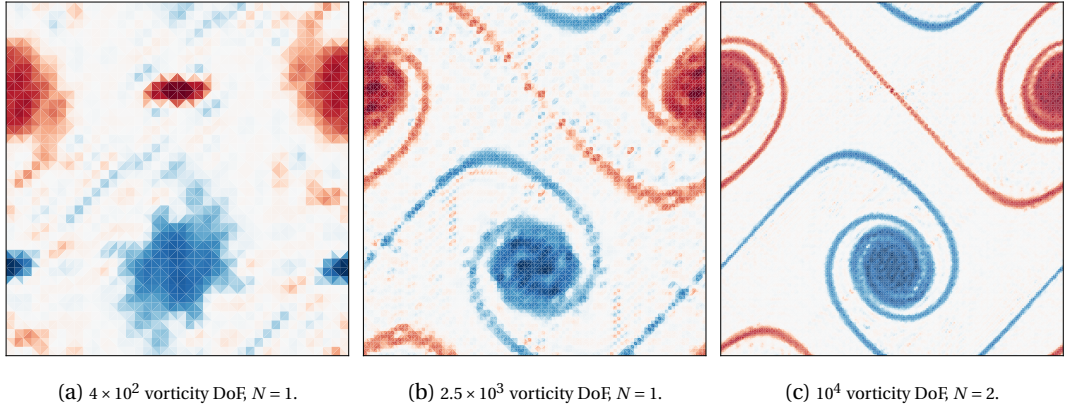


Figure 1.1: Vorticity distribution at  $t = 8$  of the inviscid vortex roll-up test case, see [11] for more details. The results have been computed with increasing polynomial order  $N = 2$  and degrees of freedom (DoF).

vection operator at the discrete level is a fundamental requirement for kinetic energy conservation [4]. Given a discrete convection operator  $\mathcal{C}_h$ , its adjoint will correspond with  $\mathcal{C}_h^T = -\mathcal{C}_h$  if skew-symmetry is preserved, such that the artificial dissipation of energy due to convection will be zero.

Staggering and skew-symmetrization of the convection operator are examples of discretizations which are capable of preserving certain properties of the continuous system. However, in many cases, the underlying structure of a continuous system can be much more obscure and constructing a stable discretization will require further insight into geometrical or variational aspects that govern the partial differential equation [8]. To this end, different approaches to staggering or skew-symmetrization have been developed for capturing the structure of a differential equation; a notable example which is relevant to this work are mimetic methods.

Mimetic methods can be considered a particular subclass of physics-compatible methods which describe the continuous and discrete differential models in terms of differential geometry and algebraic topology, respectively [9, 10]. Furthermore, mimetic methods identify the metric-free part of the differential models which can be discretized exactly. The use of differential forms for describing the field variables distinguishes scalar quantities associated to nodes or cells from vector quantities, recognizing that these should be treated in a fundamentally different manner when discretized. These geometrical aspects are encoded in differential complexes, such as the de Rham complex.

### 1.3. THE MEEVC SCHEME

The mass, energy, enstrophy and vorticity conserving (MEEVC) mimetic spectral element method for the 2D incompressible Navier-Stokes equations for unstructured simplicial meshes was presented by Palha and Gerritsma [11]. These conservation properties are possible due to the use of a  $(\vec{u}, \omega, p)$  formulation of the Navier-Stokes equations in the rotational form, a combination of finite element spaces that satisfy the divergence-free nature of the velocity field and a conserving time integrator.

Different aspects of physics-compatible discretizations are brought together in the construction of the MEEVC scheme. From a *structural* point of view, the mimetic framework establishes the appropriate function spaces in which to seek the vorticity  $\omega$ , velocity  $\vec{u}$  and pressure  $p$  such that a discrete complex of function spaces, analogous to the de Rham complex of differential forms, can be established. From the point of view of the *formulation*, the convective terms are written in such a way that artificial dissipation of energy and enstrophy is eliminated. Finally, in order to maintain the properties of the spatial discretization when integrating in time, a conserving temporal discretization is used.

As a result, the MEEVC scheme is a robust and accurate solver for 2D incompressible flow problems. Figure 1.1 shows the vorticity distribution of 3 computations of the vortex roll-up with increasing refinement. This test case consists in a shear layer that rolls up and it is considered a challenging solution because of the large vorticity gradients that are developed [11]. Figure 1.1 indicates that for very coarse grids, the MEEVC scheme is still capable of capturing the essential dynamics of the problem without any *blow up* occurring.

## 1.4. OBJECTIVE AND SCOPE OF THE THESIS

The main objective of this project is to develop a solver capable of computing the fluid motion of a turbidity current. The initial results obtained with the MEEVC scheme suggest that its stability and its robustness make it an ideal scheme for the computation of more complex flows. The exact conservation of mass and kinetic energy are particularly important when considering gravity currents because the conversion of potential to kinetic energy is a fundamental mechanism [12]. Furthermore, due to the use of unstructured meshes, the MEEVC scheme can easily accommodate to a complex geometry.

The extension of the MEEVC scheme is carried out in two separate steps. First, a method for prescribing velocity boundary conditions must be proposed; in [11], the MEEVC scheme has only been tested in domains with periodic boundary conditions and, as will be shown in Chapter 2, imposing velocity boundary conditions is not straightforward. The second part consists of the selection and implementation of a mathematical model for particle-laden currents based on the incompressible Navier-Stokes equations that can capture the essential features of a turbidity current. Therefore, the research to be carried out in this project can be divided into two separate parts:

- Prescription of arbitrary no penetration, slip boundary conditions. The difficulty of prescribing boundary conditions for the MEEVC scheme is due to the approximation of the velocity  $\vec{u}$  in a finite subset of the Sobolev space  $H(\text{div}, \Omega)$ , defined as the space of square integrable functions whose divergence is also square integrable over the domain  $\Omega$ . This condition is translated into the fact that the degrees of freedom of the discrete velocity are based on the fluxes of  $\vec{u}$  across the faces of the elements and only  $\vec{u} \cdot \vec{n} = 0$  can be strongly prescribed on the boundary  $\partial\Omega$ . Therefore, tangential velocity boundary conditions must be imposed weakly through vorticity boundary conditions. To this end, three methods are proposed and compared in two test cases to evaluate their effectiveness for imposing velocity boundary conditions.
- Development of a solver for turbidity currents. Once an appropriate method for the prescription of boundary conditions has been selected, a model is chosen for the computation of particle-laden currents. A simple model based on the Boussinesq equations is chosen and a lock exchange flow is computed. The energy conserving properties of the resulting solver are studied, detailed results are presented and comparison are made with reference results from the literature.

## 1.5. METHODOLOGY

The finite element discretizations presented in this thesis have been computed in Python using the set of libraries included in the FEniCS project, a tool which is explained below. Additionally, the mesh generator gmsh [13] has been used for the generation of unstructured simplicial meshes. Computations were carried out on a desktop computer with a 3.47GHz Intel Xeon processor, a 16GB RAM and a NVIDIA Quadro 2000 GPU with 1GB RAM.

### 1.5.1. THE FENICS PROJECT

The FEniCS project has brought together a set of C++ and Python libraries for the automated generation of finite element algorithms, resulting in a versatile tool for solving PDEs [14]. A simple interface is provided in which a general PDE, linear or non-linear, can easily be assembled into an algebraic system of equations. Furthermore, the set of finite elements implemented in FEniCS include  $H(\text{div})$  and  $H(\text{curl})$  conforming elements, making FEniCS particularly suitable for mixed finite element methods.

FEniCS consists in the core components DOLFIN, FFC, FIAT, Instant, UFC and UFL. A brief overview of these components is given below:

- DOLFIN is a C++/Python library that works as the main user interface of FEniCS. It is structured as a collection of libraries which include linear and non-linear solvers and a mesh generator. Essentially, when using Python, DOLFIN is the only module which is explicitly imported.
- The finite element discretization of variational forms and functionals are declared in UFL (unified form language). Finite element spaces and weak formulations of PDEs can be defined in this language using a notation very similar to mathematical notation.
- The assembly of algebraic linear systems is carried out with the tool chain FIAT-UFC-FFC:

1. FFC, an automated form compiler, generates a code for the construction of the element tensor, which contains the contribution from each cell, and the local to global mapping. It takes a UFL form as input and generates a C++ code that conforms to the UFC language.
2. The linear system is assembled in the UFC (unified form-assembly code) interface, which consists of a set of abstract C++ classes. The code generated in FFC, together with mesh data, are taken as input. The contributions from the cells, exterior facets and interior facets are assembled in separate stages, resulting in a final tensor.

Throughout the assembly process, FIAT is used for the implementation of the mathematical framework for constructing a general reference finite element in terms of numerical algebra. Furthermore, in FFC, Instant is used for just-in-time compilation of C/C++ code.

- The resulting linear system can be solved using one of the direct or iterative methods implemented in DOLFIN or in PETSc, a third party library used in FEniCS.

# 2

## PRESCRIPTION OF BOUNDARY CONDITIONS

### 2.1. INTRODUCTION

When considering boundary conditions for the MEEVC scheme, prescribing the tangential velocity along the boundary is not straightforward. The velocity vector  $\vec{u}$  is sought in the function space  $H(\text{div}, \Omega)$ , the space of vector fields whose divergence is square-integrable. When considering a finite element approximation of  $H(\text{div}, \Omega)$ , square integrability of the divergence field translates into continuity of the normal components of the discrete velocity  $\vec{u}_h$  along the interfaces of the elements [15].

As a consequence, the degrees of freedom of finite element spaces of  $H(\text{div}, \Omega)$  measure the *fluxes* of  $\vec{u}$  across the edges of the elements, without ensuring continuity of the tangential components of  $\vec{u}$ . Therefore, strong prescription of tangential boundary conditions is impossible and, as will be shown in this chapter, tangential velocity boundary conditions must be imposed weakly by means of vorticity boundary conditions. This difficulty was avoided in the first paper [11] by computing flow problems with periodic boundary conditions.

#### 2.1.1. PRESCRIPTION OF VORTICITY BOUNDARY CONDITIONS

A brief literature review is presented in this section which contains references from which the author drew inspiration for the development of these methods. The problem of vorticity boundary conditions arises in many different numerical solvers and remains a long-standing dilemma in computational fluid dynamics. Many different possibilities have been investigated over the past decades, although no consensus has been reached as to whether vorticity boundary conditions should be of Dirichlet or Neumann type, if they should be local or global (integral) or if they should be related to the more natural velocity boundary conditions by means of kinematic or dynamic relations [16–18].

From a historical point of view, Lighthill's analysis of vorticity creation along solid walls [19] set the standard for different vorticity schemes: tangential velocity boundary conditions are intimately related to the strength of a thin vortex sheet generated along the solid surface. The strength of these vortex sheets can be calculated as a correction to the slip velocity which results from a potential flow solution (see Chorin [20] and J.C. Wu [21] for implementations). An important point raised by Lighthill and treated in various theoretical analyses [22, 23] is the relationship between vorticity generation and the tangential pressure gradient along a solid wall. J.Z. Wu et al. [24] implement vorticity boundary conditions following this line of reasoning and come to the conclusion that vorticity generation along the boundary must be calculated as a flux.

More in line with the current work, the problem of assigning boundary conditions in the vorticity arises when considering finite element solvers for the fully resolved Navier-Stokes equations in a velocity-vorticity form. Unlike the work presented in this document, most of the solvers presented in the literature use Taylor-Hood elements [25] and seek the velocity field in a subset of  $(H^1(\Omega))^n$ , with  $n = 2$  or  $3$ ; as a consequence both the normal and the tangential velocity components can be prescribed strongly but mass conservation cannot be satisfied exactly. Use of the vorticity transport equation requires the prescription of Dirichlet [26–30] or Neumann vorticity boundary conditions [31, 32]. Furthermore, an alternative that can be found in the literature is the weak prescription of the kinematic definition of  $\omega$  by means of a penalty method [33].

### 2.1.2. OVERVIEW OF THIS CHAPTER

Section 2.2 presents the formulation of the incompressible Navier-Stokes equations used in the MEEVC scheme and three different methods are proposed for the prescription of vorticity boundary conditions. Sections 2.3 and 2.4 present the derivation of the MEEVC scheme with boundary conditions and Section 2.5 gives a summary of the three fully discretized, modified MEEVC schemes. The conservation properties of these methods are analysed in Section 2.6 and numerical test cases are computed in Section 2.7.

## 2.2. FORMULATION OF THE PROBLEM

In this section, the weak formulation of the 2D incompressible Navier-Stokes equations is constructed and the problem of prescribing tangential boundary conditions is addressed. It is shown that the boundary conditions for the vorticity transport equation must be related to the tangential velocity along the boundary. Finally, three different methods are presented that enable the prescription of tangential velocity boundary conditions by means of vorticity boundary conditions.

### 2.2.1. FORMULATION OF THE NAVIER-STOKES EQUATIONS

Two-dimensional viscous incompressible flows are modeled by the Navier-Stokes equations, defined on a domain  $\Omega \subset \mathbb{R}^2$ . These equations are generally expressed in the so-called primitive form, based on the equations for conservation of momentum and of mass, and solve for the flow velocity  $\vec{u}$  and pressure  $p$ :

$$\begin{cases} \frac{\partial \vec{u}}{\partial t} + (\vec{u} \cdot \nabla) \vec{u} + \nabla p = \nu \Delta \vec{u}, \\ \nabla \cdot \vec{u} = 0, \end{cases} \quad (2.1)$$

where  $\nu$  is the kinematic viscosity and  $\Delta$  is the Laplace operator. In this work, the following no penetration, slip boundary conditions will be considered:

$$\vec{u} \cdot \vec{n} = 0, \quad \vec{u} \times \vec{n} = g(x, t), \quad \text{on } \partial\Omega, \quad (2.2)$$

with  $\vec{n}$  the outward normal vector defined along the boundary of the domain,  $\partial\Omega$ , and  $g(t)$  is a prescribed slip velocity along  $\partial\Omega$ . In this work, the cross product is defined as a bilinear mapping  $\times : \mathbb{R}^2 \times \mathbb{R}^2 \mapsto \mathbb{R}$  resulting in a real scalar function which, in practical terms, represents a ‘‘perpendicular’’ scalar product of two vectors. For  $\vec{a}, \vec{b} \in \mathbb{R}^2$  with components  $\vec{a} = (a_x, a_y)$  and  $\vec{b} = (b_x, b_y)$ , the cross product yields  $\vec{a} \times \vec{b} = a_x b_y - a_y b_x$ .

Equation (2.1) can be written in a variety of different formulations which usually require the non-linear term to be written in a different manner or introduce the vorticity, defined  $\omega = \nabla \times \vec{u}$ , as an additional variable [16, 17]. All of these alternative formulations are equivalent at the continuous level; however, once the equations are discretized, certain vector calculus identities may no longer hold. Therefore, a fundamental point that must be taken into account is that each of these formulations leads to different discretizations of the Navier-Stokes equations with different properties [34].

The formulation used in the MEEVC scheme [11] is a combination of the momentum equation in the rotational form and the vorticity transport equation in the skew-symmetric form:

$$\begin{cases} \frac{\partial \vec{u}}{\partial t} + \omega \times \vec{u} + \nabla \bar{p} = -\nu \nabla \times \omega, \\ \frac{\partial \omega}{\partial t} + \frac{1}{2} (\vec{u} \cdot \nabla) \omega + \frac{1}{2} \nabla \cdot (\vec{u} \omega) = \nu \Delta \omega, \\ \nabla \cdot \vec{u} = 0. \end{cases} \quad (2.3)$$

where  $\bar{p} := p + \frac{1}{2} \vec{u} \cdot \vec{u}$  is the total pressure, also referred to as the Bernoulli pressure [31].

Equation (2.3) was also used by Heister et al. [32] for the construction of a finite element discretization of the 2D incompressible Navier-Stokes equations; a similar formulation for the 3D equations is used by Benzi et al. [30] and by Lee et al. [29]. The main advantage of this formulation is that the rotational and the skew-symmetric forms of the non-linear terms will not introduce numerical dissipation of kinetic energy and enstrophy, respectively, when used together with exactly divergence-free velocity fields. Furthermore, this formulation allows for the decoupling of the vorticity equation by means of a staggered time integrator.

### 2.2.2. WEAK FORMULATION

The construction of a the finite element discretization of (2.3) requires this equation to be written in its weak form. Prior to the application of slip boundary conditions, the following weak form is obtained:

$$\left\{ \begin{array}{l} \text{Find } \vec{u} \in H(\text{div}, \Omega), p \in L^2(\Omega) \text{ and } \omega \in H(\text{curl}, \Omega) \text{ such that:} \\ \langle \frac{\partial \vec{u}}{\partial t}, \vec{v} \rangle + \langle \omega \times \vec{u}, \vec{v} \rangle - \langle \bar{p}, \nabla \cdot \vec{v} \rangle + \int_{\partial\Omega} \bar{p} (\vec{v} \cdot \vec{n}) \, d\Gamma = -\nu \langle \nabla \times \omega, \vec{v} \rangle, \quad \forall \vec{v} \in H(\text{div}, \Omega), \\ \langle \frac{\partial \omega}{\partial t}, \xi \rangle - \frac{1}{2} \langle \omega, \nabla \cdot (\vec{u} \xi) \rangle + \frac{1}{2} \langle \nabla \cdot (\vec{u} \omega), \xi \rangle + \frac{1}{2} \int_{\partial\Omega} \xi \omega (\vec{u} \cdot \vec{n}) \, d\Gamma = \\ -\nu \langle \nabla \times \omega, \nabla \times \xi \rangle + \nu \int_{\partial\Omega} \xi (\nabla \times \omega) \times \vec{n} \, d\Gamma, \quad \forall \xi \in H(\text{curl}, \Omega), \\ \langle \nabla \cdot \vec{u}, q \rangle = 0, \quad \forall q \in L^2(\Omega), \end{array} \right. \quad (2.4)$$

where integration by parts has been carried out, such that

$$\begin{aligned} \langle \nabla \bar{p}, \vec{v} \rangle &= -\langle \bar{p}, \nabla \cdot \vec{v} \rangle + \int_{\partial\Omega} \bar{p} (\vec{v} \cdot \vec{n}) \, d\Gamma, \\ \langle (\vec{u} \cdot \nabla) \omega, \xi \rangle &= -\langle \omega, \nabla \cdot (\vec{u} \xi) \rangle + \int_{\partial\Omega} \xi \omega (\vec{u} \cdot \vec{n}) \, d\Gamma, \\ \langle \Delta \omega, \xi \rangle &= -\langle \nabla \times \omega, \nabla \times \xi \rangle + \int_{\partial\Omega} \xi (\nabla \times \omega) \times \vec{n} \, d\Gamma. \end{aligned} \quad (2.5)$$

In (2.4) and (2.5), the angled brackets  $\langle \cdot, \cdot \rangle$  represent the  $L^2(\Omega)$  inner product of two functions over  $\Omega$ . The function space  $L^2(\Omega)$  contains square integrable functions and the spaces  $H(\text{curl}, \Omega)$  and  $H(\text{div}, \Omega)$  contain vector functions whose curl and divergence are square-integrable, respectively.

In the theory of Sobolev spaces, the well defined restriction of a general function  $v$  to the boundary of the domain is carried out with the trace operator  $\gamma$  [35]. In more practical terms, the strong prescription of boundary conditions on  $H(\text{curl}, \Omega)$  and  $H(\text{div}, \Omega)$  is equivalent to equating the trace of its functions to a given value. Therefore, it is useful to know how the trace operator is defined for these spaces. In 3D, the traces of these vector spaces are the tangential and normal vector components at the boundary, respectively. In 2D,  $H(\text{curl}, \Omega)$  corresponds with  $H^1(\Omega)$ , and the trace is defined as the pointwise restriction to  $\partial\Omega$ , such that  $\gamma \xi = \xi|_{\partial\Omega}$  for  $\xi \in H(\text{curl}, \Omega)$ <sup>1</sup>. For  $\vec{v} \in H(\text{div}, \Omega)$ , the trace is defined  $\gamma \vec{v} = \vec{v} \cdot \vec{n}|_{\partial\Omega}$  [15].

### 2.2.3. NORMAL VELOCITY BOUNDARY CONDITIONS

Searching for the velocity vector  $\vec{u}$  in  $H(\text{div}, \Omega)$  implies weaker smoothness requirements for  $\vec{u}$  than assuming  $\vec{u} \in (H^1(\Omega))^2$ . For a finite element space to be contained in  $H(\text{div}, \Omega)$ , it is necessary for the normal vector component along each face be continuous. In general, the degrees of freedom of  $H(\text{div}, \Omega)$  conforming elements are calculated in terms of moments of the normal components of the vector along the faces [15, 36]. Thus, when considering the prescription of slip boundary conditions on  $\vec{u}$  (2.2), only  $\vec{u} \cdot \vec{n} = 0$  can be strongly enforced. Equation (2.4) takes the following form:

$$\left\{ \begin{array}{l} \text{Find } \vec{u} \in H_0(\text{div}, \Omega), p \in L^2(\Omega) \text{ and } \omega \in H(\text{curl}, \Omega) \text{ such that:} \\ \langle \frac{\partial \vec{u}}{\partial t}, \vec{v} \rangle + \langle \omega \times \vec{u}, \vec{v} \rangle - \langle \bar{p}, \nabla \cdot \vec{v} \rangle = -\nu \langle \nabla \times \omega, \vec{v} \rangle, \quad \forall \vec{v} \in H_0(\text{div}, \Omega), \\ \langle \frac{\partial \omega}{\partial t}, \xi \rangle - \frac{1}{2} \langle \omega, \nabla \cdot (\vec{u} \xi) \rangle + \frac{1}{2} \langle \nabla \cdot (\vec{u} \omega), \xi \rangle = -\nu \langle \nabla \times \omega, \nabla \times \xi \rangle + \nu \int_{\partial\Omega} \xi (\nabla \times \omega) \times \vec{n} \, d\Gamma, \quad \forall \xi \in H(\text{curl}, \Omega), \\ \langle \nabla \cdot \vec{u}, q \rangle = 0, \quad \forall q \in L^2(\Omega), \end{array} \right. \quad (2.6)$$

with  $\vec{u}$  sought in the restricted function space  $H_0(\text{div}, \Omega)$ , defined as,

$$H_0(\text{div}, \Omega) = \{ \vec{u} \in H(\text{div}, \Omega) \mid \vec{u} \cdot \vec{n} = 0 \text{ on } \partial\Omega \}. \quad (2.7)$$

### 2.2.4. VORTICITY BOUNDARY CONDITIONS

Once  $\vec{u} \cdot \vec{n} = 0$  has been strongly enforced, only vorticity boundary conditions remain to be prescribed. Equation (2.6) indicates that two possibilities exist:

<sup>1</sup>The same occurs with  $H(\text{grad}, \Omega)$ , defined further on.

1. Given a vorticity  $\omega_\Gamma$  defined on  $\partial\Omega$ , Dirichlet boundary conditions can be prescribed by formulating a non-homogeneous partial differential equation with  $\omega = \omega_\Gamma$  on  $\partial\Omega$ .
2. Neumann boundary conditions can also be given for the vorticity equation. In this case, the curl of the vorticity along the boundary  $((\nabla \times \omega) \times \vec{n})_\Gamma$  is known and the boundary integral in (2.6) can be determined.

Both the vorticity and its curl along the wall can be calculated with the kinematic condition and with the momentum equation, respectively. These two approaches are explored in the following sections.

#### KINEMATIC VORTICITY BOUNDARY CONDITIONS

The kinematic condition establishes a linear, instantaneous relation:

$$\tilde{\omega} = \nabla \times \vec{u}. \quad (2.8)$$

In this case, the vorticity is renamed  $\tilde{\omega}$  in order to distinguish it from the vorticity  $\omega$  calculated with the vorticity transport equation. Although the equality  $\tilde{\omega} = \omega$  holds at the continuous level, both vorticity values will generally differ at the discrete level; hence, distinguishing both is important when constructing the finite element approximation. Taking into account that  $\vec{u} \in H(\text{div}, \Omega)$ , the curl of  $\vec{u}$  is not defined. For this reason,  $\tilde{\omega}$  will be known as the *approximate* vorticity. In its weak form, Equation (2.8) can be written in the following manner after integrating by parts:

$$\langle \tilde{\omega}, \tilde{\xi} \rangle = \langle \vec{u}, \nabla \times \tilde{\xi} \rangle - \int_{\partial\Omega} \tilde{\xi} g(x, t) \, d\Gamma, \quad \forall \tilde{\xi} \in H(\text{curl}, \Omega), \quad (2.9)$$

where  $g(x, t) = \vec{u} \times \vec{n}$  is the slip velocity defined along  $\partial\Omega$ , see (2.2). Two approaches are suggested for the prescription of kinematic vorticity boundary conditions:

1. **Kinematic Dirichlet boundary conditions.** The approximate vorticity  $\tilde{\omega}$ , calculated with (2.9), can be strongly imposed on each of the nodes of the mesh along  $\partial\Omega$ . Formally, the resulting non-homogeneous boundary value problem is written with homogeneous boundary conditions. This can be done by setting the vorticity to  $\omega = \omega_0 + \omega'$ , with  $\omega_0 \in H_0(\text{curl}, \Omega)$ , defined

$$H_0(\text{curl}, \Omega) = \{\omega \in H(\text{curl}, \Omega) \mid \omega = 0 \text{ on } \partial\Omega\}, \quad (2.10)$$

and  $\omega'$  as any function in  $H(\text{curl}, \Omega)$  such that  $\omega' = \tilde{\omega}$  on  $\partial\Omega$ . The vorticity transport equation is solved for  $\omega_0 \in H_0(\text{curl}, \Omega)$ , such that

$$\frac{\partial \omega_0}{\partial t} + \frac{1}{2} (\vec{u} \cdot \nabla) \omega_0 + \frac{1}{2} \nabla \cdot (\vec{u} \omega_0) = \nu \Delta \omega_0 + f', \quad (2.11)$$

where

$$f' = -\frac{\partial \omega'}{\partial t} - (\vec{u} \cdot \nabla) \omega' + \nu \Delta \omega'. \quad (2.12)$$

This approach has been used extensively for the prescription of vorticity boundary conditions [26–30].

2. **Kinematic Neumann boundary conditions.** A second possibility involving the kinematic relation consists in calculating the vorticity production term with  $\tilde{\omega}$ , that is:

$$\tilde{\omega} = \nabla \times \vec{u} \rightarrow \nu \int_{\partial\Omega} \xi (\nabla \times \tilde{\omega}) \times \vec{n} \, d\Gamma \quad (2.13)$$

Well posedness of this method is not ensured. It can be proved that  $\nabla \times : H(\text{curl}, \Omega) \rightarrow H(\text{div}, \Omega)$  [11], such that  $\nabla \times \tilde{\omega} \in H(\text{div}, \Omega)$  and  $(\nabla \times \tilde{\omega}) \times \vec{n}$  on  $\partial\Omega$  is not defined. However, the vector that arises from the discretized version of the boundary integral in (2.13) can still be computed. Although computations will be carried out using kinematic Neumann boundary conditions in this chapter, understanding this point is fundamental for explaining defects and for further work.

The calculation of an additional vorticity can seem an unnatural choice, taking into account that the kinematic condition could replace the vorticity transport equation in (2.3) and tangential velocity boundary conditions could be weakly imposed without further calculations. The discretization of this alternative scheme with the same finite element spaces used for the MEEVC scheme was also investigated. Results and comparisons with the MEEVC scheme can be found in Appendix B.

### DYNAMIC VORTICITY BOUNDARY CONDITIONS

On the other hand, the momentum equation establishes a dynamic relation between the curl of  $\omega$  and the velocity which involves a non-linear term and the pressure gradient. The boundary term in (2.6), usually known as a *vorticity production* term [19, 22, 23, 31], can be written as a function of the velocity and the pressure gradient by means of the momentum equation, such that:

$$v(\nabla \times \omega) \times \vec{n} = - \left( \frac{\partial \vec{u}}{\partial t} + \omega \times \vec{u} + \nabla \bar{p} \right) \times \vec{n} \quad \text{on } \partial\Omega, \quad (2.14)$$

Using (2.2) and  $(\omega \times \vec{u}) \times \vec{n} = \omega(\vec{u} \cdot \vec{n}) = 0$ , (2.14) can be written as:

$$v(\nabla \times \omega) \times \vec{n} = - \frac{\partial \mathbf{g}}{\partial t} - \nabla \bar{p} \times \vec{n} \quad \text{on } \partial\Omega, \quad (2.15)$$

Equation (2.15) associates the vorticity production with the tangential acceleration and pressure gradient at the wall. This equation can be written in a weak form by multiplying by a test function  $\xi$  and integrating along  $\partial\Omega$ :

$$v \int_{\partial\Omega} \xi (\nabla \times \omega) \times \vec{n} \, d\Gamma = - \int_{\partial\Omega} \xi \frac{\partial \mathbf{g}}{\partial t} \, d\Gamma - \int_{\partial\Omega} \xi (\nabla \bar{p} \times \vec{n}) \, d\Gamma, \quad \forall \xi \in H(\text{curl}, \Omega). \quad (2.16)$$

A third method, similar to the method proposed by Olshanskii et al. [31] and based upon the dynamic relation given by (2.16), is suggested for prescribing vorticity boundary conditions:

3. **Dynamic Neumann boundary conditions.** The computation of the total pressure gradient  $\nabla \bar{p}$  along a solid wall presents difficulties because  $\bar{p}$  is sought in  $L^2(\Omega)$  and interelement continuity is not strongly enforced; this implies that the gradient  $\nabla \bar{p}$  is not defined [31]. In this work, an alternative method is suggested in which a total pressure  $\bar{p}$  is calculated by means of the pressure Poisson equation. If the divergence is applied to the momentum equation, the following expression can be derived,

$$\Delta \bar{p} = -\nabla \cdot (\omega \times \vec{u}). \quad (2.17)$$

In its weak form, (2.17) can take the following form: find  $\bar{p} \in H(\text{grad}, \Omega)$  such that,

$$\langle \nabla \bar{p}, \nabla \chi \rangle = \langle \nabla \cdot (\omega \times \vec{u}), \chi \rangle + \int_{\partial\Omega} \chi \nabla \bar{p} \cdot \vec{n} \, d\Gamma, \quad \forall \chi \in H(\text{grad}, \Omega), \quad (2.18)$$

where  $H(\text{grad}, \Omega)$  is the space of scalar functions with a square integrable gradient. The term  $\nabla \bar{p} \cdot \vec{n}$  remains unknown and therefore must be written in terms of the vorticity and the velocity. Taking into account that  $\vec{u} \cdot \vec{n} = 0$  along  $\partial\Omega$ , the normal component of the momentum equation restricted to the boundary is:

$$\nabla \bar{p} \cdot \vec{n} = -v(\nabla \times \omega) \cdot \vec{n} - (\omega \times \vec{u}) \cdot \vec{n} \quad \text{on } \partial\Omega. \quad (2.19)$$

If this expression for  $\bar{p} \in H(\text{grad}, \Omega)$  is substituted in (2.18) and integration by parts is performed, the pressure Poisson equation can be written in terms of  $\vec{u}$  and  $\omega$ :

$$\langle \nabla \bar{p}, \nabla \chi \rangle = -\langle \omega \times \vec{u}, \nabla \chi \rangle - v \int_{\partial\Omega} \chi (\nabla \times \omega) \cdot \vec{n} \, d\Gamma, \quad \forall \chi \in H(\text{grad}, \Omega). \quad (2.20)$$

Therefore, for a given  $\vec{u}$  and  $\omega$ , the pressure  $\bar{p} \in H(\text{grad}, \Omega)$  is calculated and used in (2.15).

## 2.3. SPATIAL DISCRETIZATION

Once the weak formulation has been constructed at the continuous level and three different approaches for the prescription of vorticity boundary conditions have been suggested, the next step in the finite element discretization of (2.3) is the spatial discretization. A general spatial discretization is performed without specifying the approach that has been taken for the vorticity boundary conditions.

The spatial discretization basically consists in the selection of stable finite element spaces for the discrete velocity  $\vec{u}_h$ , pressure  $\bar{p}_h$  and vorticity  $\omega_h$ :

$$\vec{u}_h \in U_h \subset H_0(\text{div}, \Omega), \quad \bar{p}_h \in Q_h \subset L^2(\Omega) \quad \text{and} \quad \omega_h \in W_h \subset H(\text{curl}, \Omega). \quad (2.21)$$

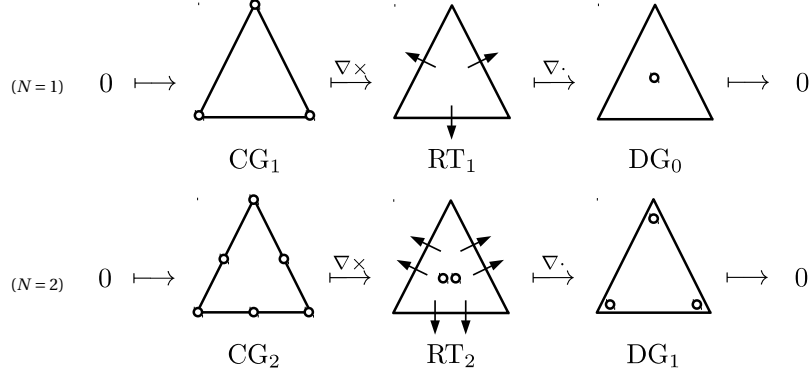


Figure 2.1: Schemes of the finite element sequences used for  $N = 1$  and  $N = 2$ . The degrees of freedom have been marked with circles to indicate point-wise or face-wise evaluation and with arrows to indicate integration through an edge.

In the MEEVC scheme, the velocity finite element space is set to  $U_h = \text{RT}_{0,N} = \{\tilde{u}_h \in \text{RT}_N \mid \tilde{u}_h \cdot \vec{n} = 0 \text{ on } \partial\Omega\}$ , where  $\text{RT}_N$  designates the Raviart-Thomas element of degree  $N$  [15, 36]. The vorticity finite element space is set to the Lagrange elements of degree  $N$ ,  $W_h = \text{CG}_N$ , and the pressure space to the discontinuous Lagrange elements of degree  $N - 1$ ,  $Q_h = \text{DG}_{N-1}$ , [36]. These finite elements are defined on rectilinear triangles of arbitrary shape, see Figure 2.1. It must be noted that  $\text{DG}_N$  elements are defined like Lagrange elements for  $N \geq 1$  but with degrees of freedom internal to the element; that is, no interelement continuity is enforced. This is reflected in Figure 2.1 by placing the degrees of freedom of  $\text{DG}_1$  inside the element, near the nodes.

This combination of finite element spaces can be proved to form a Hilbert subcomplex in which the differential operators  $\nabla \times$  and  $\nabla \cdot$  map the elements of each space into the subsequent space, see [11]. That is,

$$0 \longrightarrow W_h \xrightarrow{\nabla \times} U_h \xrightarrow{\nabla \cdot} Q_h \longrightarrow 0. \quad (2.22)$$

A discrete subcomplex mimics essential structural properties of the continuous differential equation and therefore its construction is an important requirement for stability and accuracy in a finite element scheme [10]. In this case, two important consequences are the satisfaction of the LBB stability condition [15] and the exact satisfaction of the divergence free constraint for the discrete velocity field  $\tilde{u}_h$ .

Each of the finite element spaces have an associated set of finite basis functions,

$$U_h = \text{span}\{\vec{e}_1^U, \dots, \vec{e}_{d_U}^U\}, \quad Q_h = \text{span}\{e_1^Q, \dots, e_{d_Q}^Q\} \quad \text{and} \quad W_h = \text{span}\{e_1^W, \dots, e_{d_W}^W\}, \quad (2.23)$$

where  $d_U$ ,  $d_Q$  and  $d_W$  denote the number of degrees of freedom of each finite element space. The discrete solutions  $\tilde{u}_h$ ,  $\bar{p}_h$  and  $\omega_h$  can be expressed as a linear combination of the basis functions

$$\tilde{u}_h = \sum_{i=1}^{d_U} u_i \vec{e}_i^U, \quad \bar{p}_h = \sum_{i=1}^{d_Q} p_i e_i^Q \quad \text{and} \quad \omega_h = \sum_{i=1}^{d_W} \omega_i e_i^W. \quad (2.24)$$

The coefficients  $u_i$ ,  $p_i$  and  $\omega_i$  are the degrees of freedom of velocity, total pressure and vorticity respectively. In the case of an unsteady flow, these coefficients will be time dependent.

The finite element discretization of (2.3) consists of solving the following weak formulation:

$$\left\{ \begin{array}{l} \text{Find } \tilde{u}_h \in \text{RT}_N, \bar{p}_h \in \text{DG} \text{ and } \omega_h \in \text{CG}_N \text{ such that:} \\ \langle \frac{\partial \tilde{u}_h}{\partial t}, \vec{v}_h \rangle + \langle \omega_h \times \tilde{u}_h, \vec{v}_h \rangle - \langle \bar{p}_h, \nabla \cdot \vec{v}_h \rangle = -\nu \langle \nabla \times \omega_h, \vec{v}_h \rangle, \quad \forall \vec{v}_h \in \text{RT}_{N,0}, \\ \langle \frac{\partial \omega_h}{\partial t}, \xi_h \rangle - \frac{1}{2} \langle \omega_h, \nabla \cdot (\tilde{u}_h \xi_h) \rangle + \frac{1}{2} \langle \nabla \cdot (\tilde{u}_h \omega_h), \xi_h \rangle = \\ -\nu \langle \nabla \times \omega_h, \nabla \times \xi_h \rangle + \nu \int_{\partial\Omega} \xi_h (\nabla \times \omega_h) \times \vec{n} \, d\Gamma, \quad \forall \xi_h \in \text{CG}_N, \\ \langle \nabla \cdot \tilde{u}_h, q_h \rangle = 0, \quad \forall q_h \in \text{DG}_{N-1}. \end{array} \right. \quad (2.25)$$

The expansions for  $\tilde{u}_h$ ,  $\bar{p}_h$  and  $\omega_h$  can be introduced in order to write (2.25) in a more compact form. Given the vectors  $\mathbf{u} := [u_1, \dots, u_{d_U}]^T$ ,  $\mathbf{p} := [p_1, \dots, p_{d_Q}]^T$  and  $\boldsymbol{\omega} := [\omega_1, \dots, \omega_{d_W}]^T$ , (2.25) can be written in the

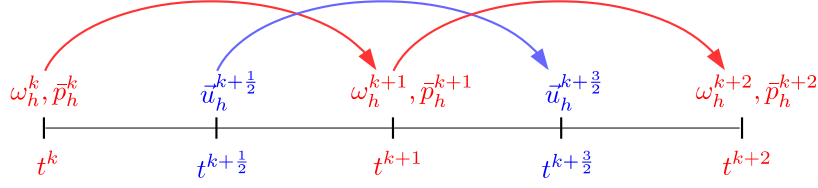


Figure 2.2: Diagram of the staggered time step used in the MEEVC scheme.

matrix form:

$$\begin{cases} \text{Find } \mathbf{u} \in \mathbb{R}^{d_U}, \bar{\mathbf{p}}_h \in \mathbb{R}^{d_Q} \text{ and } \boldsymbol{\omega} \in \mathbb{R}^{d_W} \text{ such that:} \\ \mathbf{M} \frac{d\mathbf{u}}{dt} + \mathbf{R}\mathbf{u} - \mathbf{P}\bar{\mathbf{p}} = -\nu \mathbf{l}, \\ \mathbf{N} \frac{d\boldsymbol{\omega}}{dt} - \frac{1}{2} \mathbf{W}\boldsymbol{\omega} + \frac{1}{2} \mathbf{W}^T \boldsymbol{\omega} = -\nu \mathbf{L}\boldsymbol{\omega} + \nu \mathbf{n}, \\ \mathbf{D}\mathbf{u} = 0. \end{cases} \quad (2.26)$$

The momentum equation is written in terms of the matrices  $\mathbf{M}$ ,  $\mathbf{R}$ ,  $\mathbf{P}$  and of the column vector  $\mathbf{l}$ . The coefficients of these arrays are given by

$$\mathbf{M}_{ij} := \langle \bar{\mathbf{e}}_j^U, \bar{\mathbf{e}}_i^U \rangle, \mathbf{R}_{ij} := \langle \boldsymbol{\omega}_h \times \bar{\mathbf{e}}_j^U, \bar{\mathbf{e}}_i^U \rangle, \mathbf{P}_{ij} := \langle \mathbf{e}_j^Q, \nabla \cdot \bar{\mathbf{e}}_i^U \rangle \text{ and } l_i := \langle \nabla \times \boldsymbol{\omega}_h, \bar{\mathbf{e}}_i^U \rangle. \quad (2.27)$$

The vorticity transport equation contains the matrices  $\mathbf{N}$ ,  $\mathbf{W}$ ,  $\mathbf{L}$  and the column vector  $\mathbf{n}$ , whose coefficients are given by

$$\mathbf{N}_{ij} := \langle \mathbf{e}_j^W, \mathbf{e}_i^W \rangle, \mathbf{W}_{ij} := \langle \mathbf{e}_j^W, \nabla \cdot (\bar{\mathbf{u}}_h \bar{\mathbf{e}}_i^W) \rangle, \mathbf{L}_{ij} := \langle \nabla \times \mathbf{e}_j^W, \nabla \times \mathbf{e}_i^W \rangle \text{ and } n_i := \int_{\partial\Omega} \mathbf{e}_i^W (\nabla \times \boldsymbol{\omega}_h) \times \bar{\mathbf{n}} \, d\Gamma. \quad (2.28)$$

The divergence-free constraint is written in terms of matrix  $\mathbf{D}$ , given by the coefficients

$$\mathbf{D}_{ij} := \langle \nabla \cdot \bar{\mathbf{e}}_j^U, \mathbf{e}_i^Q \rangle = \mathbf{P}^T. \quad (2.29)$$

## 2.4. TEMPORAL DISCRETIZATION

The final step in the finite element discretization of (2.3) is the temporal discretization. Once again, the approach taken for the vorticity boundary conditions is not specified.

The time integrator used in the MEEVC scheme is a first order Gauss method. This method is known to be energy-conserving when applied to the Navier-Stokes equations and time-reversible [37]. Furthermore, the first order integrator enables the construction of a staggered discretization in time. When applied to the 1D ordinary differential equation

$$\begin{cases} \frac{df}{dt} = g(f(t), t), \\ f(0) = f_0, \end{cases} \quad (2.30)$$

the first order Gauss integrator results in the implicit time stepping scheme

$$\frac{f^k - f^{k-1}}{\Delta t} = g\left(\frac{f^k + f^{k-1}}{2}, t + \frac{\Delta t}{2}\right), \quad k = 1, \dots, M, \quad (2.31)$$

where  $f^0 = f_0$ ,  $\Delta t$  is the time step and  $M$  the number of steps. This integrator is applied to the semi-discrete system of (2.26) in the following way: the vorticity  $\boldsymbol{\omega}_h$  and the total pressure  $\bar{p}_h$  are evaluated at  $t^k$ , while the velocity  $\bar{\mathbf{u}}_h$  is computed at the intermediate time instant  $t^{k+\frac{1}{2}}$ , see Figure 2.2. The resulting scheme of

equations takes the following form

$$\begin{cases} \text{Find } \mathbf{u}^{k+\frac{3}{2}} \in \mathbb{R}^{d_U}, \bar{\mathbf{p}}^{k+1} \in \mathbb{R}^{d_Q} \text{ and } \boldsymbol{\omega}^{k+1} \in \mathbb{R}^{d_W} \text{ such that:} \\ \mathbf{M} \frac{\mathbf{u}^{k+\frac{3}{2}} - \mathbf{u}^{k+\frac{1}{2}}}{\Delta t} + \mathbf{R}^{k+1} \frac{\mathbf{u}^{k+\frac{3}{2}} + \mathbf{u}^{k+\frac{1}{2}}}{2} - \mathbf{P}\bar{\mathbf{p}}^{k+1} = -\nu \mathbf{l}^{k+1}, \\ \mathbf{N} \frac{\boldsymbol{\omega}^{k+1} - \boldsymbol{\omega}^k}{\Delta t} - \frac{1}{2} \mathbf{W}^{k+\frac{1}{2}} \frac{\boldsymbol{\omega}^{k+1} + \boldsymbol{\omega}^k}{2} + \frac{1}{2} \left( \mathbf{W}^{k+\frac{1}{2}} \right)^T \frac{\boldsymbol{\omega}^{k+1} + \boldsymbol{\omega}^k}{2} = -\nu \mathbf{L} \frac{\boldsymbol{\omega}^{k+1} + \boldsymbol{\omega}^k}{2} + \nu \mathbf{n}^{k+\frac{1}{2}}, \\ \mathbf{D}\mathbf{u}^{k+\frac{3}{2}} = 0, \end{cases} \quad (2.32)$$

where the matrix operators are the same as those presented in (2.27), (2.28) and (2.29), with the exception of matrices  $\mathbf{R}^{k+1}$  and  $\mathbf{W}^{k+\frac{1}{2}}$ , defined by the coefficients

$$\mathbf{R}_{ij}^{k+1} := \langle \boldsymbol{\omega}_h^{k+1} \times \vec{e}_j^U, \vec{e}_i^U \rangle \text{ and } \mathbf{W}_{ij}^{k+\frac{1}{2}} := \langle \mathbf{e}_j^W, \nabla \cdot \left( \bar{\mathbf{u}}_h^{k+\frac{1}{2}} \vec{e}_i^W \right) \rangle, \quad (2.33)$$

and vectors  $\mathbf{l}^{k+1}$  and  $\mathbf{n}^{k+\frac{1}{2}}$ , composed of coefficients

$$l_i^{k+1} := \langle \nabla \times \boldsymbol{\omega}_h^{k+1}, \vec{e}_i^U \rangle \text{ and } n_i^{k+\frac{1}{2}} := \int_{\partial\Omega} e_i^W \left( \nabla \times \boldsymbol{\omega}_h^{k+\frac{1}{2}} \right) \times \vec{n} \, d\Gamma \quad (2.34)$$

The drawback of computing a non-linear system of equations is therefore overcome by staggering the variables in time. This implies that instead of solving a non linear system of  $d_U + d_Q + d_W$  variables that requires a series of iterations at each time iteration, only two linear systems of equations are solved, with  $d_W$  and  $d_U + d_Q$  variables each. See Figure B.4 in Appendix B for a comparison of the time required to compute a coupled scheme and the MEEVC scheme. Given the initial conditions,  $\bar{\mathbf{u}}_h^0$  and  $\boldsymbol{\omega}_h^0$ , the initial time step is required to be implicit because  $\bar{\mathbf{u}}_h^{\frac{1}{2}}$  is not known.

## 2.5. NUMERICAL SCHEMES

The three approaches for the prescription of vorticity boundary conditions suggested in Section 2.2.4 lead to 3 different numerical schemes. The resulting schemes, discretized in time and space, are presented in this section.

### 2.5.1. MEEVC WITH KINEMATIC DIRICHLET BOUNDARY CONDITIONS

Given  $\bar{\mathbf{u}}_h^{k+\frac{1}{2}}$  and  $\boldsymbol{\omega}_h^k$ ,

**Step 1.** Find  $\tilde{\boldsymbol{\omega}}_h^{k+1} \in \text{CG}_N$  such that:

$$\langle \tilde{\boldsymbol{\omega}}_h^{k+1}, \boldsymbol{\xi}_h \rangle = \langle \bar{\mathbf{u}}_h^{k+\frac{1}{2}}, \nabla \times \boldsymbol{\xi}_h \rangle - \int_{\partial\Omega} \tilde{\boldsymbol{\omega}}_h \mathbf{g}^{k+\frac{1}{2}} \, d\Gamma, \quad \forall \boldsymbol{\xi}_h \in \text{CG}_N.$$

**Step 2.** Find  $\boldsymbol{\omega}_h^{k+1} \in \text{CG}_{N,0}$  such that:

$$\begin{aligned} \left\langle \frac{\boldsymbol{\omega}_h^{k+1} - \boldsymbol{\omega}_h^k}{\Delta t}, \boldsymbol{\xi}_h \right\rangle - \frac{1}{2} \left\langle \frac{\boldsymbol{\omega}_h^{k+1} + \boldsymbol{\omega}_h^k}{2}, \nabla \cdot \left( \bar{\mathbf{u}}_h^{k+\frac{1}{2}} \boldsymbol{\xi}_h \right) \right\rangle + \frac{1}{2} \left\langle \nabla \cdot \left( \bar{\mathbf{u}}_h^{k+\frac{1}{2}} \frac{\boldsymbol{\omega}_h^{k+1} + \boldsymbol{\omega}_h^k}{2} \right), \boldsymbol{\xi} \right\rangle = \\ -\nu \left\langle \nabla \times \frac{\boldsymbol{\omega}_h^{k+1} + \boldsymbol{\omega}_h^k}{2}, \nabla \times \boldsymbol{\xi}_h \right\rangle + \langle f_h^{k+\frac{1}{2}}, \boldsymbol{\xi}_h \rangle, \quad \forall \boldsymbol{\xi}_h \in \text{CG}_{N,0}, \end{aligned}$$

with  $f_h^{k+\frac{1}{2}}$  defined as in (2.12).

**Step 3.** Find  $\left( \bar{\mathbf{u}}_h^{k+\frac{3}{2}}, \bar{\mathbf{p}}^{k+1} \right) \in (\text{RT}_{N,0}, \text{DG}_{N-1})$  such that:

$$\begin{cases} \left\langle \frac{\bar{\mathbf{u}}_h^{k+\frac{3}{2}} - \bar{\mathbf{u}}_h^{k+\frac{1}{2}}}{\Delta t}, \vec{v}_h \right\rangle + \left\langle \boldsymbol{\omega}_h^{k+1} \times \frac{\bar{\mathbf{u}}_h^{k+\frac{3}{2}} + \bar{\mathbf{u}}_h^{k+\frac{1}{2}}}{2}, \vec{v}_h \right\rangle - \langle \bar{\mathbf{p}}^{k+1}, \nabla \cdot \vec{v}_h \rangle = -\nu \langle \nabla \times \boldsymbol{\omega}_h^{k+1}, \vec{v}_h \rangle, \quad \forall \vec{v}_h \in \text{RT}_{N,0}, \\ \langle \nabla \cdot \bar{\mathbf{u}}_h^{k+\frac{3}{2}}, q_h \rangle = 0, \quad \forall q_h \in \text{DG}_{N-1}. \end{cases}$$

In Step 1, the approximate vorticity at  $t^{k+1}$  is written in terms of the velocity at  $t^{k+\frac{1}{2}}$ . Therefore, for each iteration in time, this scheme contains an explicit time integrator.

### 2.5.2. MEEVC WITH KINEMATIC NEUMANN BOUNDARY CONDITIONS

Given  $\bar{u}_h^{k+\frac{1}{2}}$  and  $\omega_h^k$ ,

**Step 1.** Find  $\tilde{\omega}_h^{k+1} \in CG_N$  such that:

$$\langle \tilde{\omega}_h^{k+\frac{1}{2}}, \tilde{\xi}_h \rangle = \langle \bar{u}_h^{k+\frac{1}{2}}, \nabla \times \tilde{\xi}_h \rangle - \int_{\partial\Omega} \tilde{\xi}_h g^{k+\frac{1}{2}} d\Gamma, \quad \forall \tilde{\xi}_h \in CG_N.$$

**Step 2.** Find  $\omega_h^{k+1} \in CG_N$  such that:

$$\begin{aligned} & \left\langle \frac{\omega_h^{k+1} - \omega_h^k}{\Delta t}, \xi_h \right\rangle - \frac{1}{2} \left\langle \frac{\omega_h^{k+1} + \omega_h^k}{2}, \nabla \cdot \left( \bar{u}_h^{k+\frac{1}{2}} \xi_h \right) \right\rangle + \frac{1}{2} \left\langle \nabla \cdot \left( \bar{u}_h^{k+\frac{1}{2}} \frac{\omega_h^{k+1} + \omega_h^k}{2} \right), \xi \right\rangle = \\ & = -\nu \langle \nabla \times \frac{\omega_h^{k+1} + \omega_h^k}{2}, \nabla \times \xi_h \rangle + \nu \int_{\partial\Omega} \xi_h \left( \nabla \times \bar{\omega}_h^{k+\frac{1}{2}} \right) \times \bar{n} d\Gamma, \quad \forall \xi_h \in CG_N. \end{aligned}$$

**Step 3.** Find  $\left( \bar{u}_h^{k+\frac{3}{2}}, \bar{p}^{k+1} \right) \in (RT_{N,0}, DG_{N-1})$  such that:

$$\begin{cases} \left\langle \frac{\bar{u}_h^{k+\frac{3}{2}} - \bar{u}_h^{k+\frac{1}{2}}}{\Delta t}, \bar{v}_h \right\rangle + \left\langle \omega_h^{k+1} \times \frac{\bar{u}_h^{k+\frac{3}{2}} + \bar{u}_h^{k+\frac{1}{2}}}{2}, \bar{v}_h \right\rangle - \langle \bar{p}_h^{k+1}, \nabla \cdot \bar{v}_h \rangle = -\nu \langle \nabla \times \omega_h^{k+1}, \bar{v}_h \rangle, & \forall \bar{v}_h \in RT_{N,0}, \\ \langle \nabla \cdot \bar{u}_h^{k+\frac{3}{2}}, q_h \rangle = 0, & \forall q_h \in DG_{N-1}. \end{cases}$$

In this case, the approximate vorticity  $\bar{\omega}_h^{k+\frac{1}{2}}$  is evaluated at the correct time instant and therefore, unlike the previous scheme, this scheme does not require the use of any explicit time integrator.

### 2.5.3. MEEVC WITH DYNAMIC NEUMANN BOUNDARY CONDITIONS

Given  $\bar{u}_h^{k+\frac{1}{2}}$  and  $\omega_h^k$ ,

**Step 1.** Find  $\bar{p}_h^{k+\frac{1}{2}} \in CG_N$  such that:

$$\langle \nabla \bar{p}_h^{k+\frac{1}{2}}, \nabla \chi_h \rangle = -\langle \omega_h^k \times \bar{u}_h^{k+\frac{1}{2}}, \nabla \chi_h \rangle - \nu \int_{\partial\Omega} \chi_h \left( \nabla \times \omega_h^k \right) \cdot \bar{n} d\Gamma, \quad \forall \chi_h \in CG_N.$$

**Step 2.** Find  $\omega_h^{k+1} \in CG_N$  such that:

$$\begin{aligned} & \left\langle \frac{\omega_h^{k+1} - \omega_h^k}{\Delta t}, \xi_h \right\rangle - \frac{1}{2} \left\langle \frac{\omega_h^{k+1} + \omega_h^k}{2}, \nabla \cdot \left( \bar{u}_h^{k+\frac{1}{2}} \xi_h \right) \right\rangle + \frac{1}{2} \left\langle \nabla \cdot \left( \bar{u}_h^{k+\frac{1}{2}} \frac{\omega_h^{k+1} + \omega_h^k}{2} \right), \xi \right\rangle = \\ & = -\nu \langle \nabla \times \frac{\omega_h^{k+1} + \omega_h^k}{2}, \nabla \times \xi_h \rangle - \int_{\partial\Omega} \xi_h \left[ \frac{\partial g}{\partial t} \right]^{k+\frac{1}{2}} d\Gamma - \int_{\partial\Omega} \xi_h \left( \nabla \bar{p}_h^{k+\frac{1}{2}} \times \bar{n} \right) d\Gamma, \quad \forall \xi_h \in CG_N. \end{aligned}$$

**Step 3.** Find  $\left( \bar{u}_h^{k+\frac{3}{2}}, \bar{p}^{k+1} \right) \in (RT_N, DG_{N-1})$  such that:

$$\begin{cases} \left\langle \frac{\bar{u}_h^{k+\frac{3}{2}} - \bar{u}_h^{k+\frac{1}{2}}}{\Delta t}, \bar{v}_h \right\rangle + \left\langle \omega_h^{k+1} \times \frac{\bar{u}_h^{k+\frac{3}{2}} + \bar{u}_h^{k+\frac{1}{2}}}{2}, \bar{v}_h \right\rangle - \langle \bar{p}_h^{k+1}, \nabla \cdot \bar{v}_h \rangle = -\nu \langle \nabla \times \omega_h^{k+1}, \bar{v}_h \rangle, & \forall \bar{v}_h \in RT_N, \\ \langle \nabla \cdot \bar{u}_h^{k+\frac{3}{2}}, q_h \rangle = 0, & \forall q_h \in DG_{N-1}. \end{cases}$$

In this scheme, the pressure Poisson equation is discretized in time in an explicit manner because  $\omega_h^{k+\frac{1}{2}}$  is not known.

## 2.6. CONSERVATION PROPERTIES

In the original paper [11] the MEEVC scheme was formulated with periodic boundary conditions. Under these conditions, mass and total vorticity proved to be conserved for all cases; furthermore, in the inviscid limit  $\nu \rightarrow 0$ , both kinetic energy and enstrophy were also conserved. In this section, the conservation of these quantities will be studied for the three numerical schemes presented in Section 2.3.

### 2.6.1. CONSERVATION OF MASS

In (2.3), conservation of mass is expressed with the divergence-free constraint of the velocity field  $\vec{u}_h$ . As indicated in Section 2.3, the use of Raviart-Thomas elements for the velocity exactly enforces this constraint in a point-wise sense. This is valid for all of the schemes.

### 2.6.2. CONSERVATION OF VORTICITY

At the continuous level, a flow problem defined with boundary conditions (2.2) will have a constant total vorticity  $\mathcal{W}$  whenever the tangential velocity at the boundary  $g$  is independent of time. Integration over  $\Omega$  of the kinematic yields

$$\int_{\Omega} \omega \, d\Omega = - \int_{\partial\Omega} \vec{u} \times \vec{n} \, d\Gamma = - \int_{\partial\Omega} g \, d\Gamma = \text{const.}, \quad (2.35)$$

where the Stokes theorem has been used to relate the integral of the curl of the velocity to its line integral. The same result can be obtained with the vorticity transport equation. Integration over  $\Omega$  and application of the divergence theorem on the convective and diffusive terms gives

$$\frac{\partial}{\partial t} \int_{\Omega} \omega \, d\Omega = \nu \int_{\partial\Omega} \nabla \times \omega \times \vec{n} \, d\Gamma. \quad (2.36)$$

The boundary term of (2.36) can be written in terms of the pressure by restricting the momentum equation to the boundary. This integral will be zero whenever  $g$  does not depend on time, that is,

$$\frac{\partial}{\partial t} \int_{\Omega} \omega \, d\Omega = \nu \int_{\partial\Omega} (\nabla \times \omega) \times \vec{n} \, d\Gamma = - \int_{\partial\Omega} \nabla \bar{p} \times \vec{n} \, d\Gamma = 0. \quad (2.37)$$

The final equality in (2.37) holds whenever  $\Omega$  is bounded by a closed curve.

Here, conservation of vorticity will be studied for the values of  $g$  which satisfy (2.35) and for domains bounded by closed curves. The discrete conservation of total vorticity can be expressed with the following requirement:

$$\mathcal{W}_h^{k+1} = \int_{\Omega} \omega_h^{k+1} \, d\Omega := \langle \omega_h^{k+1}, 1 \rangle = \langle \omega_h^k, 1 \rangle := \int_{\Omega} \omega_h^k \, d\Omega = \mathcal{W}_h^k. \quad (2.38)$$

The time evolution of total vorticity is governed by the discretized vorticity transport equation, see (2.32). An explicit expression can be obtained for the special case of  $\xi_h = 1$ :

$$\begin{aligned} & \left\langle \frac{\omega_h^{k+1} - \omega_h^k}{\Delta t}, 1 \right\rangle - \frac{1}{2} \left\langle \frac{\omega_h^{k+1} + \omega_h^k}{2}, \nabla \cdot \vec{u}_h^{k+\frac{3}{2}} \right\rangle + \frac{1}{2} \left\langle \nabla \cdot \left( \vec{u}_h^{k+\frac{3}{2}} \frac{\omega_h^{k+1} + \omega_h^k}{2} \right), 1 \right\rangle = \\ & - \nu \left\langle \nabla \times \left( \frac{\omega_h^{k+1} + \omega_h^k}{2} \right), \nabla \times 1 \right\rangle + \nu \int_{\partial\Omega} \nabla \times \omega_h^{k+\frac{1}{2}} \times \vec{n} \, d\Gamma. \end{aligned} \quad (2.39)$$

The exact satisfaction of the divergence-free constraint implies that the second term of (2.39) is zero. On the other hand, the divergence theorem can be applied to the the third term:

$$\left\langle \nabla \cdot \left( \vec{u}_h^{k+\frac{3}{2}} \frac{\omega_h^{k+1} + \omega_h^k}{2} \right), 1 \right\rangle := \int_{\Omega} \nabla \cdot \left( \vec{u}_h^{k+\frac{3}{2}} \frac{\omega_h^{k+1} + \omega_h^k}{2} \right) \, d\Omega = \int_{\partial\Omega} \left( \frac{\omega_h^{k+1} + \omega_h^k}{2} \right) \vec{u}_h^{k+\frac{3}{2}} \cdot \vec{n} \, d\Gamma. \quad (2.40)$$

Boundary conditions (2.2) enforce  $\vec{u} \cdot \vec{n} = 0$  along  $\partial\Omega$  and these are exactly satisfied with  $\vec{u}_h \in \text{RT}_{N,0}$ . Hence, the third term of (2.40) is exactly zero. Equation (2.40) can be rearranged and written as follows:

$$\langle \omega_h^{k+1}, 1 \rangle = \langle \omega_h^k, 1 \rangle + \nu \Delta t \int_{\partial\Omega} \nabla \times \omega_h^{k+\frac{1}{2}} \times \vec{n} \, d\Gamma. \quad (2.41)$$

Whether vorticity is conserved or not will depend on which numerical scheme is chosen:

1. MEEVC with kinematic Dirichlet boundary conditions. The specification of Dirichlet boundary conditions for the vorticity transport equation requires  $\xi_h \in \text{CG}_{N,0}$ ; this implies that the Equation (2.41) will not hold for this case because it is only valid for  $\xi_h = 1 \notin \text{CG}_{N,0}$ . Numerical test cases in Section 2.7 confirm that  $\mathcal{W}_h$  is not conserved with Dirichlet boundary conditions.

2. MEEVC with kinematic Neumann boundary conditions. The boundary integral in (2.41) is computed with the *approximate* vorticity,  $\tilde{\omega}_h$ . This term is computed with the kinematic condition, Equation (2.9); for  $\tilde{\xi} = 1$ ,

$$\langle \tilde{\omega}_h^{k+\frac{1}{2}}, 1 \rangle = \langle \tilde{u}_h^{k+\frac{1}{2}}, \nabla \times 1 \rangle - \int_{\partial\Omega} g \, d\Gamma = \int_{\partial\Omega} g \, d\Gamma = \text{const.}, \quad (2.42)$$

such that the total *approximate* vorticity is conserved. However, this does not ensure the boundary integral in (2.41) to be zero because (2.37) is not strongly satisfied. In order to do so, an additional compatibility condition is developed in the Appendix A.

3. MEEVC with dynamic Neumann boundary conditions. This approach to vorticity boundary conditions has the advantage of strongly satisfying Equation (2.37). Hence, the boundary integral of  $\tilde{p}_h$  around a closed contour will always be zero and Equation (2.38) will be satisfied.

### 2.6.3. CONSERVATION OF KINETIC ENERGY

Kinetic energy  $\mathcal{K}$ , together with enstrophy  $\mathcal{E}$ , is one of the two *secondary* conservation properties of the MEEVC scheme. In the original paper, the conservation of  $\mathcal{K}$  was proved for the inviscid limit  $\nu = 0$ . As will be proved below, the approach taken for the prescription of boundary conditions does not affect conservation of kinetic energy.

At the continuous level,  $\mathcal{K}$  is proportional to the  $L^2(\Omega)$  norm of the velocity,

$$\mathcal{K} = \frac{1}{2} \|\tilde{u}\|_{L^2(\Omega)}^2 = \frac{1}{2} \langle \tilde{u}, \tilde{u} \rangle. \quad (2.43)$$

This definition extends to the discrete level:

$$\mathcal{K}_h = \frac{1}{2} \|\tilde{u}_h\|_{L^2(\Omega)}^2 = \frac{1}{2} \langle \tilde{u}_h, \tilde{u}_h \rangle. \quad (2.44)$$

Conservation of kinetic energy at the discrete level requires the following equality to hold:

$$\mathcal{K}_h^{k+\frac{1}{2}} = \frac{1}{2} \langle \tilde{u}_h^{k+\frac{1}{2}}, \tilde{u}_h^{k+\frac{1}{2}} \rangle = \frac{1}{2} \langle \tilde{u}_h^{k+\frac{3}{2}}, \tilde{u}_h^{k+\frac{3}{2}} \rangle = \mathcal{K}_h^{k+\frac{3}{2}}. \quad (2.45)$$

This equality can be proved to hold by evaluating the momentum equation in its discretised form, see (2.32), with  $\tilde{v}_h = \frac{1}{2} \tilde{u}_h^{k+\frac{3}{2}} + \frac{1}{2} \tilde{u}_h^{k+\frac{1}{2}}$ :

$$\frac{1}{2} \left\langle \frac{\tilde{u}_h^{k+\frac{3}{2}} - \tilde{u}_h^{k+\frac{1}{2}}}{\Delta t}, \tilde{u}_h^{k+\frac{3}{2}} + \tilde{u}_h^{k+\frac{1}{2}} \right\rangle + \frac{1}{2} \langle \omega_h^{k+1} \times \frac{\tilde{u}_h^{k+\frac{3}{2}} + \tilde{u}_h^{k+\frac{1}{2}}}{2}, \tilde{u}_h^{k+\frac{3}{2}} + \tilde{u}_h^{k+\frac{1}{2}} \rangle - \frac{1}{2} \langle \tilde{p}_h^{k+1}, \nabla \cdot (\tilde{u}_h^{k+\frac{3}{2}} + \tilde{u}_h^{k+\frac{1}{2}}) \rangle = 0. \quad (2.46)$$

The third term of (2.46) is identically zero because both  $\tilde{u}_h^{k+\frac{3}{2}}$  and  $\tilde{u}_h^{k+\frac{1}{2}}$  are divergence free. The second term can be written as follows,

$$\langle \omega_h^{k+1} \times \frac{\tilde{u}_h^{k+\frac{3}{2}} + \tilde{u}_h^{k+\frac{1}{2}}}{2}, \tilde{u}_h^{k+\frac{3}{2}} + \tilde{u}_h^{k+\frac{1}{2}} \rangle = \langle \omega_h^{k+1} \times \tilde{u}_h^{k+\frac{3}{2}}, \tilde{u}_h^{k+\frac{1}{2}} \rangle + \langle \omega_h^{k+1} \times \tilde{u}_h^{k+\frac{1}{2}}, \tilde{u}_h^{k+\frac{3}{2}} \rangle \quad (2.47)$$

Following [38, Lemma 1.3], given the trilinear form  $\mathcal{B}(\vec{a}, \vec{b}, \vec{c}) = \langle \vec{a}, \vec{b} \times \vec{c} \rangle$ , the identity  $\mathcal{B}(\vec{a}, \vec{b}, \vec{c}) = -\mathcal{B}(\vec{c}, \vec{b}, \vec{a})$  can be proved to hold, such that (2.47) is identically zero. This proves that (2.45) holds for  $\nu = 0$ .

### 2.6.4. CONSERVATION OF ENSTROPY

The MEEVC scheme was proved to conserve enstrophy  $\mathcal{E}$  for the case of periodic boundary conditions and  $\nu = 0$  [11]. In this section we demonstrate that, depending on the approach chosen for the prescription of vorticity boundary conditions, enstrophy may or may not be conserved, even though tangential velocity boundary conditions no longer make sense when considering an inviscid flow.

In the same way as  $\mathcal{K}$ , enstrophy is defined proportional to the  $L^2(\Omega)$  norm of the vorticity,

$$\mathcal{E} = \frac{1}{2} \|\omega\|_{L^2(\Omega)}^2 = \frac{1}{2} \langle \omega, \omega \rangle, \quad (2.48)$$

with its discrete counterpart defined as,

$$\mathcal{E}_h = \frac{1}{2} \|\omega_h\|_{L^2(\Omega)}^2 = \frac{1}{2} \langle \omega_h, \omega_h \rangle. \quad (2.49)$$

In the same way as (2.45), conservation of enstrophy at the discrete level requires

$$\mathcal{E}_h^k = \frac{1}{2} \langle \omega_h^k, \omega_h^k \rangle = \frac{1}{2} \langle \omega_h^{k+1}, \omega_h^{k+1} \rangle = \mathcal{E}_h^{k+1} \quad (2.50)$$

to hold when  $\nu = 0$ . The identity (2.50) can be proved to hold whenever the dissipation and the boundary term in the vorticity equation in (2.32) are neglected. By substituting  $\xi_h = \frac{1}{2}\omega_h^k + \frac{1}{2}\omega_h^{k+1}$  into the discretized vorticity transport equation (see (2.32)), the following expression is obtained,

$$\begin{aligned} & \frac{1}{2} \left\langle \frac{\omega_h^{k+1} - \omega_h^k}{\Delta t}, \omega_h^{k+1} + \omega_h^k \right\rangle - \frac{1}{4} \left\langle \frac{\omega_h^{k+1} + \omega_h^k}{2}, \nabla \cdot \left( \bar{u}_h^{k+\frac{1}{2}} (\omega_h^{k+1} + \omega_h^k) \right) \right\rangle \\ & + \frac{1}{4} \left\langle \nabla \cdot \left( \bar{u}_h^{k+\frac{1}{2}} \frac{\omega_h^{k+1} + \omega_h^k}{2} \right), \omega_h^{k+1} + \omega_h^k \right\rangle = 0. \end{aligned} \quad (2.51)$$

The two last terms of Equation (2.51) are equal with opposing signs; hence, Equation (2.50) is proved to hold and the discrete enstrophy is conserved for  $\nu = 0$ . However, this derivation will not be valid for each of the numerical schemes described in Section 2.5:

1. MEEVC with kinematic Dirichlet boundary conditions. In this case,  $\xi_h = \frac{1}{2}\omega_h^k + \frac{1}{2}\omega_h^{k+1} \notin \text{CG}_{N,0}$  and the previous derivation is not valid. Numerical test cases in Section 2.7.2 indicate that enstrophy is not conserved when  $\nu = 0$ .
2. MEEVC with kinematic Neumann boundary conditions. This scheme respects the inviscid limit in such a way that, when  $\nu \rightarrow 0$ , both the dissipation term and its associated boundary term tend to zero. Therefore, (2.51) is valid for the kinematic Neumann boundary conditions.
3. MEEVC with dynamic Neumann boundary conditions. The use of dynamic boundary conditions for the vorticity equation implies that the corresponding boundary term no longer depends explicitly on  $\nu$ . For the limit  $\nu = 0$ ,

$$\frac{1}{2} \langle \omega_h^{k+1}, \omega_h^{k+1} \rangle = \frac{1}{2} \langle \omega_h^k, \omega_h^k \rangle - \frac{\Delta t}{2} \int_{\partial\Omega} (\omega_h^k + \omega_h^{k+1}) \left( \left[ \frac{\partial g}{\partial t} \right]^{k+\frac{1}{2}} + \nabla \bar{p}_h^{k+\frac{1}{2}} \times \bar{n} \right) d\Gamma. \quad (2.52)$$

Equation (2.52) indicates that not only is enstrophy not exactly conserved, but also that  $g$  still enters the equation even though  $\nu = 0$ .

## 2.7. NUMERICAL TEST CASES

In this section, two numerical test cases are computed with the three schemes that have been introduced in Section 2.5. The first test is the Taylor-Green vortex, for which an analytical solution is known and convergence rates for the discrete velocity and vorticity can be obtained. The second test is the dipole collision and results are shown for  $\text{Re} = 625$  and for the inviscid limit,  $\nu = 0$  and  $\text{Re} \rightarrow \infty$ . Detailed results are shown for the dipole collision which shed light on the advantages and disadvantages of the three schemes.

Further numerical results can be found in Appendices A and B. Compatibility conditions which enable total vorticity conservation for kinematic Neumann boundary conditions are presented and tested in Appendix A. In Appendix B, an alternative formulation to that of (2.3) is presented and its discretization is compared to the MEEVC scheme with kinematic Neumann boundary conditions. For the two appendices, numerical results are computed for the dipole collision at  $\text{Re} = 625$ .

### 2.7.1. TAYLOR-GREEN VORTEX. ORDER OF ACCURACY OF THE SCHEMES.

The Taylor-Green vortex is a suitable analytical solution for testing the order of accuracy of a scheme. The solution is given by:

$$\begin{cases} u_x(x, y, t) = -\sin(\pi x) \cos(\pi y) e^{-2\pi^2 \nu t}, \\ u_y(x, y, t) = \cos(\pi x) \sin(\pi y) e^{-2\pi^2 \nu t}, \\ p(x, y, t) = \frac{1}{4} (\cos(2\pi x) + \cos(2\pi y)) e^{4\pi^2 \nu t}, \\ \omega(x, y, t) = -2\pi \sin(\pi x) \sin(\pi y) e^{-2\pi^2 \nu t}. \end{cases} \quad (2.53)$$

Table 2.1: Orders of convergence for velocity and vorticity  $L^2$ -errors. Results obtained with periodic boundary conditions are also included as a reference.

	$\ \vec{u} - \vec{u}_h\ _{L^2}$			$\ \omega - \omega_h\ _{L^2}$		
	$N = 1$	$N = 2$	$N = 4$	$N = 1$	$N = 2$	$N = 4$
Kinematic Dirichlet	1.02	1.98	3.99	1.18	1.57	3.44
Kinematic Neuman	1.00	1.98	3.94	0.99	2.92	3.98
Dynamic Neuman	0.96	0.97	0.16	0.10	0.02	0.21
Periodic b.c.	1.05	1.97	3.92	1.87	3.19	5.02

This test case was also used in the previous paper [11] with periodic boundary conditions. For this study, the solution is defined on a domain  $\Omega = [0, 2] \times [0, 2]$  and the boundary conditions are assumed to correspond with  $\vec{u} = (u_x, u_y)$  on  $\partial\Omega$ ; therefore,  $\vec{u} \cdot \vec{n} = 0$  and  $g = g(x, y, t) = (u_x, u_y) \times \vec{n}$ . The kinematic viscosity is set to  $\nu = 0.01$  and the solution is evolved from  $t = 0$  to  $t = 1$ .

The variation of  $L^2$  errors for  $\vec{u}$  and  $\omega$  are considered for the three schemes suggested in Section 2.5. Calculations are carried out for the polynomial degrees  $N = 1, 2$  and  $4$ , for which the time steps  $\Delta t = 10^{-2}, 5 \times 10^{-3}$  and  $1 \times 10^{-4}$  are used, respectively, such that the error introduced by the time integration is very small. The errors are calculated at  $t = 1$  and are plotted in Figure 2.3. The orders of convergence, which can be found in Table 2.1, have been calculated for each solver and each polynomial order. Table 2.1 also includes the orders of convergence obtained with the MEEVC scheme with periodic boundary conditions.

The expected orders of convergence are shown in Figure 2.3 with black lines. They correspond with the orders of convergence obtained with the MEEVC scheme with periodic boundary conditions. For  $\vec{u}_h$ , order  $N$  was obtained, while convergence rates of  $N + 1$  were obtained for  $\omega_h$ <sup>2</sup>.

The results indicate that the solution with the dynamic Neumann boundary conditions does not converge to the exact solution. Both of the kinematic boundary conditions yield convergence rates for the velocity equivalent to those obtained with periodic boundary conditions.

Regarding the vorticity, the reference convergence rate is only obtained for the kinematic Neumann boundary conditions when  $N = 2$ ; for  $N = 1$  and  $4$ , this method yields rates of order  $N$ . These convergence rates are the highest of the three methods proposed in this chapter. However, for the case of the vorticity, these are non-optimal with respect to the MEEVC solver with periodic boundary conditions.

For the kinematic Dirichlet boundary conditions, the convergence rates are of order  $N - 0.5$  for  $N = 2$  and  $4$ . This could be related to previous results from Lee et al. and Benzi et al., which report that kinematic Dirichlet boundary conditions introduce numerical errors into the boundary vorticity, propagating further into the domain throughout the computation, resulting in order reduction [29, 30].

### 2.7.2. DIPOLE COLLISION

In this section, a series of results are shown for the normal dipole collision, a test case consisting in a self-propelled vorticity dipole which collides against a wall. This test case was originally proposed for the quantification of vorticity produced in the boundary layers [39]. Thus, this flow problem is an ideal test case for evaluating the different methods for prescribing vorticity boundary conditions suggested in this work.

The results computed in this section are for  $Re = 625$ , in a domain  $\Omega = [1, 1] \times [-1, 1]$  and for times  $t = 0$  to  $t = 1$ , see Figure 2.4. No-slip boundary conditions,  $\vec{u} = 0$ , are prescribed along the boundary. The initial vorticity distribution for each monopole is given by

$$\omega_0 = \omega_e \left( 1 - \left( \frac{r}{r_0} \right)^2 \right) \exp \left( - \left( \frac{r}{r_0} \right)^2 \right), \quad (2.54)$$

where  $r$  is the distance from the center of the monopole,  $r_0$  its dimensionless radius and  $\omega_e$  its dimensionless extremum vorticity. Following Clercx and Bruneau [39], the value  $r_0 = 0.1$  is taken for both monopoles and  $\{\omega_{e,1}, \omega_{e,2}\} = \{320, -320\}$ . The initial position of both monopoles is  $\{(x_1, y_1), (x_2, y_2)\} = \{(0, 0.1), (0, -0.1)\}$ .

Comparisons are made with the benchmark results given by Clercx and Bruneau [39]. The benchmark results are computed with a finite difference scheme in  $(\vec{u}, p)$  formulation with  $N_{FD}$  equidistant cells along each direction and with a pseudospectral Chebyshev method in  $(\vec{u}, \omega, p)$  formulation with  $N_{SM}$  collocation points in each direction.

<sup>2</sup>Convergence rates for  $\omega_h$  were not shown in [11].

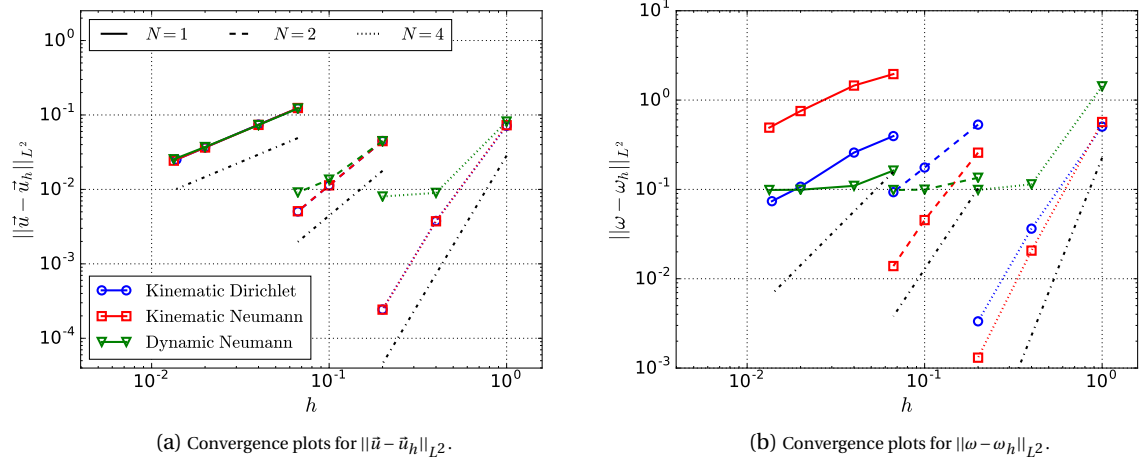


Figure 2.3:  $h$ -convergence of velocity and vorticity errors measured in the  $L^2$ -norm for different polynomial degrees  $N$ . Calculations have been carried out for the three schemes suggested in Section 2.5. The black lines indicate convergence rates obtained with the MEEVC scheme with periodic boundary conditions.

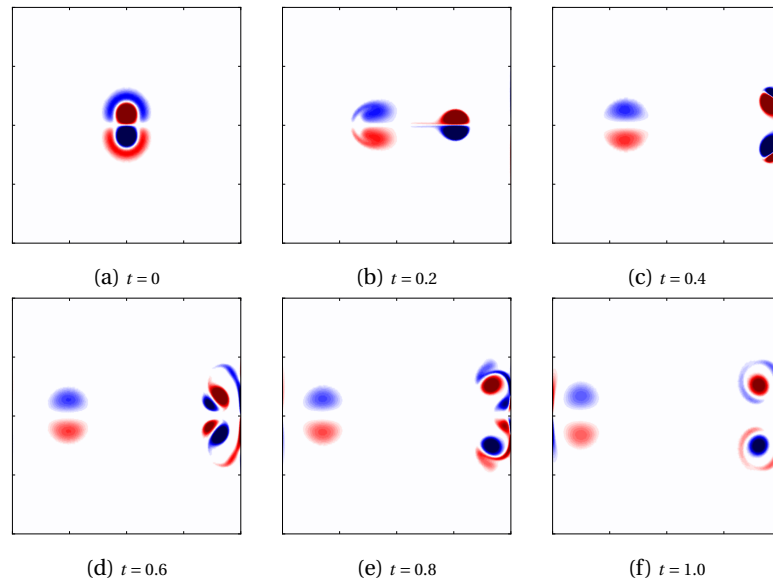


Figure 2.4: The normal dipole collision for  $\text{Re} = 625$  in a domain  $\Omega = [1, 1] \times [-1, 1]$ , from  $t = 0$  to  $t = 1$ , obtained with the MEEVC scheme with kinematic Neumann boundary conditions for  $N = 2$  and 5210 cells.

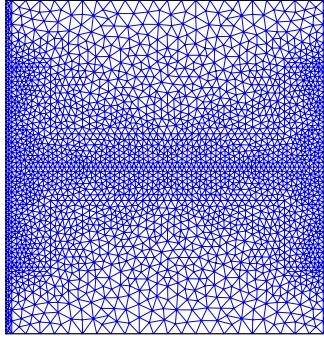


Figure 2.5: Unstructured mesh used for the computation of the dipole collision for  $Re = 625$ .

### COMPARISON OF THE NUMERICAL SCHEMES

The performance of each of the solvers proposed in Section 2.5 is evaluated by computing the normal dipole collision test case. The results presented have been computed with 5210 cells of polynomial degree  $N = 2$ , see Figure 2.5, such that 10645, 26274 and 2718 degrees of freedom are assigned to the vorticity, velocity and pressure, respectively. Regarding the time discretization, a time step of  $\Delta t = 5 \times 10^{-4}$  is used.

In Figure 2.6, the vorticity contour of the region  $0.4 \leq x \leq 1$  and  $0 \leq y \leq 0.6$  is plotted (the upper-right part of the domain, see Figure 2.4f for the vorticity distribution in  $\Omega$  at  $t = 1$ ); these contours are compared to the contour computed by Clercx and Bruneau with a high order spectral method ( $N_{SM} = 256$ ). From of Figure 2.6 we see that the dynamic Neumann boundary conditions introduces visible errors in the region close to the boundary.

Figure 2.7 shows the variation of the discrete kinetic energy  $\mathcal{K}_h$ , enstrophy  $\varepsilon_h$  and palinstrophy  $\mathcal{P}_h$ . These integral variables are compared with the results from Clercx and Bruneau at  $t = 0.25, 0.5$  and  $0.75$  and for the first two maxima of  $\varepsilon_h$  and  $\mathcal{P}_h$ . The exact numerical values of these quantities at this times are given in Tables C.1, C.2 and C.3.

The palinstrophy is given by

$$\mathcal{P}_h = \frac{1}{2} \langle \nabla \omega_h, \nabla \omega_h \rangle, \quad (2.55)$$

such that  $\mathcal{P}_h$  depends on the vorticity gradient in  $\Omega$  and is therefore much more sensitive to approximation errors than the enstrophy. Figure 2.7c clearly shows that the palinstrophy obtained with dynamic Neumann boundary conditions differs from the results given by the reference and the two remaining methods after the first maximum. The first maximum coincides approximately with the moment of the first collision, when large variations in the wall vorticity occur.

The variation with time of the total vorticity  $\mathcal{W}_h$  and the  $L^2$  norm of the divergence field,  $\|\nabla \cdot \vec{u}_h\|_{L^2}$ , are plotted in Figure 2.8. The divergence field is solved up to the tolerance set for the iterative solver of the linear system and is very close to machine precision. Regarding the vorticity, taking into account that  $\vec{u} = 0$  on  $\partial\Omega$ , the discrete total vorticity  $\mathcal{W}_h$  should be conserved for all  $t$ . As expected, the MEEVC scheme with dynamic Neumann boundary conditions satisfies this requirement and the kinematic Neumann method does not. This result confirms that kinematic Dirichlet boundary conditions do not conserve  $\mathcal{W}_h$ .

More valuable insight into the performance of the different schemes can be obtained when observing the vorticity at the wall. In Figure 2.9, the vorticity values at  $x = 1$  and  $-0.6 \leq y \leq 0$  (lower region of the right wall) are plotted for three different time instants and compared with the results from the reference. The results obtained for the kinematic Neumann boundary conditions show smooth curves which differ from the reference curve in a considerable amount for  $t = 0.4$  (more or less the instant of the first collision). This result contrasts with those obtained with the kinematic Dirichlet and dynamic Neumann boundary conditions; in these cases, the vorticity can be seen to oscillate around the reference curve, indicating a possible existence of spurious vorticity modes at the boundary. The oscillations are much greater for the case of the dynamic boundary conditions and seem to explain the existence of ripples which can be appreciated towards the wall in Figure 2.6c.

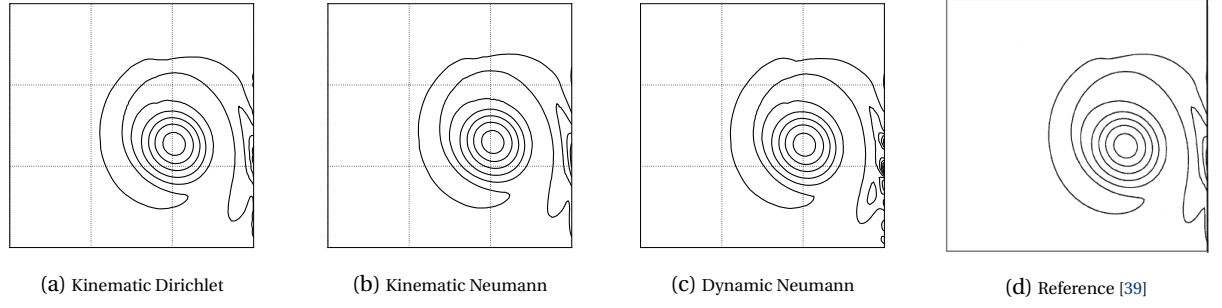


Figure 2.6: Vorticity contour plots for the dipole collision at  $t = 1$ , for the region  $0.4 \leq x \leq 1$  and  $0 \leq y \leq 0.6$ . The contours have been plotted for the vorticity levels  $(150, 130, \dots, 30, 10, -10, -30, \dots, -130, -150)$ .

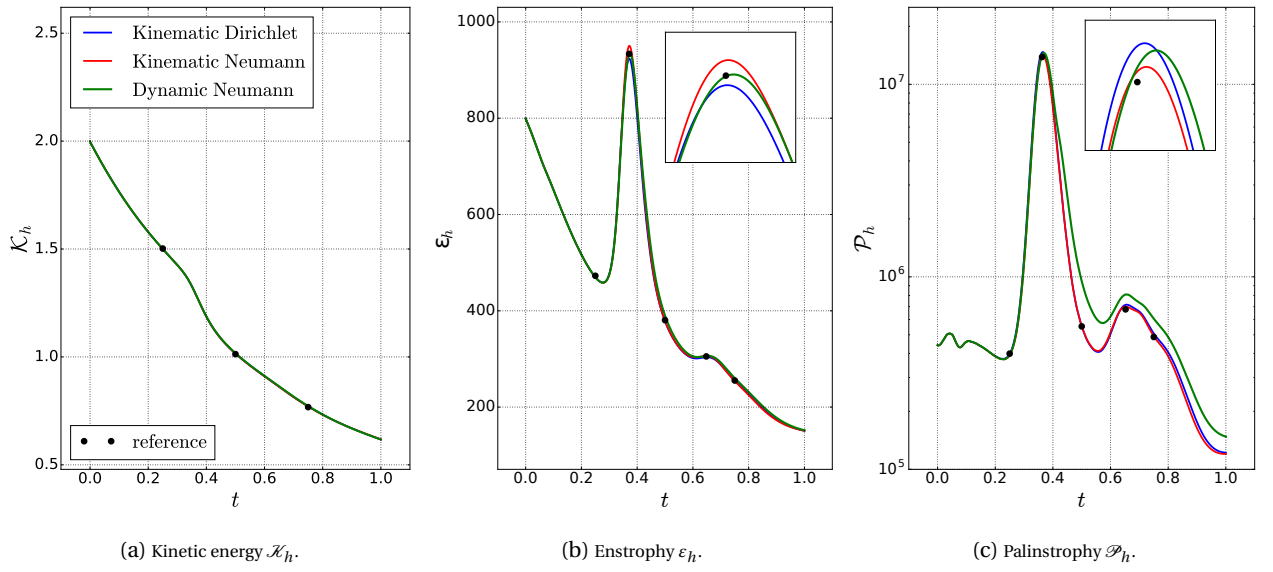


Figure 2.7: Variation over time of the kinetic energy, enstrophy and palinstrophy. Comparisons are made with the results given in [39] at  $t = 0.25, 0.5$  and  $0.75$ .

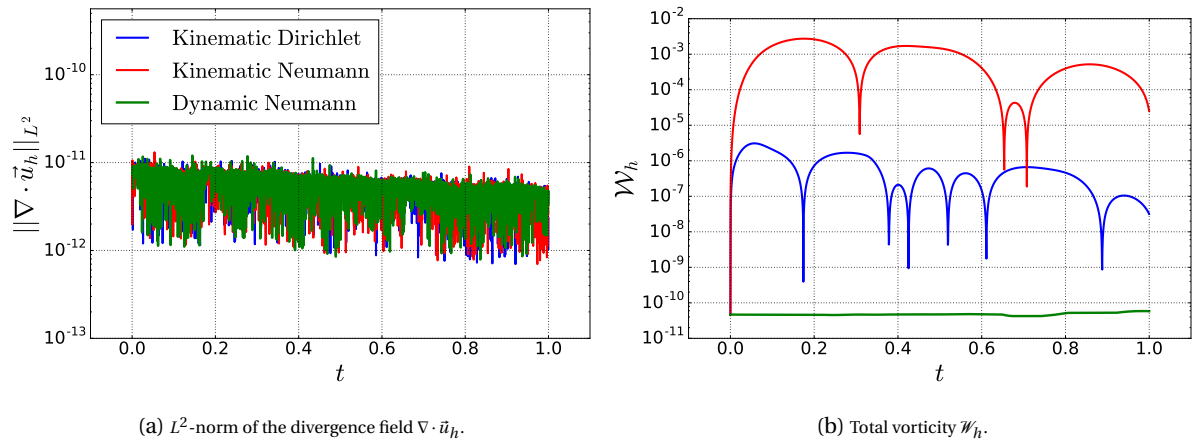


Figure 2.8: Variation over time of the  $L^2$ -norm of the divergence field,  $\|\nabla \cdot \vec{u}_h\|_{L^2}$ , and the total vorticity  $\mathcal{W}_h$ .

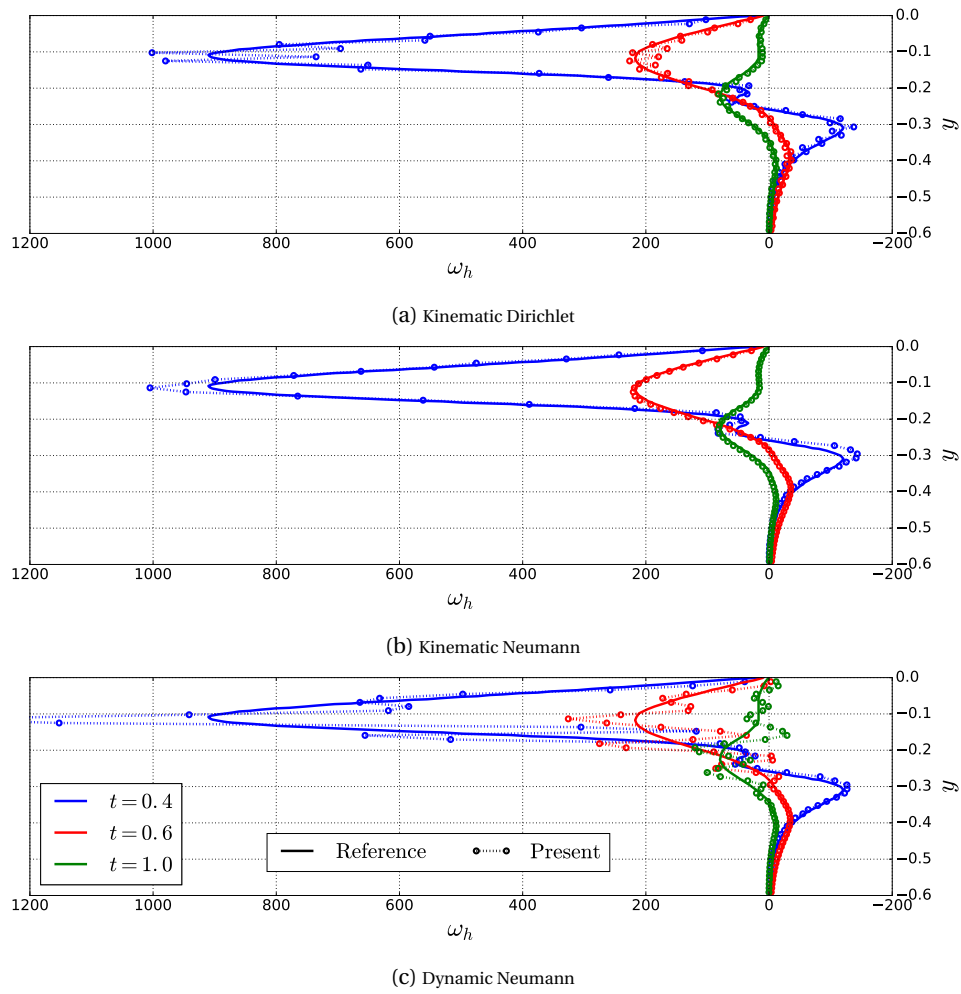


Figure 2.9: Vorticity distribution at  $x=1$  and  $-0.6 \leq y \leq 0$  (lower region of the right wall). The wall vorticity has been plotted for each solver at  $t=0.4, 0.6$  and  $1$  and is compared to the results given in [39].

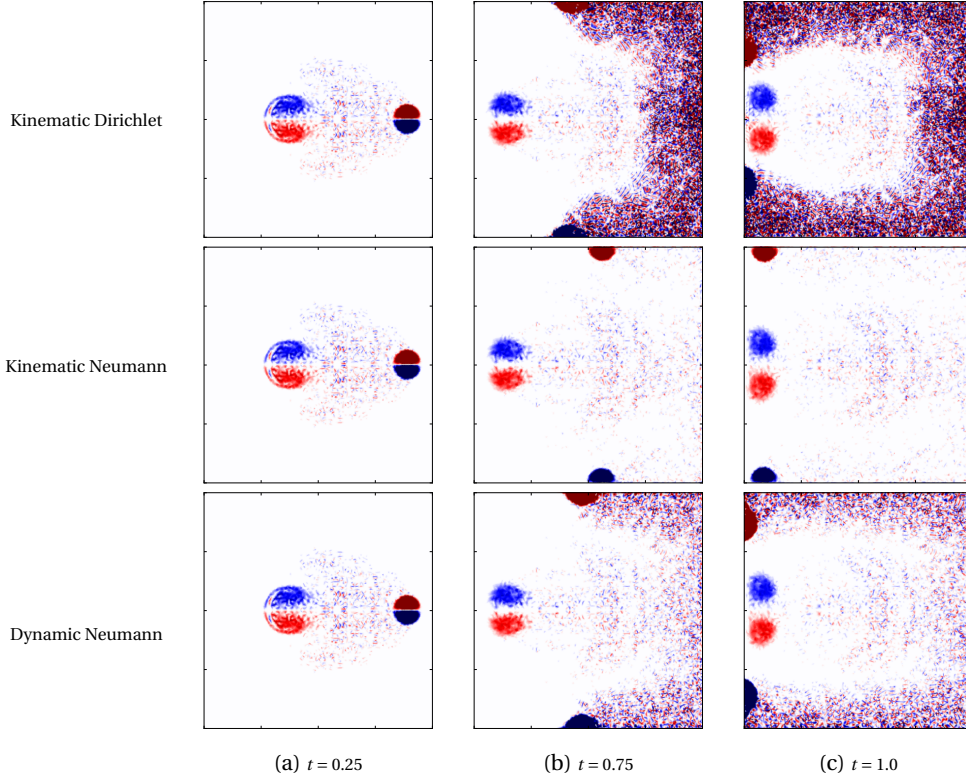


Figure 2.10: Vorticity distribution at  $t = 0.25, 0.75$  and  $1$  for the inviscid dipole collision computed with the three solvers.

#### THE INVISCID DIPOLE COLLISION

For the inviscid limit  $\nu = 0$ , the dipole collision is a useful test case for the performance of the solvers in the inviscid limit. It gives a computational demonstration of the conservation properties of  $\mathcal{K}_h$  and  $\varepsilon_h$ , analyzed in Sections 2.6.3 and 2.6.4. Furthermore, the inviscid limit is interesting because slip boundary conditions can no longer be imposed. In Section 2.6, it was noted that both the MEEVC scheme with kinematic Dirichlet and with dynamic Neumann boundary conditions require the computation of  $g(x, t) = \bar{u} \times \bar{n}$  on  $\partial\Omega$ . In this case  $g$  is no longer a known function and it must be computed from  $\bar{u}$ . This operation is not well defined, because  $\bar{u} \in H(\text{div}, \Omega)$ .

In the same way that  $\nabla \times \omega \times \bar{n}$  is not well posed but can still be computed from a computational point of view, the same will be done for  $\bar{u} \times \bar{n}$  on  $\partial\Omega$ . The inviscid dipole collision has been computed for 6740 cells of order  $N = 2$ . Figure 2.10 contains plots of the vorticity distribution at  $t = 0.25, 0.75$  and  $1.0$ ; it is noted that when the dipole collides into the wall, the two monopoles travel along the wall in opposing directions. The kinematic Dirichlet and dynamic Neumann boundary conditions introduce a large amount of errors along the boundary.

In the inviscid dipole collision, the kinetic energy  $\mathcal{K}_h$ , total vorticity  $\mathcal{W}_h$  and enstrophy  $\varepsilon_h$  are conserved. The variation of their discrete counterparts, computed with the three solvers, are presented in Figure 2.11. The three methods, conserve kinetic energy, an expected result because the momentum equation is not modified. Total vorticity and enstrophy are not conserved with kinematic Dirichlet or dynamic Neumann boundary conditions. In the latter case, the following relation holds at the continuous level,

$$\nu \int_{\partial\Omega} \xi (\nabla \times \omega) \times \bar{n} \, d\Gamma = - \int_{\partial\Omega} \xi \frac{\partial}{\partial t} (\bar{u} \times \bar{n}) \, d\Gamma - \int_{\partial\Omega} \xi \nabla \bar{p} \times \bar{n} \, d\Gamma = 0. \quad (2.56)$$

Equation (2.56) indicates that dynamic Neumann boundary conditions introduce a term in the vorticity transport equation which is zero in the inviscid limit. At the discrete level, this term is not exactly zero due to the acceleration term; therefore, spurious vorticity and enstrophy are introduced into the domain. In a similar way, kinematic Dirichlet boundary conditions enforce  $\bar{\omega} = \nabla \times \bar{u}$  on  $\partial\Omega$ , such that  $\bar{\omega}_h \neq \omega_h$  at the discrete level. On the other hand, with kinematic Neumann boundary conditions,  $\omega_h$  is fully modeled with the vorticity transport equation and no vorticity boundary conditions are introduced when  $\nu = 0$ .

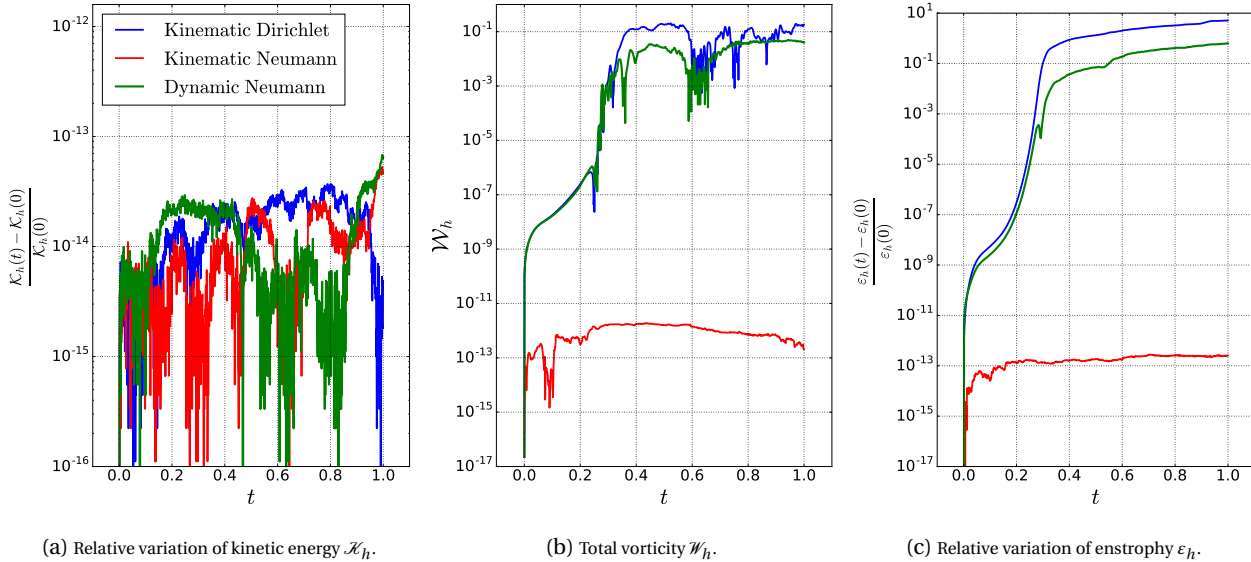


Figure 2.11: Variation over time of the kinetic energy, vorticity and enstrophy.

## 2.8. CONCLUDING REMARKS

In this chapter, three possibilities have been proposed for the prescription of slip boundary conditions for the MEEVC scheme. The three methods are compared in order to determine which one yields the best results. In this final section, the numerical results are discussed and a method is selected for the construction of a solver for turbidity currents.

The MEEVC scheme with dynamic Neumann boundary conditions is of interest because it is capable of exactly representing the necessary conditions for exact vorticity conservation in 2D for  $\nu > 0$ . However, it can be concluded from the numerical results obtained in Section 2.7 that this method does not converge to the correct solution.

The MEEVC scheme with both kinematic Dirichlet and Neumann boundary conditions yields convergence rates for the velocity equal to those obtained with the original scheme. Furthermore, almost no differences can be found between the two resulting velocity fields. However, a slight deterioration in the convergence rate of the vorticity is found for the kinematic Dirichlet boundary conditions. The results obtained from the dipole collision indicate that, unlike the case with kinematic Neumann boundary conditions, oscillations appear near the wall in the vorticity when using the Dirichlet boundary conditions.

These results imply that, of the three approaches that have been suggested, kinematic Neumann boundary conditions are the most appropriate. Furthermore, the inviscid computations of Section 2.7.2 indicate that only kinematic Neumann boundary conditions respect the behavior of the solution for  $\nu \rightarrow 0$ . A clear disadvantage of this approach is the fact that vorticity cannot be conserved. To this end, a compatibility condition for the vorticity boundary conditions has been investigated and a preliminary method, only valid for the case of a domain bounded by a closed curve, has been proposed in Appendix A. Results obtained for the dipole collision with and without the compatibility condition suggest that this additional condition is capable of enforcing conservation of vorticity without deteriorating the solution.

Finally, the MEEVC scheme with kinematic Neumann boundary conditions is compared with an alternative scheme based on a  $(\vec{u}, \omega, p)$  formulation in which the vorticity evolution equation is replaced by the kinematic condition, (2.9). For this scheme, which is discretized in the same way as the MEEVC scheme, the prescription of velocity boundary conditions is more straightforward and therefore is a reasonable option to consider. The results indicate that this scheme is more stable than the MEEVC on coarse grids, although for more refined meshes the MEEVC scheme yields better results. Furthermore, this alternative scheme cannot be decoupled and much higher computation times are required.

Therefore, linking back to the objective of this thesis, the MEEVC scheme with kinematic Neumann boundary conditions is selected for the construction of a solver for turbidity currents. This solver is developed in the next chapter.



# 3

## DEVELOPMENT OF A SOLVER FOR TURBIDITY CURRENTS

### 3.1. INTRODUCTION

In this chapter, the MEEVC scheme with kinematic Neumann boundary conditions is extended in order to model turbidity currents. These are gravity-driven, particle-laden currents and therefore the presence of a dilute particle phase must be modeled. A simple approach is implemented, the equilibrium Eulerian method [40], and the lock exchange flow is computed. Comparisons are made with existing results in order to evaluate the modified MEEVC scheme.

#### 3.1.1. HIGH-RESOLUTION COMPUTATIONS OF TURBIDITY CURRENTS

Early direct numerical simulations of gravity currents focused on the formation of intrusion fronts in lock exchange flows [41, 42]. The models used in these computations consist of the Boussinesq equation, in which a transport equation models the advection and diffusion of the density variable. Extensions to particle-laden flows were first carried out by Necker et al. [43, 44] with the equilibrium Eulerian approach. In these initial computations, the particle velocity field was assumed to be the sum of the carrier fluid's velocity plus a constant settling velocity. Further studies have investigated gravity currents in more complex geometries [45, 46] and have considered non-Boussinesq flows [47]. Cantero et al. have extended the investigations on particle-laden flows and accounted for inertial effects, in addition to a settling velocity [48]. More recently, Parkinson et al. [49] have computed particle-laden flows with discontinuous Galerkin finite elements. Espath et al. [50] explore the validity of 2D computations of turbidity currents by comparing them with 3D computations and with experimental data.

#### 3.1.2. OVERVIEW OF THIS CHAPTER

In Section 3.2, a series of modeling possibilities for dilute particle-laden flows are presented and the equilibrium Eulerian approach is described. Section 3.3 presents the lock exchange problem and specifies the boundary conditions required for modeling the settling of particles in turbidity currents. Next, in Section 3.4, the finite element discretization of the equilibrium Eulerian approach is presented. The energy budget of a turbidity current is examined in Section 3.5 in order to understand the conservation properties of the solver. Finally, in Section 3.6, numerical results are presented for the lock exchange case and comparisons are made with the literature.

### 3.2. MODELING CONSIDERATIONS

In this section, a series of modeling possibilities are presented for dilute suspensions. Of these, the equilibrium Eulerian model is chosen for the construction of the turbidity current solver and the equations of motion are derived.

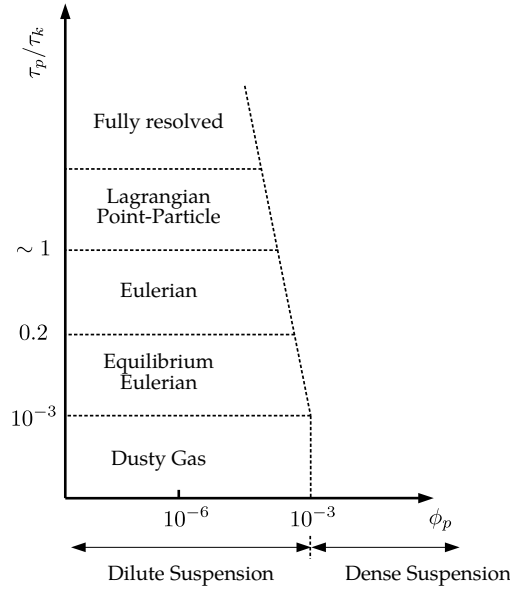


Figure 3.1: Different approaches to modeling particle-laden flows according to the volume fraction  $\phi_p$  of the particle phase and time scale ratio (Stokes number). The inclined line reflects the increasing importance of particle collisions for larger particle sizes. Figure taken from Balachandar [52].

### 3.2.1. MODELING POSSIBILITIES FOR DILUTE SUSPENSIONS

A large set of modeling possibilities exist for particle-laden flows. The range of validity of these models is generally determined by two parameters: the Stokes number and the volumetric concentration of particles in the flow [51, 52]. The Stokes number is defined as the ratio  $\tau_p/\tau_f$ , where  $\tau_p$  and  $\tau_f$  are the characteristic time-scale of the particles and the smallest time-scale of the flow (i.e. the Kolmogorov time-scale), respectively. Assuming Stokes flow around the particles,  $\tau_p$  can be calculated with,

$$\tau_p = \frac{\rho_p d^2}{18\rho_f \nu}, \quad (3.1)$$

where  $\rho_p$  and  $\rho_f$  are the particle and fluid densities, respectively,  $d$  is the particle diameter and  $\nu$  the dynamic viscosity of the fluid [51].

Figure 3.1 summarizes the modeling possibilities for dilute particle suspensions. In this case, the volumetric concentration of particles is limited to  $\phi_p < 10^{-3}$ , such that a two-way coupling based on momentum exchange exists between the fluid and the particles. For higher concentrations, the flow is considered a dense suspension and particle-particle interaction becomes important (four-way coupling), [51].

The different modeling approaches indicated in Figure 3.1 are briefly explained below.

- **Dusty gas approach.** Particles are assumed to be sufficiently small such that they follow the carrier fluid. The equations to be solved are the Navier-Stokes equations with a modified density together with a transport equation for particles.
- **Equilibrium Eulerian approach.** Developed by Ferry and Balachandar and also known as the *fast Eulerian method* [40], this method retains the simplicity of the dusty gas approach by assuming that the particle velocity field can be expanded in terms of the carrier fluid velocity field and calculated by means of an algebraic equation. This method gives adequate results for particles with Stokes numbers just below unity and density ratio parameters  $\rho_p/\rho_f$  of order  $\mathcal{O}(1)$  or lower. Further attention is given to this method in Section 3.2.2.
- **Eulerian approach.** Both the fluid and the particles are treated as two different continuum fluid phases. In this case, momentum and energy equations must also be solved for the particle phase. The principal restriction for this method is that within a small volume of fluid the particles must have a unique velocity, momentum and energy.

- **Lagrangian approach.** For  $\tau_p/\tau_f > 1$ , the relative particle sizes are such that the continuum phase assumption is no longer realistic, that is, assuming uniqueness of particle properties over small areas of the fluid is not valid. In the Lagrangian approach, particles are represented in a Lagrangian reference frame and their properties are calculated with probabilistic methods. In this case, there is no requirement for uniqueness and the flow equations are valid until the Stokes number is such that the point-particle assumption no longer makes sense.

In this work, the equilibrium Eulerian approach will be used due to its simplicity and its capacity to capture both inertial and gravitational effects characteristic of turbidity currents. In the following subsection, the equilibrium assumption will be applied to the Eulerian-Eulerian equations and a set of equations for dilute suspensions will be derived.

### 3.2.2. EQUILIBRIUM EULERIAN EQUATIONS FOR A DILUTE SUSPENSION

A set of equations for a fluid-particle system studied from an Eulerian point of view can be obtained by mixture theory or by ensemble averaging [53]. The volumetric concentrations of the fluid and particle phases are denoted  $\phi_f$  and  $\phi_p$  respectively, the densities  $\rho_f$  and  $\rho_p$  and the velocities  $\vec{u}_p$  and  $\vec{u}_f$ .

By assuming constant densities for both phases and no mass transfer, the equations of motion in dimensional form can be written as follows [48],

$$\begin{cases} \frac{\partial \phi_f}{\partial t} + \nabla \cdot (\phi_f \vec{u}_f) = 0, \\ \frac{\partial \phi_p}{\partial t} + \nabla \cdot (\phi_p \vec{u}_p) = 0, \\ \phi_p \rho_p \frac{D_p \vec{u}_p}{Dt} = \phi_p (\rho_p - \rho_f) \vec{g} - \phi_p \nabla p + \vec{F}, \\ \phi_f \rho_f \frac{D_f \vec{u}_f}{Dt} = -\phi_f \nabla p + \mu \Delta \vec{u}_v - \vec{F}, \end{cases} \quad (3.2)$$

where  $\vec{F}$  represents the net hydrodynamic interaction between both phases,  $\vec{g} = g\vec{e}_g$  is the gravitational acceleration vector ( $\vec{e}_g$  is the unit vector pointing in the direction of the gravitational force) and  $\vec{u}_v = \phi_f \vec{u}_f + \phi_p \vec{u}_p$  is the composite velocity.  $D_f/Dt$  and  $D_p/Dt$  refer to the material derivatives following the fluid and particle velocity fields, respectively. The volume fractions satisfy the identity  $\phi_f + \phi_p = 1$ ; hence, by adding the first two equations of (3.2),

$$\nabla \cdot \vec{u}_v = \nabla \cdot (\phi_f \vec{u}_f + \phi_p \vec{u}_p) = 0. \quad (3.3)$$

In the equilibrium Eulerian model, the velocity field of the particle phase,  $\vec{u}_p$ , is expanded about  $\tau_p = 0$  and defined in terms of  $\vec{u}_f$ . Given the density ratio parameter  $\beta = 3/(2\rho_p/\rho_f + 1)$ , for  $\beta \sim \mathcal{O}(1)$ , the following approximation holds up to  $\mathcal{O}(\tau_p^{3/2})$ :

$$\vec{u}_p \approx \vec{u}_f + \tau_p(1 - \beta) \left( \vec{g} - \frac{D_f \vec{u}_f}{Dt} \right), \quad (3.4)$$

For simplicity and to conform with existing computations [43, 44, 49, 50] for validation purposes, the inertial term of (3.4) is neglected, so that,

$$\vec{u}_p \approx \vec{u}_f + \tau_p(1 - \beta) \vec{g} = \vec{u}_f + u_s \vec{e}_g, \quad (3.5)$$

where  $u_s = \tau_p(1 - \beta)g$  is the settling velocity of the particles.

The fact that the particle velocity field is completely defined by the velocity field of the carrier fluid leads to the following question: how will the initial particle distribution affect the resulting particle velocity field? It is possible to prove that, for sufficiently small particle sizes, an *equilibrium* particle field exists such that it depends only on fluid quantities [40]. In essence, this means that the transients arising from the initial conditions decay exponentially fast when the characteristic time-scale  $\tau_p$  is much smaller than that of the fluid  $\tau_f$ .

It is important to take into account that certain circumstances exist in which the Stokes number  $\tau_p/\tau_f$  is small but the equilibrium condition does not hold. An example is the injection of particles into a fluid domain; near the point of injection, particle motion will be dominated by the injection process and only after an initial transient will it reach equilibrium with respect to the carrier fluid [52]. Furthermore, for increasing

particle concentrations, the mean time between particle collisions will decrease until it reaches the particle response time  $\tau_p$  and exerts a considerable effect on the particle velocity field.

Implicit in (3.5) is the assumption:

$$\frac{D_p \vec{u}_p}{Dt} \approx \frac{D_f \vec{u}_f}{Dt}. \quad (3.6)$$

Taking into account (3.6), the momentum equations in (3.2) can be combined in order to obtain

$$(\phi_f \rho_f + \phi_p \rho_p) \frac{D_f \vec{u}_f}{Dt} = -\nabla p + \mu \Delta \vec{u}_v + \phi_p (\rho_p - \rho_f) \vec{g}. \quad (3.7)$$

Considering that dilute suspensions are to be modeled and therefore  $\phi_p \ll 1$ , the composite velocity can be considered equal to the fluid velocity field, that is,  $\vec{u}_v \approx \vec{u}_f$ . By using (3.3), the conservation of mass for the fluid phase can be described with a divergence-free constraint,

$$\nabla \cdot \vec{u}_f \approx 0. \quad (3.8)$$

Finally, the Boussinesq approximation is assumed to hold, such that density variations are considered to be small and only influence the buoyancy term of (3.7). The density term on the left-hand side of (3.7) is assumed constant, such that  $(\phi_f \rho_f + \phi_p \rho_p) \approx \rho_f$ . In order to write the simplified equations of motion in non-dimensional form, a characteristic velocity, length and density are defined. The characteristic density is taken as  $\rho_f$  and, when considering a lock exchange flow, the characteristic length is taken as the height of the channel,  $H$ , see Figure 3.2. The buoyancy velocity, defined as

$$u_b = \sqrt{gH \frac{\rho_p - \rho_f}{\rho_f} \phi_{p,\max}}, \quad (3.9)$$

is used as the characteristic velocity.  $\phi_{p,\max}$  represents the maximum volumetric concentration of particles in the domain at the initial time instant. For simplicity of notation, the non-dimensional fluid velocity,  $\vec{u}_f$  will be represented with  $\vec{u}$  and the variable  $\phi = \phi_p / \phi_{p,\max}$  will be used as a normalized measure of particle concentration. The non-dimensional equations of motion are given by,

$$\begin{cases} \nabla \cdot \vec{u}, \\ \frac{\partial \vec{u}}{\partial t} + (\vec{u} \cdot \nabla) \vec{u} = -\nabla p + \frac{1}{\sqrt{\text{Gr}}} \Delta \vec{u} + \phi \vec{e}_g, \\ \frac{\partial \phi}{\partial t} + (\vec{u} + u_s \vec{e}_g) \cdot \nabla \phi = \frac{1}{\sqrt{\text{GrSc}^2}} \Delta \phi. \end{cases} \quad (3.10)$$

In Equation (3.10), a diffusion term has been added to the equation for conservation of particles. This is common practice when considering particle-laden flows, as it avoids the formation of sharp concentrations of particles that could lead to numerical instabilities [43, 44, 48]. Furthermore, certain authors indicate that this term has a physical significance, such as the spreading of particles in time due to hydrodynamic diffusion [44] or the departure of the equilibrium assumption due to close interaction of particles [48].

The two non-dimensional parameters that appear in (3.10) are the Grashof number  $\text{Gr}$  and the Schmidt number  $\text{Sc}$ , defined by

$$\text{Gr} = \left( \frac{u_b H}{\nu} \right)^2 \quad \text{and} \quad \text{Sc} = \frac{\nu}{\kappa}. \quad (3.11)$$

The Grashof number represents the ratio of buoyancy forces and viscous forces and it is proportional to  $\text{Re}^2$ . The Schmidt number compares the viscous diffusivity of the fluid to the molecular diffusivity of the particle field, given by  $\kappa$ .

### 3.3. THE 2D LOCK EXCHANGE FLOW

In this section, the 2D lock-exchange flow problem of a particle-driven current is presented together with the boundary conditions that will be prescribed in order to capture the deposition of sediment along the lower boundary. A lock-exchange flow consists of the mutual propagation of two flows with different densities which were initially separated by a membrane. Many physically relevant features of gravity currents can be observed in this type of flow, such as the body-head structure that gradually develops as the flow evolves [41,

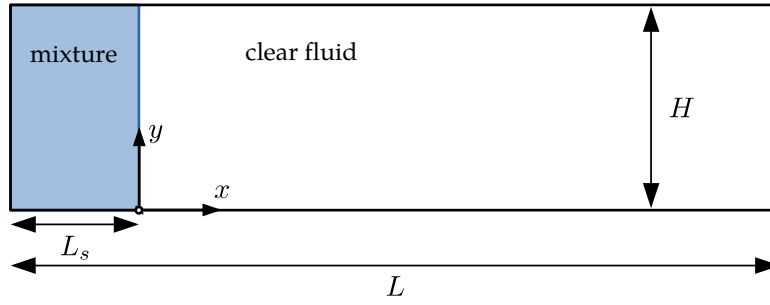


Figure 3.2: Initial set-up of the lock-exchange test-case to be computed in this work.

42, 48]. Extensive experimental studies have been carried out with lock-exchange flows [12]; more recently, direct numerical simulations have been used in order to capture more subtle physical aspects of the flow or to test numerical solvers for gravity currents [41–43, 45–50].

The initial set-up of the lock-exchange flow computed in this work is shown in Figure 3.2 and corresponds to the one presented by Necker et al. [43] and used in the work of Parkinson et al. [49] and Espath et al. [50]. The domain consists in a plane channel of height  $H$  and length  $L$ . At  $t = 0$ , a mixture of the particle phase and the fluid phase is contained in the region  $[-L_s, 0] \times [0, H]$ . For  $t > 0$ , the mixture is put in touch with the clear fluid and an intrusion front develops as the heavier fluid propagates along the lower boundary.

### 3.3.1. BOUNDARY CONDITIONS

In order to solve (3.10), boundary conditions must be given for the velocity  $\vec{u}$  and particle concentration  $\phi$ . Boundary conditions will be prescribed in the same way as Espath et al. [50], such that the lower wall allows for the convection of the flow particles at a settling velocity  $u_s$ . To this end, the boundary  $\partial\Omega$  is partitioned into 4 regions which correspond with the 4 faces of the rectangle, such that  $\partial\Omega = \cup \Gamma_i$ , for  $i = 1, 2, 3$  and 4, see Figure 3.3.

The velocity boundary conditions consist of no-slip conditions along the upper and lower walls, such that

$$\vec{u} = 0 \quad \text{on } \Gamma_1 \cup \Gamma_3, \quad (3.12)$$

and shear free conditions with no penetration along the lateral walls,

$$\vec{u} \cdot \vec{n} = 0 \quad \text{and} \quad \nabla \vec{u} \cdot \vec{n} = 0 \quad \text{on } \Gamma_2 \cup \Gamma_4. \quad (3.13)$$

Taking into account that (3.10) will be solved in a  $(\vec{u}, \omega, p)$  formulation, the shear-free boundary conditions can also be written in the following form,

$$\vec{u} \cdot \vec{n} = 0 \quad \text{and} \quad \omega = 0 \quad \text{on } \Gamma_2 \cup \Gamma_4. \quad (3.14)$$

A fundamental feature of turbidity currents is the deposition and resuspension of particles, which modifies the driving force of the current [48]. For the lock exchange flow, deposition of particles is assumed to occur on the lower boundary,  $\Gamma_3$ , due to advection with  $u_s \vec{e}_g$ . Over  $\Gamma_1 \cup \Gamma_2 \cup \Gamma_4$ , no particle transport is assumed to hold.

In order to understand how these boundary conditions can be prescribed, the transport equation for  $\phi$  must be integrated over the domain  $\Omega$ . Taking into account that  $\nabla \cdot \vec{u} = 0$  in  $\Omega$  and  $\vec{u} \cdot \vec{n} = 0$  on  $\partial\Omega$ , integrating the particle transport equation in (3.10) over  $\Omega$  yields the following result after applying the divergence theorem,

$$\frac{d}{dt} \int_{\Omega} \phi \, d\Omega = \int_{\partial\Omega} \left( -\phi u_s \vec{e}_g + \frac{1}{\sqrt{\text{GrSc}^2}} \nabla \phi \right) \cdot \vec{n} \, d\Gamma. \quad (3.15)$$

Therefore, if the boundary condition for  $\phi$  on  $\Gamma_1 \cup \Gamma_2 \cup \Gamma_4$  is zero particle flux, the integral in Equation (3.15) must be equal to zero, such that

$$\left( -\phi u_s \vec{e}_g + \frac{1}{\sqrt{\text{GrSc}^2}} \nabla \phi \right) \cdot \vec{n} = 0 \quad \text{on } \Gamma_1 \cup \Gamma_2 \cup \Gamma_4. \quad (3.16)$$

$$\Gamma_1 : \vec{u} = 0 \text{ and } -u_s \phi \vec{e}_g \cdot \vec{n} + \frac{1}{\sqrt{\text{GrSc}^2}} \nabla \phi \cdot \vec{n} = 0$$

$\Gamma_2 :$ $\vec{u} \cdot \vec{n} = 0,$ $\omega = 0$ and $\nabla \phi \cdot \vec{n} = 0$	$\Gamma_4 :$ $\vec{u} \cdot \vec{n} = 0,$ $\omega = 0$ and $\nabla \phi \cdot \vec{n} = 0$
---	---

$$\Gamma_3 : \vec{u} = 0 \text{ and } \nabla \phi \cdot \vec{n} = 0$$

Figure 3.3: Boundary conditions for the lock exchange test-case.

If the gravity vector is set to  $\vec{e}_g = (0, -1)$ , the following boundary conditions hold:

$$\begin{cases} -u_s \phi \vec{e}_g \cdot \vec{n} + \frac{1}{\sqrt{\text{GrSc}^2}} \nabla \phi \cdot \vec{n} = 0 & \text{on } \Gamma_1, \\ \nabla \phi \cdot \vec{n} = 0 & \text{on } \Gamma_2 \cup \Gamma_4. \end{cases} \quad (3.17)$$

Deposition of particles is enabled by assuming that the boundary condition over  $\Gamma_2$  is a particle flux at a velocity  $u_s$ . In order to do so, the dissipation term in (3.15) is eliminated, such that

$$\nabla \phi \cdot \vec{n} = 0 \quad \text{on } \Gamma_3. \quad (3.18)$$

Therefore, given the boundary conditions (3.17) and (3.18), the variation of the total particle concentration is determined with the following expression,

$$\frac{d}{dt} \int_{\Omega} \phi \, d\Omega = - \int_{\Gamma_3} \phi u_s \, d\Gamma. \quad (3.19)$$

### 3.4. FINITE ELEMENT DISCRETIZATION

The modified MEEVC scheme with kinematic Neumann boundary conditions, defined in Section 2.5.2, is adapted for the computation of the lock exchange flow presented in Section 3.3. The first step is to write (3.10) in the  $(\vec{u}, \omega, p)$  formulation of the MEEVC scheme:

$$\begin{cases} \frac{\partial \vec{u}}{\partial t} + \omega \times \vec{u} + \nabla \bar{p} = -\frac{1}{\sqrt{\text{Gr}}} \nabla \times \omega + \phi \vec{e}_g, \\ \frac{\partial \omega}{\partial t} + \frac{1}{2} (\vec{u} \cdot \nabla) \omega + \frac{1}{2} \nabla \cdot (\vec{u} \omega) = \frac{1}{\sqrt{\text{Gr}}} \Delta \omega + \nabla \phi \times \vec{e}_g, \\ \frac{\partial \phi}{\partial t} + \frac{1}{2} (\vec{u}_p \cdot \nabla) \phi + \frac{1}{2} \nabla \cdot (\vec{u}_p \phi) = \frac{1}{\sqrt{\text{GrSc}^2}} \Delta \phi, \\ \nabla \cdot \vec{u} = 0, \end{cases} \quad (3.20)$$

where  $\vec{u}_p = \vec{u} + u_s \vec{e}_g$  and the equality  $\nabla \times (\phi \vec{e}_g) = \nabla \phi \times \vec{e}_g$  has been used. The convective term for the particle transport equation has been written in skew-symmetric form to conserve the quadratic mean  $\langle \phi, \phi \rangle$  at the discrete level. Conservation of  $\langle \phi, \phi \rangle$  enforces  $\phi \geq 0$  over  $\Omega$  at the discrete level.

The next step is the construction of a weak formulation. The velocity  $\vec{u}$  is sought in the function space  $H_0(\text{div}, \Omega)$ , see (2.7), such that  $\vec{u} \cdot \vec{n} = 0$  is strongly prescribed along  $\partial\Omega$ . On the other hand, the vorticity  $\omega$  is assumed to be contained in the space  $H_{(2,4)}(\text{curl}, \Omega)$ , defined

$$H_{(2,4)}(\text{curl}, \Omega) = \{\omega \in H(\text{curl}, \Omega) \mid \omega = 0 \text{ on } \Gamma_2 \cup \Gamma_4\}. \quad (3.21)$$

The particle concentration  $\phi$  is to be found in the space of functions with square integrable gradients,  $H(\text{grad}, \Omega)$ . The boundary conditions, given by (3.17) and (3.18), must be imposed weakly by means of Neumann boundary conditions. After integrating by parts, the weak form of the particle transport equation is,

$$\begin{aligned} & \left\langle \frac{\partial \phi}{\partial t}, \zeta \right\rangle + \frac{1}{2} \langle \nabla \cdot (\bar{u}_p \phi), \zeta \rangle - \frac{1}{2} \langle \phi, \nabla \cdot (\bar{u}_p \zeta) \rangle + \frac{1}{2} \int_{\partial \Omega} \zeta \phi (\bar{u}_p \cdot \bar{n}) \, d\Gamma = \\ & = \frac{1}{\sqrt{\text{GrSc}^2}} \left[ -\langle \nabla \phi, \nabla \zeta \rangle + \int_{\partial \Omega} \zeta (\nabla \phi \cdot \bar{n}) \, d\Gamma \right], \quad \forall \zeta \in H(\text{grad}, \Omega). \end{aligned} \quad (3.22)$$

The term  $\nabla \phi \cdot \bar{n}$  is equal to zero along  $\Gamma_2 \cup \Gamma_3 \cup \Gamma_4$ . On the other hand,  $\bar{u}_p \cdot \bar{n} = u_s \bar{e}_g \cdot \bar{n}$  will be zero along the lateral faces,  $\Gamma_2 \cup \Gamma_4$ . Finally,  $\nabla \phi \cdot \bar{n} = -\sqrt{\text{GrSc}^2} \phi u_s (\bar{e}_g \cdot \bar{n})$  on  $\Gamma_1$ . These relations imply that (3.22) can be written as follows

$$\begin{aligned} & \left\langle \frac{\partial \phi}{\partial t}, \zeta \right\rangle + \frac{1}{2} \langle \nabla \cdot (\bar{u}_p \phi), \zeta \rangle - \frac{1}{2} \langle \phi, \nabla \cdot (\bar{u}_p \zeta) \rangle = \\ & = -\frac{1}{\sqrt{\text{GrSc}^2}} \langle \nabla \phi, \nabla \zeta \rangle + \int_{\Gamma_1} \zeta \phi u_s (\bar{e}_g \cdot \bar{n}) \, d\Gamma - \frac{1}{2} \int_{\Gamma_1 \cup \Gamma_3} \zeta \phi u_s (\bar{e}_g \cdot \bar{n}) \, d\Gamma = \\ & = -\frac{1}{\sqrt{\text{GrSc}^2}} \langle \nabla \phi, \nabla \zeta \rangle + \frac{1}{2} \int_{\Gamma_1} \zeta \phi u_s \, d\Gamma - \frac{1}{2} \int_{\Gamma_3} \zeta \phi u_s \, d\Gamma, \quad \forall \zeta \in H(\text{grad}, \Omega). \end{aligned} \quad (3.23)$$

The weak form of (3.20) can be written as

$$\left\{ \begin{array}{l} \text{Find } \bar{u} \in H_0(\text{div}, \Omega), \, p \in L^2(\Omega), \, \omega \in H_{(2,4)}(\text{curl}, \Omega) \text{ and } \phi \in H(\text{grad}, \Omega) \text{ such that:} \\ \left\langle \frac{\partial \bar{u}}{\partial t}, \bar{v} \right\rangle + \langle \omega \times \bar{u}, \bar{v} \rangle - \langle \bar{p}, \nabla \cdot \bar{v} \rangle = -\frac{1}{\sqrt{\text{Gr}}} \langle \nabla \times \omega, \bar{v} \rangle + \langle \phi \bar{e}_g, \bar{v} \rangle, \quad \forall \bar{v} \in H_0(\text{div}, \Omega), \\ \left\langle \frac{\partial \omega}{\partial t}, \xi \right\rangle + \frac{1}{2} \langle (\bar{u} \cdot \nabla) \omega, \xi \rangle + \frac{1}{2} \langle \nabla \cdot (\bar{u} \omega), \xi \rangle = \\ -\frac{1}{\sqrt{\text{Gr}}} \langle \nabla \times \omega, \nabla \times \xi \rangle + \frac{1}{\sqrt{\text{Gr}}} \int_{\partial \Omega} \xi (\nabla \times \bar{\omega}) \times \bar{n} \, d\Gamma + \langle \nabla \phi \times \bar{e}_g, \xi \rangle, \quad \forall \xi \in H_{(2,4)}(\text{curl}, \Omega), \\ \left\langle \frac{\partial \phi}{\partial t}, \zeta \right\rangle + \frac{1}{2} \langle \nabla \cdot (\bar{u}_p \phi), \zeta \rangle - \frac{1}{2} \langle \phi, \nabla \cdot (\bar{u}_p \zeta) \rangle = \\ -\frac{1}{\sqrt{\text{GrSc}^2}} \langle \nabla \phi, \nabla \zeta \rangle + \frac{1}{2} \int_{\Gamma_1} \zeta \phi u_s \, d\Gamma - \frac{1}{2} \int_{\Gamma_3} \zeta \phi u_s \, d\Gamma, \quad \forall \zeta \in H(\text{grad}, \Omega), \\ \langle \nabla \cdot \bar{u}, q \rangle = 0, \quad \forall q \in L^2(\Omega). \end{array} \right. \quad (3.24)$$

The finite element discretization of (3.24) can be developed once a set of finite element spaces is chosen for the variables, these are extended in terms of the basis functions and a time integrator is implemented. Following the steps taken in the MEEVC scheme with kinematic Neumann boundary conditions and taking into account that the space  $\text{CG}_N$  is chosen for  $\phi_h$ , the following algorithm is developed:

Given  $\bar{u}_h^{k+\frac{1}{2}}$ ,  $\omega_h^k$  and  $\phi^k$ ,

**Step 1.** Find  $\bar{\omega}_h^{k+1} \in \text{CG}_{N,(2,4)} = \{\omega_h \in \text{CG}_N \mid \omega_h = 0 \text{ on } \Gamma_2 \cup \Gamma_4\}$  such that:

$$\langle \bar{\omega}_h^{k+\frac{1}{2}}, \xi_h \rangle = \langle \bar{u}_h^{k+\frac{1}{2}}, \nabla \times \xi_h \rangle, \quad \forall \xi_h \in \text{CG}_{N,(2,4)}. \quad (3.25)$$

**Step 2.** Find  $\phi_h^{k+1} \in \text{CG}_N$  such that:

$$\begin{aligned} & \left\langle \frac{\phi_h^{k+1} - \phi_h^k}{\Delta t}, \zeta_h \right\rangle + \frac{1}{2} \langle \nabla \cdot \left( \left( \bar{u}_h^{k+\frac{1}{2}} + u_s \bar{e}_g \right) \frac{\phi_h^{k+1} + \phi_h^k}{2} \right), \zeta_h \rangle - \frac{1}{2} \left\langle \frac{\phi_h^{k+1} + \phi_h^k}{2}, \nabla \cdot \left( \left( \bar{u}_h^{k+\frac{1}{2}} + u_s \bar{e}_g \right) \zeta_h \right) \right\rangle = \\ & -\frac{1}{\sqrt{\text{GrSc}^2}} \langle \nabla \left( \frac{\phi_h^{k+1} + \phi_h^k}{2} \right), \nabla \zeta_h \rangle + \frac{1}{2} \int_{\Gamma_1} \zeta_h \frac{\phi_h^{k+1} + \phi_h^k}{2} u_s \, d\Gamma - \frac{1}{2} \int_{\Gamma_3} \zeta_h \frac{\phi_h^{k+1} + \phi_h^k}{2} u_s \, d\Gamma, \quad \forall \zeta_h \in \text{CG}_N \end{aligned} \quad (3.26)$$

**Step 3.** Find  $\omega_h^{k+1} \in \text{CG}_{N,(2,4)}$  such that:

$$\begin{aligned} & \left\langle \frac{\omega_h^{k+1} - \omega_h^k}{\Delta t}, \xi_h \right\rangle - \frac{1}{2} \left\langle \frac{\omega_h^{k+1} + \omega_h^k}{2}, \nabla \cdot \left( \bar{u}_h^{k+\frac{1}{2}} \xi_h \right) \right\rangle + \frac{1}{2} \langle \nabla \cdot \left( \bar{u}_h^{k+\frac{1}{2}} \frac{\omega_h^{k+1} + \omega_h^k}{2} \right), \xi \rangle = \\ & = -\frac{1}{\sqrt{\text{Gr}}} \langle \nabla \times \omega_h^{k+1}, \bar{v}_h \rangle + \frac{1}{\sqrt{\text{Gr}}} \int_{\partial \Omega} \xi_h (\nabla \times \bar{\omega}_h^{k+\frac{1}{2}}) \times \bar{n} \, d\Gamma + \langle \nabla \bar{\phi}_h^{k+\frac{1}{2}} \times \bar{e}_g, \xi_h \rangle, \quad \forall \xi_h \in \text{CG}_{N,(2,4)}, \end{aligned} \quad (3.27)$$

with

$$\tilde{\phi}_h^{k+\frac{1}{2}} = \frac{\phi_h^{k+1} + \phi_h^k}{2}. \quad (3.28)$$

**Step 4.** Find  $(\tilde{u}_h^{k+\frac{3}{2}}, \tilde{p}^{k+1}) \in (\text{RT}_{N,0}, \text{DG}_{N-1})$  such that:

$$\begin{cases} \left\langle \frac{\tilde{u}_h^{k+\frac{3}{2}} - \tilde{u}_h^{k+\frac{1}{2}}}{\Delta t}, \tilde{v}_h \right\rangle + \langle \omega_h^{k+1} \times \frac{\tilde{u}_h^{k+\frac{3}{2}} + \tilde{u}_h^{k+\frac{1}{2}}}{2}, \tilde{v}_h \rangle - \langle \tilde{p}_h^{k+1}, \nabla \cdot \tilde{v}_h \rangle = -\frac{1}{\sqrt{\text{Gr}}} \langle \nabla \times \omega_h^{k+1}, \tilde{v}_h \rangle + \langle \phi_h^{k+1} \tilde{e}_g, \tilde{v} \rangle, & \forall \tilde{v}_h \in \text{RT}_{(N,0)}, \\ \langle \nabla \cdot \tilde{u}_h^{k+\frac{3}{2}}, q_h \rangle = 0, & \forall q_h \in \text{DG}_{N-1}. \end{cases} \quad (3.29)$$

### 3.5. ENERGY BALANCE

The progressive conversion of potential energy into kinetic energy is the main mechanism that drives a turbidity current. The fluid motion decays over time due to viscous dissipation and the gradual loss of mass due to sedimentation. In this section, the energy balance equations are derived at the continuous level in the way of [43, 44, 49, 50]. Subsequently, the degree to which the discrete counterpart of the energy balance holds is analyzed.

#### 3.5.1. CONSERVATION OF ENERGY AT THE CONTINUOUS LEVEL

Denoting the potential energy by  $E_p$  and the viscous and sedimentation dissipation rates with  $\varepsilon_v$  and  $\varepsilon_s$ , the global energy equation of the flow is given by,

$$\frac{d}{dt} (\mathcal{K} + E_p) = -\varepsilon_v - \varepsilon_s. \quad (3.30)$$

An expression for the conservation of kinetic energy can be derived from the momentum equation in its weak formulation by specifying  $\tilde{v} = \tilde{u}$ , see (3.24), such that,

$$\frac{d\mathcal{K}}{dt} = -\frac{1}{\sqrt{\text{Gr}}} \langle \nabla \times \omega, \tilde{u} \rangle + \langle \phi \tilde{e}_g, \tilde{u} \rangle. \quad (3.31)$$

The potential energy, in its non-dimensional form, is defined,

$$E_p = \int_{\Omega} \phi y \, d\Omega, \quad (3.32)$$

such that its time derivative of  $E_p$  is given by,

$$\frac{dE_p}{dt} = \int_{\Omega} \frac{D\phi}{Dt} y \, d\Omega + \int_{\Omega} \phi \frac{Dy}{Dt} \, d\Omega = \left\langle \frac{D\phi}{Dt}, y \right\rangle - \langle \phi, \tilde{u} \cdot \tilde{e}_g \rangle. \quad (3.33)$$

Given (3.33), the term  $\langle \phi, \tilde{u} \cdot \tilde{e}_g \rangle$  in (3.31) can be written as a function of  $E_p$ . Therefore, the energy budget equation can be written as

$$\frac{d\mathcal{K}}{dt} + \frac{dE_p}{dt} = -\frac{1}{\sqrt{\text{Gr}}} \langle \nabla \times \omega, \tilde{u} \rangle + \left\langle \frac{D\phi}{Dt}, y \right\rangle. \quad (3.34)$$

This equation yields an expression for the dissipation terms due to viscosity, denoted  $\varepsilon_v$ , and sedimentation,  $\varepsilon_s$ , such that,

$$\varepsilon_v = \frac{1}{\sqrt{\text{Gr}}} \langle \nabla \times \omega, \tilde{u} \rangle, \quad (3.35)$$

$$\varepsilon_s = -\left\langle \frac{D\phi}{Dt}, y \right\rangle. \quad (3.36)$$

A simpler expression can be found for (3.36) that does not require derivation over time. In the particle transport equation, the advection velocity is  $\tilde{u}_p = \tilde{u} + u_s \tilde{e}_g$ . Taking into account that  $u_s$  is constant, see (3.5), the particle transport equation takes the following form for  $\zeta = y$ ,

$$\left\langle \frac{D\phi}{Dt}, y \right\rangle = -u_s \langle \nabla \phi \cdot \tilde{e}_g, y \rangle - \frac{1}{\sqrt{\text{GrSc}^2}} \left( \langle \nabla \phi, \nabla y \rangle - \int_{\partial\Omega} y \nabla \phi \cdot \tilde{n} \, d\Gamma \right). \quad (3.37)$$

The first term in (3.37) can be integrated by parts,

$$\begin{aligned} -u_s \langle \nabla \phi \cdot \vec{e}_g, y \rangle &= u_s \langle \phi, \nabla y \cdot \vec{e}_g \rangle - u_s \int_{\partial\Omega} \phi y (\vec{e}_g \cdot \vec{n}) \, d\Gamma \\ &= -u_s \langle \phi, 1 \rangle + 2u_s \int_{\Gamma_1} \phi \, d\Gamma, \end{aligned} \quad (3.38)$$

and, taking into account boundary conditions (3.17) and (3.18), the boundary term in (3.37) results in,

$$\frac{1}{\sqrt{\text{GrSc}^2}} \int_{\partial\Omega} y \nabla \phi \cdot \vec{n} \, d\Gamma = -2u_s \int_{\Gamma_1} \phi \, d\Gamma. \quad (3.39)$$

Therefore, (3.37) can be written as follows,

$$\left\langle \frac{D\phi}{Dt}, y \right\rangle = -u_s \langle \phi, 1 \rangle + \frac{1}{\sqrt{\text{GrSc}^2}} \langle \nabla \phi, \vec{e}_g \rangle, \quad (3.40)$$

such that  $\epsilon_s$  corresponds with

$$\epsilon_s = u_s \langle \phi, 1 \rangle - \frac{1}{\sqrt{\text{GrSc}^2}} \langle \nabla \phi, \vec{e}_g \rangle. \quad (3.41)$$

The energy balance of a turbidity current is generally written in terms of time integrated values [43, 44, 49, 50]. Equation (3.31) can be written as follows,

$$\mathcal{K} + E_p + E_v + E_s = \mathcal{K}_0 + E_{p,0}, \quad (3.42)$$

where  $\mathcal{K}_0$  and  $E_{p,0}$  are the initial kinetic and potential energy and  $E_v$  and  $E_s$  are the total energy losses to viscous dissipation and suspended particles.  $E_v$  and  $E_s$  are given by

$$E_v = \int_0^t \epsilon_v \, d\tau \quad \text{and} \quad E_s = \int_0^t \epsilon_s \, d\tau. \quad (3.43)$$

### 3.5.2. CONSERVATION OF ENERGY AT THE DISCRETE LEVEL

A discrete energy balance equation, equivalent to (3.42), can be derived from the discretized equations of motion, given by (3.25) to (3.29). The discretized energy balance equation is constructed by imitating the derivation carried out in Section 3.5.1 and taking into account which steps and vector identities are exact at the discrete level.

A discrete statement of the conservation of kinetic energy can be written by setting  $\vec{v}_h = \frac{1}{2} \vec{u}_h^{k+\frac{3}{2}} + \frac{1}{2} \vec{u}_h^{k+\frac{1}{2}}$  in the discrete momentum equation. In the same way as presented in Section 2.6.3, the following equation can be derived,

$$\frac{1}{2} \langle \vec{u}_h^{k+\frac{3}{2}}, \vec{u}_h^{k+\frac{3}{2}} \rangle - \frac{1}{2} \langle \vec{u}_h^{k+\frac{1}{2}}, \vec{u}_h^{k+\frac{1}{2}} \rangle = -\frac{\Delta t}{\sqrt{\text{Gr}}} \langle \nabla \times \omega_h^{k+1}, \frac{\vec{u}_h^{k+\frac{3}{2}} + \vec{u}_h^{k+\frac{1}{2}}}{2} \rangle + \Delta t \langle \phi^{k+1} \vec{e}_g, \frac{\vec{u}_h^{k+\frac{3}{2}} + \vec{u}_h^{k+\frac{1}{2}}}{2} \rangle. \quad (3.44)$$

The discrete kinetic energy  $\mathcal{K}_h^{k+1}$  is defined in (2.44). The discrete counterpart of  $\epsilon_v$  is defined as,

$$\epsilon_{v,h}^{k+1} = \frac{1}{\sqrt{\text{Gr}}} \langle \nabla \times \omega_h^{k+1}, \frac{\vec{u}_h^{k+\frac{3}{2}} + \vec{u}_h^{k+\frac{1}{2}}}{2} \rangle. \quad (3.45)$$

Therefore, Equation (3.44) can be written as follows,

$$\mathcal{K}_h^{k+1} - \mathcal{K}_h^k = -\Delta t \epsilon_{v,h}^{k+1} + \Delta t \langle \phi^{k+1} \vec{e}_g, \frac{\vec{u}_h^{k+\frac{3}{2}} + \vec{u}_h^{k+\frac{1}{2}}}{2} \rangle. \quad (3.46)$$

The potential energy and the dissipation due to sedimentation can be introduced by using the discrete transport equation for the particle phase, Equation (3.26). To this end, the discrete test function is set to  $\zeta_h = y$  and the convective terms are rewritten as follows,

$$\frac{1}{2} \langle \nabla \cdot \left( \vec{u}_h^{k+\frac{1}{2}} \frac{\phi_h^{k+1} + \phi_h^k}{2} \right), y \rangle - \frac{1}{2} \langle \frac{\phi_h^{k+1} + \phi_h^k}{2}, \nabla \cdot \left( \vec{u}_h^{k+\frac{1}{2}} y \right) \rangle = \langle \vec{\phi}^{k+\frac{1}{2}}, \vec{u}_h^{k+\frac{1}{2}} \cdot \vec{e}_g \rangle, \quad (3.47)$$

$$\frac{1}{2} \langle \nabla \cdot \left( u_s \bar{e}_g \frac{\phi_h^{k+1} + \phi_h^k}{2} \right), y \rangle - \frac{1}{2} \left\langle \frac{\phi_h^{k+1} + \phi_h^k}{2}, \nabla \cdot (u_s \bar{e}_g y) \right\rangle + \frac{1}{2} \int_{\Gamma_1} y \frac{\phi_h^{k+1} + \phi_h^k}{2} u_s (\bar{e}_g \cdot \bar{n}) \, d\Gamma = -u_s \langle \bar{\phi}_h^{k+\frac{1}{2}}, 1 \rangle, \quad (3.48)$$

where integration by parts has been applied on the first terms in both cases, an operation which is exact at the discrete level because  $\nabla \cdot \bar{u}_h = 0$  and  $\bar{u}_h \cdot \bar{n} = 0$ . For simplicity of notation,  $\bar{\phi}_h^{k+\frac{1}{2}}$  is used, see (3.28). The discrete counterparts of  $E_p$  and  $\epsilon_s$  are defined as,

$$E_{p,h}^k = \langle \phi_h^k, y \rangle, \quad (3.49)$$

$$\epsilon_{s,h}^k = u_s \langle \bar{\phi}_h^k, 1 \rangle - \frac{1}{\sqrt{\text{GrSc}^2}} \langle \nabla \bar{\phi}_h^k, \bar{e}_g \rangle, \quad (3.50)$$

such that (3.26) can be rewritten as follows,

$$E_{p,h}^{k+1} - E_{p,h}^k = -\Delta t \epsilon_{s,h}^{k+\frac{1}{2}} - \Delta t \left\langle \frac{\phi_h^{k+1} + \phi_h^k}{2} \bar{e}_g, \bar{u}_h^{k+\frac{1}{2}} \right\rangle. \quad (3.51)$$

A discrete energy balance equation analogous to (3.30) is obtained by summing (3.46) and (3.51),

$$\mathcal{K}_h^{k+\frac{3}{2}} + E_{p,h}^{k+1} = \mathcal{K}_h^{k+\frac{1}{2}} + E_{p,h}^k - \Delta t \left( \epsilon_{v,h}^{k+1} + \epsilon_{s,h}^{k+\frac{1}{2}} \right) + \frac{\Delta t}{2} \left( \langle \phi_h^{k+1} \bar{e}_g, \bar{u}_h^{k+\frac{3}{2}} \rangle - \langle \phi_h^k \bar{e}_g, \bar{u}_h^{k+\frac{1}{2}} \rangle \right). \quad (3.52)$$

The last term in (3.52) is a residual term due to the staggering in time of the momentum equation with respect to particle transport equation. The temporal evolution of the residual can be understood by deriving the integral form of (3.52). The following expressions are obtained at the time iterations  $k, k-1, \dots, 1$  and  $0$ :

$$\begin{aligned} \mathcal{K}_h^{k+\frac{3}{2}} + E_{p,h}^{k+1} &= \mathcal{K}_h^{k+\frac{1}{2}} + E_{p,h}^k - \Delta t \left( \epsilon_{v,h}^{k+1} + \epsilon_{s,h}^{k+\frac{1}{2}} \right) + \frac{\Delta t}{2} \left( \langle \phi_h^{k+1} \bar{e}_g, \bar{u}_h^{k+\frac{3}{2}} \rangle - \langle \phi_h^k \bar{e}_g, \bar{u}_h^{k+\frac{1}{2}} \rangle \right), \\ \mathcal{K}_h^{k+\frac{1}{2}} + E_{p,h}^k &= \mathcal{K}_h^{k-\frac{1}{2}} + E_{p,h}^{k-1} - \Delta t \left( \epsilon_{v,h}^k + \epsilon_{s,h}^{k-\frac{1}{2}} \right) + \frac{\Delta t}{2} \left( \langle \phi_h^k \bar{e}_g, \bar{u}_h^{k+\frac{1}{2}} \rangle - \langle \phi_h^{k-1} \bar{e}_g, \bar{u}_h^{k-\frac{1}{2}} \rangle \right), \\ &\vdots \\ \mathcal{K}_h^{\frac{5}{2}} + E_{p,h}^2 &= \mathcal{K}_h^{\frac{3}{2}} + E_{p,h}^1 - \Delta t \left( \epsilon_{v,h}^2 + \epsilon_{s,h}^{\frac{3}{2}} \right) + \frac{\Delta t}{2} \left( \langle \phi_h^2 \bar{e}_g, \bar{u}_h^{\frac{5}{2}} \rangle - \langle \phi_h^1 \bar{e}_g, \bar{u}_h^{\frac{3}{2}} \rangle \right), \\ \mathcal{K}_h^{\frac{3}{2}} + E_{p,h}^1 &= \mathcal{K}_h^{\frac{1}{2}} + E_{p,h}^0 - \Delta t \left( \epsilon_{v,h}^1 + \epsilon_{s,h}^{\frac{1}{2}} \right) + \frac{\Delta t}{2} \left( \langle \phi_h^1 \bar{e}_g, \bar{u}_h^{\frac{3}{2}} \rangle - \langle \phi_h^0 \bar{e}_g, \bar{u}_h^{\frac{1}{2}} \rangle \right). \end{aligned}$$

The summation of all the energy balance equations from  $t^{k+1}$  to  $t^1$  produces the following result,

$$\mathcal{K}_h^{k+\frac{3}{2}} + E_{p,h}^{k+1} = \mathcal{K}_h^{\frac{1}{2}} + E_{p,h}^0 - \Delta t \sum_{i=1}^{k+1} \left( \epsilon_{v,h}^i + \epsilon_{s,h}^{i-\frac{1}{2}} \right) + \frac{\Delta t}{2} \left( \langle \phi_h^{k+1} \bar{e}_g, \bar{u}_h^{k+\frac{3}{2}} \rangle - \langle \phi_h^0 \bar{e}_g, \bar{u}_h^{\frac{1}{2}} \rangle \right). \quad (3.53)$$

Given the discrete counterpart of the total dissipated energy,

$$E_{v,h}^{k+1} = \Delta t \sum_{i=1}^{k+1} \epsilon_{v,h}^i \quad \text{and} \quad E_{s,h}^{k+\frac{1}{2}} = \Delta t \sum_{i=1}^{k+1} \epsilon_{s,h}^{i-\frac{1}{2}}, \quad (3.54)$$

an integral energy balance equation for the discrete system can be derived,

$$\mathcal{K}_h^{k+\frac{3}{2}} + E_{p,h}^{k+1} + E_{v,h}^{k+1} + E_{s,h}^{k+\frac{1}{2}} = \mathcal{K}_h^{\frac{1}{2}} + E_{p,h}^0 + \frac{\Delta t}{2} \left( \langle \phi_h^{k+1} \bar{e}_g, \bar{u}_h^{k+\frac{3}{2}} \rangle - \langle \phi_h^0 \bar{e}_g, \bar{u}_h^{\frac{1}{2}} \rangle \right). \quad (3.55)$$

Equation (3.55) indicates that, due to staggering in time, a discrete statement for the conservation of energy cannot be exact because the different components of the energy are known at different time instants. The residual term of (3.55) is not a sink/source of energy because it is not accumulated over time, it quantifies the level of mismatch between the staggered variables in time. It is proportional only to  $\Delta t$ .

### 3.6. NUMERICAL RESULTS

In this section, results are shown for the lock exchange test case described in Section 3.3. The objective of this section is to validate the modified MEEVC scheme and its robustness. In order to do so, 3 simulations are carried out with different levels of refinement and the results are compared with those given by Parkinson et al. [49] and Espath et al. [50].

In these computations, the Grashof and the Schmidt numbers are set to  $Gr = 5 \times 10^6$  ( $Re \approx 2236$ ) and  $Sc = 1$ . The simulations presented in the literature compute the flow problem up to  $t = 60$  for a domain of length  $L = 19$ . The references used for the comparison, denoted Ref. 1 and Ref. 2 hereafter, are briefly explained below.

- **Ref. 1**, Parkinson et al. [49]. A mixed finite element method based on discontinuous Galerkin (DG) elements is used, with linear elements for  $\bar{u}$  and  $\phi$  and quadratic elements for  $p$ . A Crank-Nicolson time discretization is used and the resulting non-linear system of equations is solved using two Picard iterations. Fixed and highly adaptive meshes are used. Unlike the boundary conditions presented in Section 3.3.1,  $\phi = 0$  is prescribed along the top boundary, resulting in a loss of  $< 1\%$  of mass and  $\sim 3\%$  of the total energy.
- **Ref. 2**, Espath et al. [50]. A compact sixth-order finite difference scheme is used for the spatial discretization and a third order Adams-Bashforth scheme for time integration.

In total, 3 simulations are carried out with the modified MEEVC scheme; these are denoted by Sim 1, 2 and 3 and the discretization parameters can be found in Table 3.1. Due to the lack of available computing power (see Section 1.5 for details of the workstation), the simulations are computed from  $t = 0$  to  $t = 12$  and in a domain of length  $L = 13$ . At  $t = 12$ , the particle flow is far from reaching the opposite wall and the difference in domain length with the references should not modify the results. According to Härtel et al. [41], the propagating front remains unaffected by the wall up to a distance of  $2H$ , a condition satisfied in these computations.

In all of the simulations, the time step is set to  $\Delta t = 10^{-3}$ , following Espath et al. [50]. An “equivalent number of cells” is calculated in order to facilitate comparisons, defined

$$\text{eq. num. cells} = \text{num. cells} \times \frac{19}{13} \times N^2, \quad (3.56)$$

such that the domain is extended to  $L = 19$  and the polynomial order is accounted for by triangulating each element into  $N^2$  cells. The meshes used in the simulations are depicted in Figure 3.7.

Figure 3.7 displays the color plots of the particle concentration at  $t = 4$  and 12, together with the corresponding meshes. Color plots from Parkinson et al. [49] are also shown because they illustrate the effects of mesh refinement and a mixed finite element method is also used. The first plot is a low resolution computation with a fixed mesh, while the second and third plots are high resolution computations with a fixed and an adaptive mesh, respectively. These last two plots are of approximately the same degree of accuracy [49].

The particle concentration fields obtained with the modified MEEVC scheme resemble the high resolution reference results for  $t = 4$ . For  $t = 4$ , an intrusion front has fully developed and a vortical structure, characteristic of Kelvin-Helmholtz instabilities, are present along the upper interface. The reference results display two vortexes along the upper interface, although for the low resolution case these are highly dissipated. With the MEEVC scheme these two vortexes are captured, even with the lowest resolution. Interestingly, a third vortex appears in all of the MEEVC scheme computations. Possible differences could be due to the different ways in which boundary conditions are prescribed, to the highly dissipative nature of the reference scheme or to under resolved structures in the MEEVC scheme.

Table 3.1: Discretization parameters of the three simulations carried out with the modified MEEVC scheme. The Grashof and the Schmidt numbers are set to  $Gr = 5 \times 10^6$  and  $Sc = 1$ .

id	$N$	num. cells	eq. num. cells	$\Delta t$	$d_W$	$d_U$	$d_Q$
Sim 1	4	1116	$2.6 \times 10^4$	$10^{-3}$	9169	20328	11160
Sim 2	4	2399	$5.6 \times 10^4$	$10^{-3}$	19587	43576	23990
Sim 3	4	3599	$8.4 \times 10^4$	$10^{-3}$	29283	65272	35990

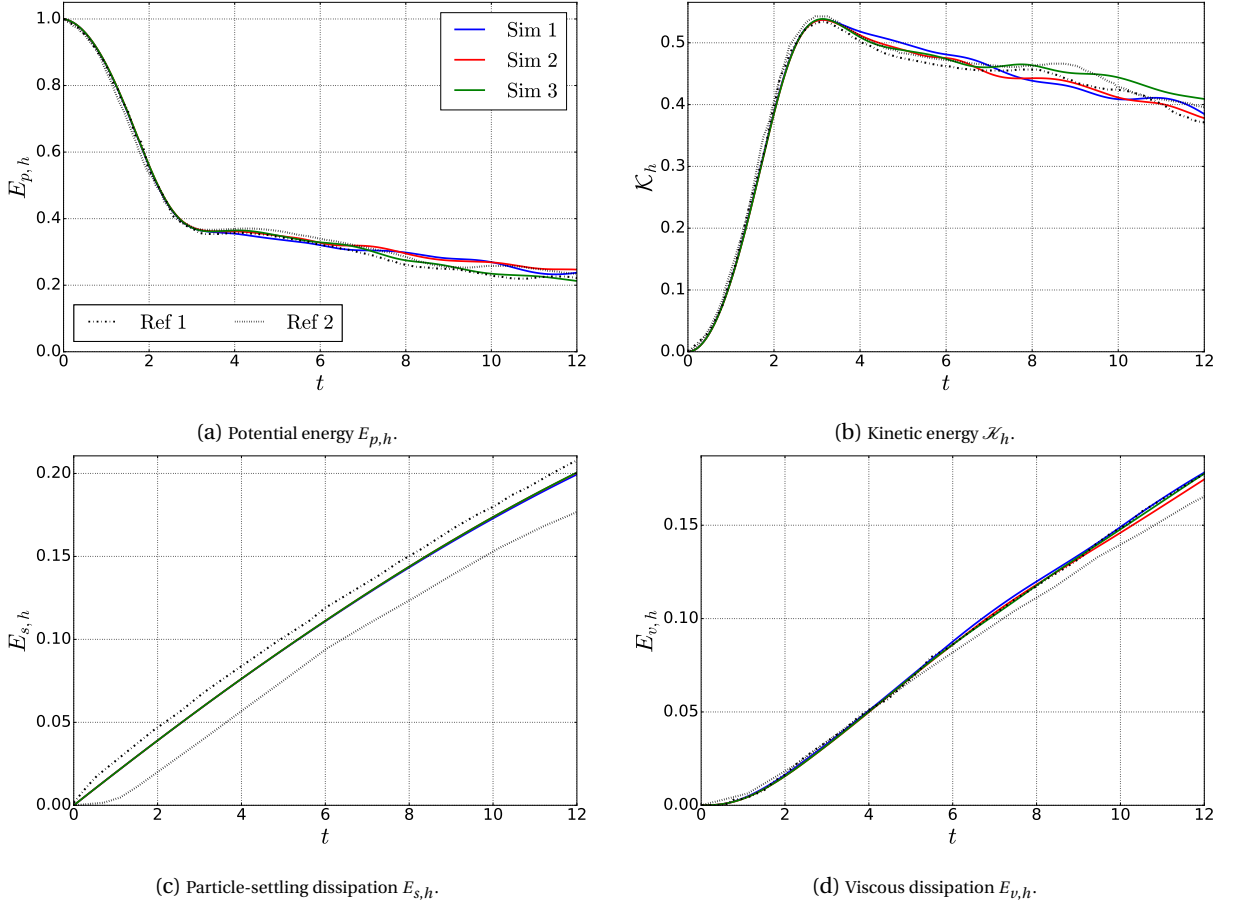


Figure 3.4: Variation over time of the 4 components of the energy balance equation. Results are compared with those of [49, 50].

For  $t = 12$ , large variations appear from one computation to another. According to Parkinson et al. [49], no two simulations ever produced the same results. This is due to the highly chaotic nature of the flow; vortices are generated and propagated in such a way that small variations in the mesh induce small variations in these vortices which grow and propagate over time. However, in the two highly-resolved computations from the reference, three distinct vortical structures, suspended over the remains of the intrusion front, can be observed. These structures can also be observed in the three computations carried out with the MEEVC scheme. Considerable variations in the shape and position of these structures are found from Sim 2 to Sim 3. It must be taken into account that spatial convergence would require more computational power and it is not priority in this work.

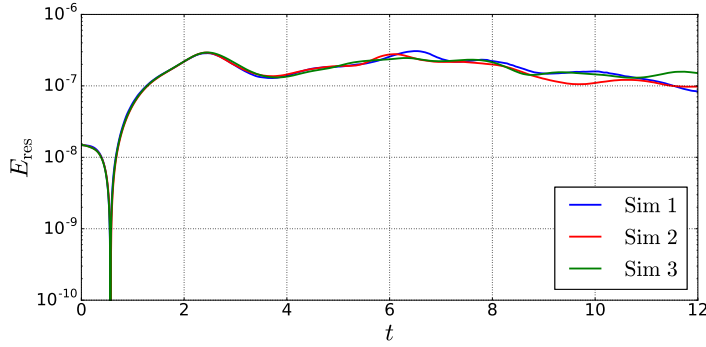
In Figure 3.4, the evolution of the 4 discrete energy components can be found, see (3.42). The kinetic and potential energy are very similar for  $t < 3$ . Until  $t = 6$ , Sim 2 and 3 yield similar results. For  $t > 6$ , vortex interaction becomes stronger and the three simulations differ considerably. It can be concluded that, in general, good agreement can be found between the MEEVC computations and those of the references.

For the particle-settling dissipation, hardly no difference is found between the three MEEVC simulations. The values for  $E_{s,h}$  given by the references differ from each other and from the MEEVC scheme along the entire computation. Parkinson et al. use different boundary conditions at the top wall and the two references use a different expression for  $\epsilon_s$ . Although these are equivalent at the continuous level, the discrete expressions may differ. Parkinson et al. calculate  $\epsilon_s$  with

$$\epsilon_{s,\text{ref 1}} = -u_s \langle \vec{e}_g, \nabla \phi \rangle - \frac{1}{\sqrt{\text{GrSc}^2}} \left\{ \langle \nabla \phi, \nabla y \rangle - \int_{\partial\Omega} y \nabla \phi \cdot \vec{n} \, d\Gamma \right\}, \quad (3.57)$$

and Espath et al. use,

$$\epsilon_{s,\text{ref 2}} = -u_s \langle \vec{e}_g, \nabla \phi \rangle + \frac{1}{\sqrt{\text{GrSc}^2}} \langle \Delta \phi, y \rangle. \quad (3.58)$$

Figure 3.5: Energy residual  $E_{res}$ .

A powerful advantage of the MEEVC scheme is the energy conserving properties. Figure 3.5 displays the evolution of the energy residual,  $E_{res}$ , defined,

$$E_{res}^k = \mathcal{K}_h^k + E_{p,h}^k + E_{v,h}^k + E_{s,h}^k - E_{p,h}^0 - \mathcal{K}^0, \quad (3.59)$$

where  $\mathcal{K}_h^k = \frac{1}{2}(\mathcal{K}_h^{k+\frac{3}{2}} + \mathcal{K}_h^{k+\frac{1}{2}})$ . As expected, this term remains stable and bounded to relatively small values, indicating a lack of artificial dissipation. This error is only due to the staggering in time of the velocity, see (3.55)<sup>1</sup>.

Three of the main features of a turbidity current are the location of the front  $x_f$ , the mass of suspended particles  $m_p$  and the sedimentation rate  $\dot{m}_s$ . The evolution of these variables is shown in Figure 3.6, together with data from Espath et al. [50]. The calculated values for the location of the front and the total suspended mass agree with the reference results. This last variable is defined as

$$\frac{m_p}{m_{p,0}} = \frac{1}{m_{p,0}} \int_{\Omega} \phi \, d\Omega, \quad \text{with} \quad m_{p,0} = \int_{\Omega} \phi(t=0) \, d\Omega. \quad (3.60)$$

The variation of  $m_p$ , denoted  $\dot{m}_s$ , is defined as

$$\dot{m}_s = - \int_{\Gamma_3} \phi u_s \, d\Gamma, \quad (3.61)$$

see (3.3.1) for a derivation. Figure 3.6c indicates that the results from Sim 2 and 3 are in great agreement and that a similar tendency to that of the reference is obtained. On the other hand, the results from Sim 1 show a more chaotic behavior.

<sup>1</sup>The expression given in (3.55) for the residual was not derived until a few days before the hand-in of this document. There was not enough time to repeat the simulations in order to gather the required data for the calculation of the residual and give a more precise proof.

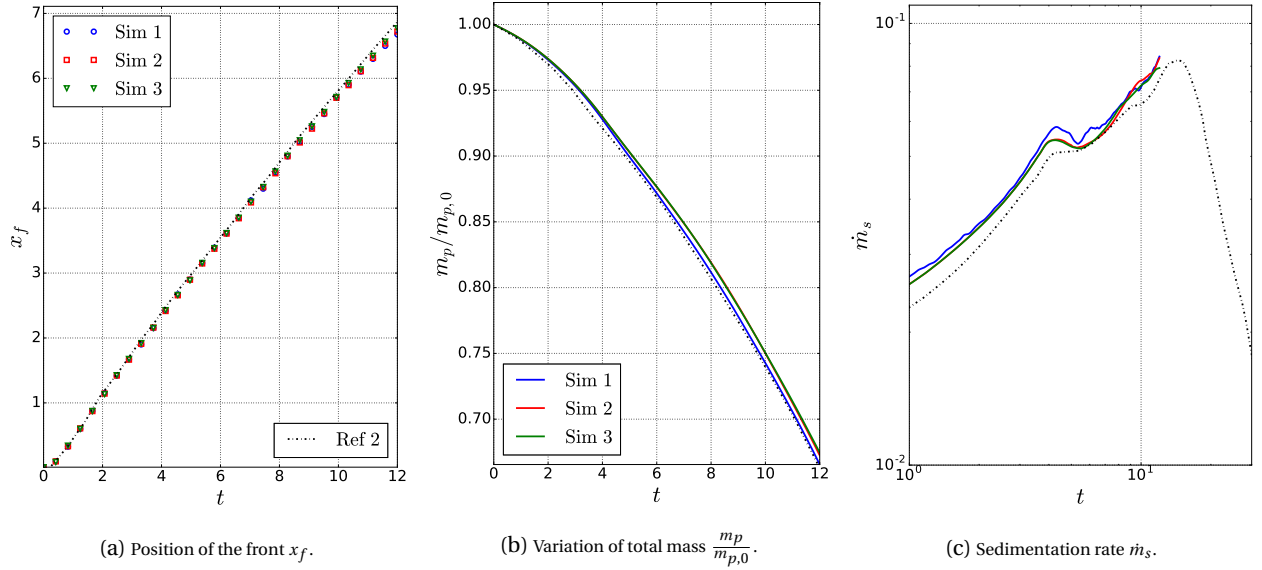


Figure 3.6: Variation over time of the location of the front, the suspended mass and the sedimentation rate. Comparisons are made with the results from [50].

### 3.7. CONCLUDING REMARKS

In this chapter, a physics-compatible solver for turbidity currents is constructed from the MEEVC scheme with kinematic Neumann boundary conditions. It is proved that the discrete energy balance equation holds up to a residual which does not accumulate over time and is due to the staggering in time of the velocity. With the finite element basis functions used for the velocity and the pressure,  $\nabla \cdot \vec{u}_h = 0$  over  $\Omega$  and certain vector calculus identities required for the derivation of the energy balance equation hold at the discrete level. Essentially, the discrete kinetic and potential energy are only lost to the viscous and sedimentation terms, and no artificial dissipation of energy is introduced.

This solver is validated by computing the lock exchange test case for  $Gr = 5 \times 10^6$  ( $Re \approx 2236$ ) with three different meshes of increasing refinement. Comparisons are made with Parkinson et al. [49] and Espath et al. [50], and these indicate that the essential dynamics and vortical structures are captured with the lowest resolution. Further features of the flow are computed and compared with the reference results, showing very good agreement in general.

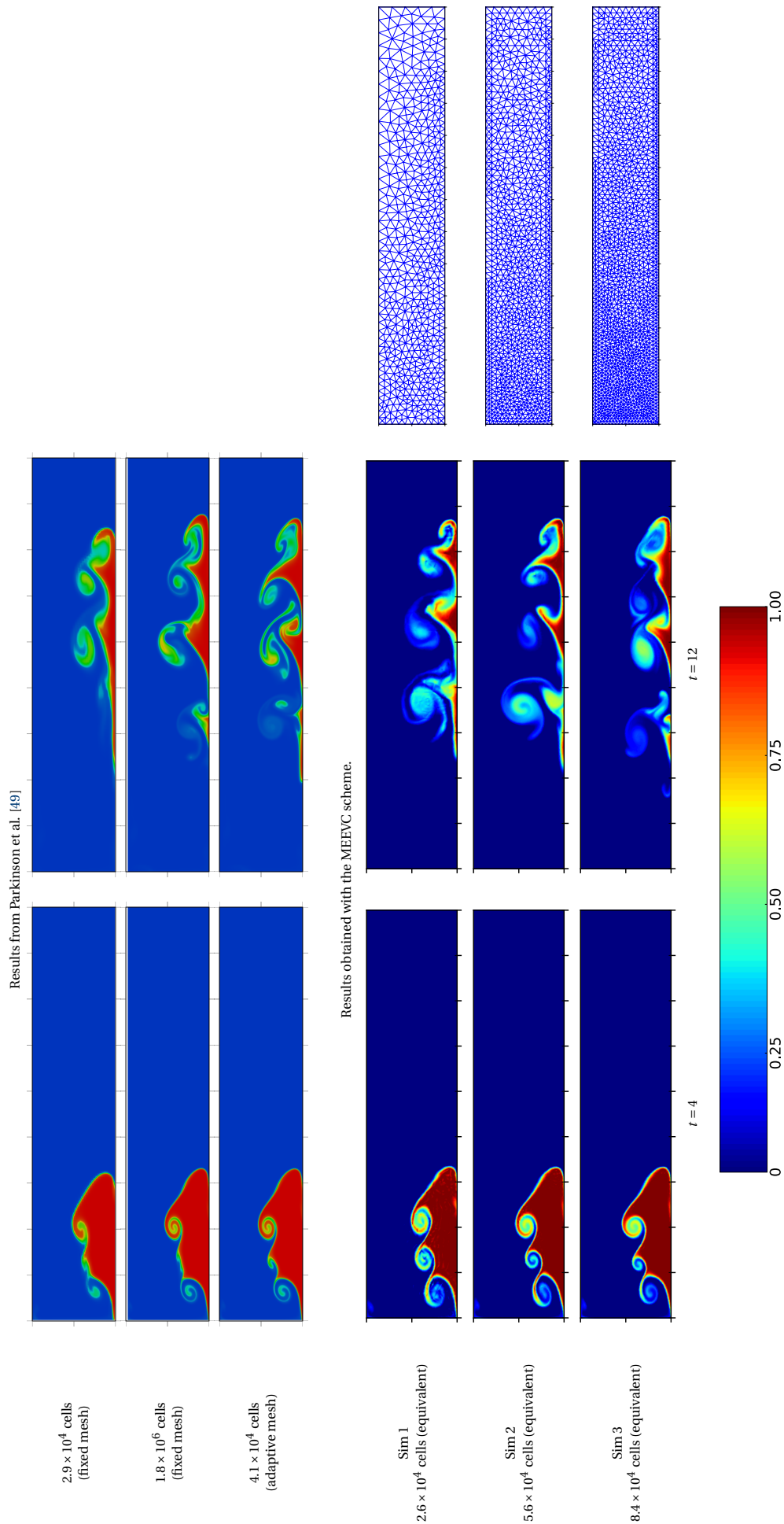


Figure 3.7: Distribution of particle concentration at  $t = 4$  and  $12$  obtained with the three discretizations described in Table 3.1, together with the corresponding meshes. Three sets of results from [49] are also presented.



# 4

## CONCLUSIONS AND FURTHER RESEARCH

This thesis represents a continuation of the work from Palha and Gerritsma [11] in which different ideas from physics-compatible methods are brought together to create a robust solver for the 2D incompressible Navier-Stokes equations with periodic boundary conditions. In this work, the MEEVC scheme, which conserves mass, energy, enstrophy and vorticity, is extended for the construction of a turbidity current solver. This extension is carried out in two separate steps: slip boundary conditions are implemented, see Chapter 2, and a model based on the 2D incompressible Navier-Stokes equations for particle-laden flows is discretized, see Chapter 3.

In this final chapter, the conclusions drawn from this project are stated, together with further research that can continue this work. The two main chapters of this work lead to fundamentally different conclusions and therefore two separate sections dedicated to the corresponding chapters can be found below.

### 4.1. PRESCRIPTION OF SLIP BOUNDARY CONDITIONS

In the MEEVC scheme, the velocity is sought in the function space  $H(\text{div}, \Omega)$  and the tangential velocity component along the boundary is not defined. From a numerical point of view,  $H(\text{div}, \Omega)$  conforming finite element spaces, like the Raviart-Thomas elements used in the MEEVC scheme, ensure continuity of the normal vector components across the edges of the elements. Hence, the degrees of freedom of the approximate velocity are based on fluxes across the edges and tangential boundary conditions cannot be prescribed strongly.

In Chapter 2, a solution to this problem is proposed in which the slip velocity is enforced by means of vorticity boundary conditions. Three methods for prescribing slip boundary conditions are described; these are based on local relations between vorticity and velocity. Of those methods, two are constructed with the kinematic relation,  $\omega = \nabla \times \vec{u}$ , and the remaining one with the tangential component of the momentum equation (a dynamic relation). One of the kinematic approaches and the dynamic approach make use of Neumann boundary conditions, while the other kinematic approach specifies the vorticity values in a Dirichlet manner. These are denoted kinematic Neumann, dynamic Neumann and kinematic Dirichlet boundary conditions, respectively.

The three methods are evaluated and compared by computing two numerical test cases, the Taylor-Green vortex and the dipole collision. The results indicate that kinematic Neumann boundary conditions yield the highest convergence rates for the velocity and the vorticity. Unlike the other two methods, the vorticity near the wall does not present artificial oscillations. Furthermore, the dipole collision is computed for  $\nu = 0$  and it is proved that only kinematic Neumann boundary conditions respect the inviscid limit.

Chapter 2 concludes that kinematic Neumann boundary conditions are the most adequate for the construction of a solver for turbidity currents. With these boundary conditions, the mass, energy and enstrophy conservation properties remain unaltered. However, vorticity conservation is destroyed and, as a preliminary solution, a compatibility condition is proposed in Appendix A for the conservation of vorticity in domains bounded by closed curves.

The results from this work suggest that, for the prescription of slip boundary conditions, information from the adjoint de Rham complex [9] is required. This complex is dual to the continuous counterpart of (2.22) and the pressure is sought in  $H(\text{grad}, \Omega)$ , the velocity in  $H(\text{curl}, \Omega)$  and the vorticity in  $L^2(\Omega)$ . A possibility to be explored is a dual finite element method in which the complexes are discretized in a primal and

dual mesh, respectively, and normal and tangential velocity boundary conditions are strongly imposed in the corresponding spaces.

Further research to be done is the extension to 3D of the MEEVC scheme and the subsequent prescription of slip boundary conditions. In 3D, enstrophy is no longer conserved and helicity becomes an invariant of fundamental importance in the study of turbulence [54].

## 4.2. DEVELOPMENT OF A SOLVER FOR TURBIDITY CURRENTS

In Chapter 3, a solver for turbidity currents is developed which solves the 2D incompressible Navier-Stokes equations coupled with a transport equation for the particle phase. The Boussinesq approximation is assumed to hold and the velocity field of the particle phase is computed with the equilibrium Eulerian approach, reducing the momentum equation for the particle phase to an algebraic equation. This solver is based on the MEEVC scheme with kinematic Neumann boundary conditions, developed in Chapter 2.

The conservation properties of the MEEVC scheme lead to a very robust and stable discretization with no artificial dissipation of energy. The lock exchange flow is computed for  $Gr = 5 \times 10^6$ , which corresponds with  $Re \approx 2236$ , and comparisons are made with reference results. This numerical test indicates that the general structure of the flow is captured in the most coarse mesh and good agreement is found with the reference results.

Future work can focus on extending this scheme to more complex mathematical models. From a physical point of view, the model used in this solver presents many limitations. The equilibrium Eulerian model is capable of representing essential physics of particle-laden turbulent flows [40]. However, the equilibrium assumption limits computations to cases where particle motion is dominated by the fluid at all times. Therefore, extension to flows with higher particle concentrations than  $\phi > 10^{-3}$  is impossible because particle-particle interaction destroys this equilibrium assumption.

Assuming that the flow is two dimensional has been proved to be another limitation of this model. Necker et al. [43] show that particles remain suspended much longer in the 2D case due to the persistence of energetic vortices over longer periods of time. These structures are less dissipated than in the 3D case, resulting in a slower decay of kinetic energy. Espath et al. [50] compare both 2D and 3D computations with experimental data and conclude that the only feature which the 2D equations can predict in a qualitative manner is the sedimentation rate  $\dot{m}_s$ .

Therefore, if the robustness of the MEEVC scheme is to be exploited for the study of turbidity currents, extensions to fully Eulerian models and to 3D should be considered. The computational power required would be prohibitively high, such that mesh adaptation and turbulence modeling should be considered.

# A

## A COMPATIBILITY CONDITION FOR KINEMATIC NEUMANN BOUNDARY CONDITIONS

When considering the kinematic Neumann boundary conditions, a compatibility condition can be enforced on the vorticity production term such that the total vorticity is conserved. For the case of  $\partial g / \partial t = 0$ , Equation (2.15) reduces to

$$\nu(\nabla \times \omega) \times \vec{n} = -\nabla \bar{p} \times \vec{n} \quad \text{on } \partial\Omega, \quad (\text{A.1})$$

indicating that a sufficient condition for vorticity conservation is that the vorticity production along  $\partial\Omega$  is equal to the gradient of a function  $f$  along  $\partial\Omega$ . Given a closed boundary  $\partial\Omega$  with perimeter  $P$ , a parameterization  $s \in [0, P)$  is defined, see Figure A.1. The compatibility condition for the vorticity along the boundary consists in solving the following 1D ordinary differential equation: given  $\eta(s) = \nu \nabla \times \omega \times \vec{n} \in L^2(\partial\Omega)$ , find  $f(s) \in H^1(\partial\Omega)$  such that

$$\begin{cases} \frac{df}{ds} = \eta, \\ f(0) = f(P) = 0. \end{cases} \quad (\text{A.2})$$

Once  $f$  has been calculated, the derivative of this variable along  $\partial\Omega$  can substitute the vorticity production, such that

$$\langle \omega_h^{k+1}, 1 \rangle = \langle \omega_h^k, 1 \rangle + \Delta t \int_{s=0}^{s=P} \frac{df^{k+\frac{1}{2}}}{ds} ds = \langle \omega_h^k, 1 \rangle. \quad (\text{A.3})$$

### A.1. IMPLEMENTATION

The implementation of this compatibility condition is carried out in two steps:

1. Calculate  $\eta_h$ . Given  $\nabla \times \omega_h \in \text{RT}_N$ , find  $\eta_h \in \text{DG}_N(\partial\Omega)$  such that

$$\langle \eta_h, \hat{q}_h \rangle_{\partial\Omega} = \langle \nabla \times \omega_h \times \vec{n}, \hat{q}_h \rangle_{\partial\Omega} \quad \forall \hat{q}_h \in \text{DG}_N(\partial\Omega), \quad (\text{A.4})$$

where  $\text{DG}_N(\partial\Omega)$  are the discontinuous Lagrange elements of order  $N$  [36] defined along the boundary mesh and  $\langle \cdot, \cdot \rangle_{\partial\Omega}$  is the  $L^2(\partial\Omega)$  inner product.

2. Calculate  $f_h$ . In order to distribute the error along the boundary, the following equation was found to yield the best results: find  $f_h \in \text{CG}_N(\partial\Omega)$  such that,

$$\left\langle \frac{df_h}{ds}, \frac{d\hat{f}_h}{ds} \right\rangle_{\partial\Omega} = \langle \eta_h, \frac{d\hat{f}_h}{ds} \rangle_{\partial\Omega}. \quad (\text{A.5})$$

Equation A.5 is derived from A.1 by differentiating, constructing the weak form and integrating by parts.

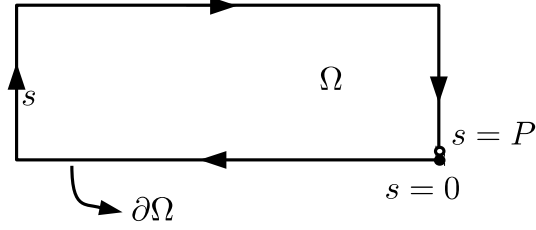


Figure A.1: Parameterization of the closed boundary  $\partial\Omega$  of a domain  $\Omega$ .  $s \in [0, P)$  is the parameter defined along the line and  $P$  the perimeter.

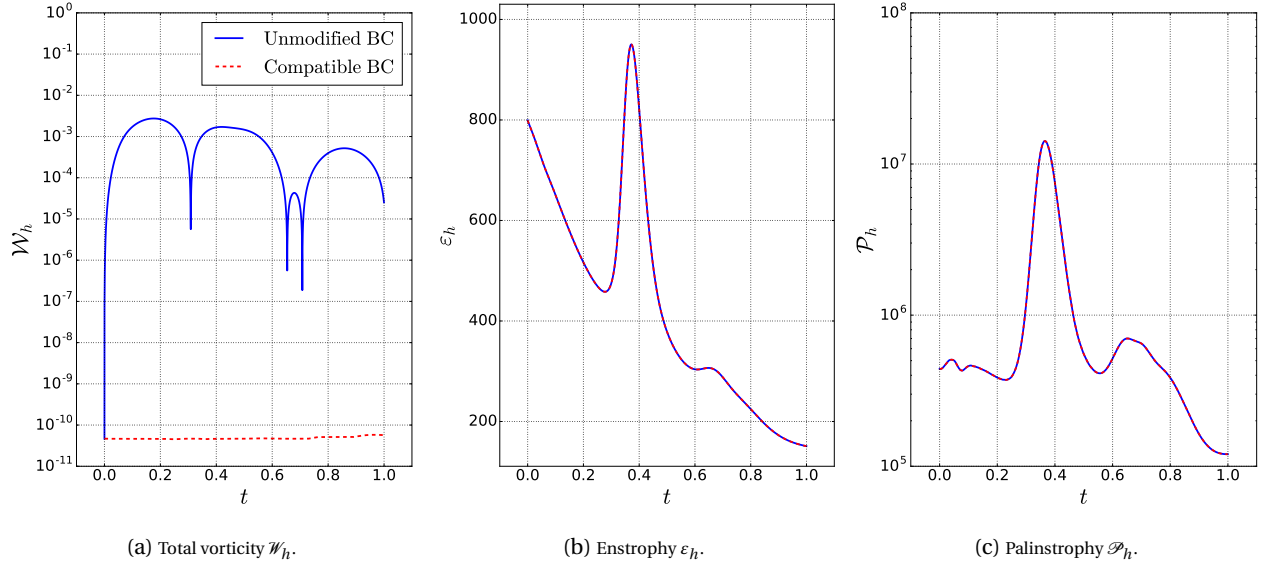


Figure A.2: Variation over time of the total vorticity, enstrophy and palinstrophy. Results have been obtained for the kinematic Neumann boundary conditions with and without compatibility conditions at the boundary.

## A.2. NUMERICAL TEST CASE. THE DIPOLE COLLISION.

Results obtained with and without the compatibility conditions and with the same discretization parameters used in the comparison between solvers of Section 2.7.2 (5210 cells of polynomial degree  $N = 2$  and  $\Delta t = 5 \times 10^{-4}$ ) are shown in Figures A.2 and in Table C.1. These results indicate that, on the one hand, no appreciable differences can be found in the kinetic energy, enstrophy and palinstrophy, and, on the other hand, that the total vorticity is reduced to machine precision values.

# B

## AN ALTERNATIVE $(\vec{u}, \omega, p)$ FORMULATION. COMPARISON WITH THE MEEVC SCHEME.

Chapter 2 concludes that the MEEVC scheme with kinematic Neumann boundary conditions yields the best results with respect to the two other methods proposed. However, this method requires the calculation of an additional vorticity,  $\tilde{\omega}$ , and  $\nabla \times \tilde{\omega} \times \vec{n}$  is not well-defined along  $\partial\Omega$  because  $\tilde{\omega} \in H(\text{curl}, \Omega)$ . This raises the following question: does a  $(\vec{u}, \omega, p)$  formulation with the kinematic condition yield better results than the MEEVC scheme with kinematic Neumann boundary conditions? In order to answer this question, an alternative solver is presented in this chapter and comparisons are made with the MEEVC scheme.

### B.1. DESCRIPTION OF THE ALTERNATIVE $(\vec{u}, \omega)$ FORMULATION. DISCRETIZATION AND CONSERVATION PROPERTIES.

The alternative scheme presented in this chapter combines the momentum equation with the kinematic condition,

$$\begin{cases} \frac{\partial \vec{u}}{\partial t} + \omega \times \vec{u} + \nabla p = -\nu \nabla \times \omega, \\ \nabla \times \vec{u} = \omega, \\ \nabla \cdot \vec{u} = 0. \end{cases} \quad (\text{B.1})$$

If boundary conditions (2.2) are considered, the associated weak form takes the following form,

$$\begin{cases} \text{Find } \vec{u} \in H_0(\text{div}, \Omega), p \in L^2(\Omega) \text{ and } \omega \in H(\text{curl}, \Omega) \text{ such that:} \\ \left\langle \frac{\partial \vec{u}}{\partial t}, \vec{v} \right\rangle + \langle \omega \times \vec{u}, \vec{v} \rangle - \langle p, \nabla \cdot \vec{v} \rangle = -\nu \langle \nabla \times \omega, \vec{v} \rangle, & \forall \vec{v} \in H(\text{div}, \Omega) \\ \langle \omega, \xi \rangle = \langle \vec{u}, \nabla \times \xi \rangle - \int_{\partial\Omega} g(x, t) \xi \, d\Gamma, & \forall \xi \in H(\text{curl}, \Omega) \\ \langle \nabla \cdot \vec{u}, q \rangle = 0, & \forall q \in L^2(\Omega). \end{cases} \quad (\text{B.2})$$

Imposing boundary conditions is straightforward: the restriction on  $H_0(\text{div})$  allows a strong imposition of normal boundary conditions and the boundary integral that arises when integrating by parts in the kinematic condition weakly enforces the tangential component,  $g(x, t) = \vec{u} \times \vec{n}$ . After applying the spatial and temporal discretization, see Sections 2.3 and 2.4, a fully coupled, non-linear system of equations is obtained:

Given  $\bar{u}_h^{k+\frac{1}{2}}$ , find  $(\bar{u}_h^{k+\frac{3}{2}}, \bar{p}_h^{k+1}, \omega_h^{k+1}) \in (\text{RT}_{N,0}, \text{DG}_{N-1}, \text{CG}_N)$  such that:

$$\begin{cases} \left\langle \frac{\bar{u}_h^{k+\frac{3}{2}} - \bar{u}_h^{k+\frac{1}{2}}}{\Delta t}, \bar{v}_h \right\rangle + \langle \omega_h^{k+1} \times \frac{\bar{u}_h^{k+\frac{3}{2}} + \bar{u}_h^{k+\frac{1}{2}}}{2}, \bar{v}_h \rangle - \langle \bar{p}_h^{k+1}, \nabla \cdot \bar{v}_h \rangle = -\nu \langle \nabla \times \omega_h^{k+1}, \bar{v}_h \rangle, & \forall \bar{v}_h \in \text{RT}_{N,0}, \\ \langle \omega_h^{k+1}, \xi_h \rangle = \left\langle \frac{\bar{u}_h^{k+\frac{3}{2}} + \bar{u}_h^{k+\frac{1}{2}}}{2}, \nabla \times \xi_h \right\rangle - \int_{\partial\Omega} \xi_h g^{k+1} \, d\Gamma, & \forall \xi_h \in \text{CG}_N, \\ \langle \nabla \cdot \bar{u}_h^{k+\frac{3}{2}}, q_h \rangle = 0, & \forall q_h \in \text{DG}_{N-1}. \end{cases}$$

In its discrete form, (B.2) conserves mass, kinetic energy and vorticity. Mass and kinetic energy conservation can be proved in the same way as for the MEEVC scheme, see Section 2.6. Vorticity conservation can be proven for  $\xi_h = 1$ , see 2.42. Enstrophy is not conserved, because convection of vorticity is not explicitly described in the discrete system.

## B.2. THE DIPOLE COLLISION

The MEEVC scheme with kinematic Neumann boundary conditions is compared with the alternative  $(\bar{u}, \omega)$  scheme, from now on also denoted “alt”, by computing the dipole collision (see Section 2.7.2) with three meshes of increasing coarseness, with 5210, 3028 and 2052 cells. For all of the computations, the polynomial order of the basis functions is set to  $N = 2$  and the time step to  $\Delta t = 0.001$ .

The detailed contours in the region  $[0.4, 1.0] \times [0, 0.6]$  at  $t = 1$  are presented in Figure B.1, which can be compared with the reference result shown in Figure 2.6d. The variation of the kinetic energy  $\mathcal{K}_h$ , the enstrophy  $\varepsilon_h$ , the palinstrophy  $\mathcal{P}_h$  and the total vorticity  $\mathcal{W}_h$  is plotted in Figure B.2; the values of these variables at  $t = 0.25, 0.5$  and  $0.75$ , together with the two first maxima of  $\varepsilon_h$  and  $\mathcal{P}_h$ , can be found in Tables C.4, C.5 and C.6, where the values given by Bruneau and Clercx [39] are also shown. The values of the wall vorticity for the most refined mesh are plotted in Figure B.3 for  $t = 0.4, 0.6$  and  $1.0$ ; the values given by [39] are also shown.

Better results can be attributed to the MEEVC scheme when considering the refined mesh. On one hand, the contour calculated with the MEEVC scheme, shown in Figure B.1a is more precise than the contour obtained with the alternative scheme. On the other hand, the wall vorticity obtained with the alternative scheme presents large oscillations. Interestingly, for the coarse mesh, the results of the MEEVC scheme clearly deteriorate much more than those of the alternative scheme. This can be appreciated in Figure B.1c and in the variation of enstrophy and palinstrophy, in Figure B.2. Therefore, although the MEEVC scheme yields better results with a refined mesh, the fully coupled alternative scheme seems to be more stable when considering a more under resolved flows.

In order to emphasize the importance of decoupling the discrete system of equations, the computation times required for the dipole collision in the workstation specified in Section 1.5 are plotted over the total degrees of freedom of  $\omega_h$ , denoted  $d_W$ . In this case, a Newton solver is used for the resolution of the non-linear system and, in both cases, the linear systems are solved with a biconjugate gradient stabilized iterative method with an incomplete LU factorization as preconditioner [55]. These results indicate that, in the current setting, computation times are approximately one order of magnitude higher when considering a fully coupled non-linear system.

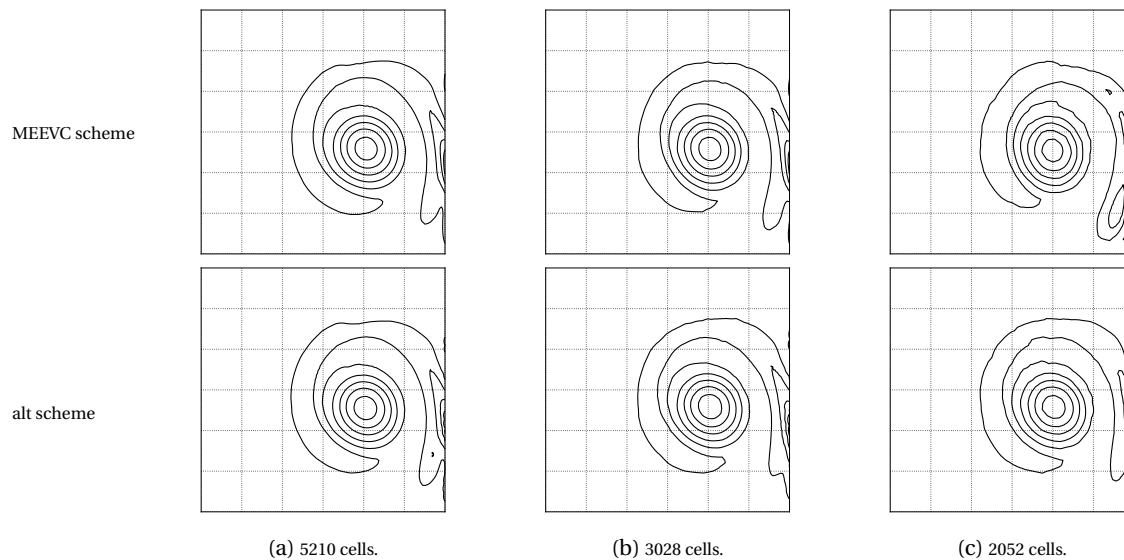


Figure B.1: Vorticity contours for the dipole collision at  $t = 1$  and for the region  $0.4 \leq x \leq 1$  and  $0 \leq y \leq 0.6$ . Computations have been carried out with the MEEVC scheme with kinematic Neumann boundary conditions and with the alternative scheme.

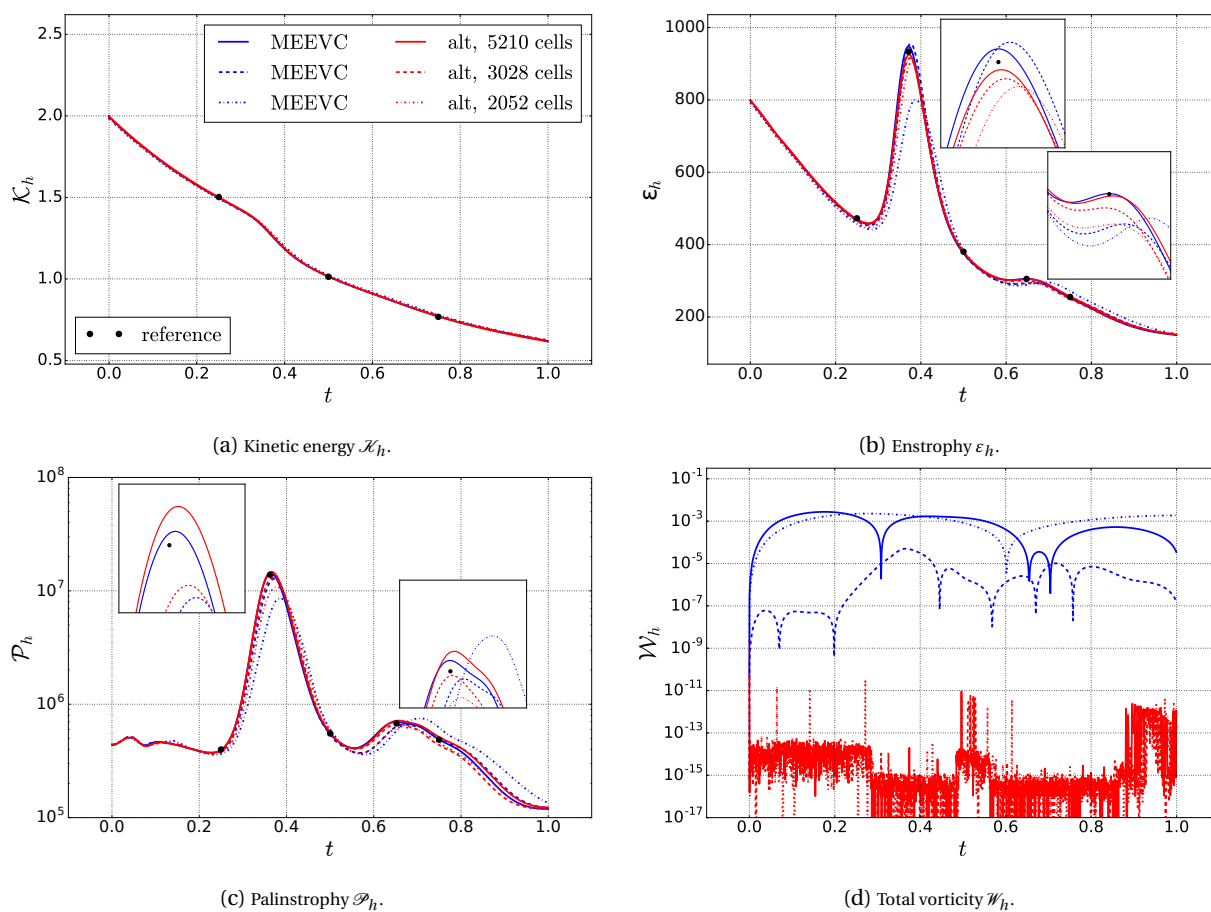


Figure B.2: Variation over time of the kinetic energy, enstrophy, palinstrophy and total vorticity. Details of the two maxima in the enstrophy and the palinstrophy are given.

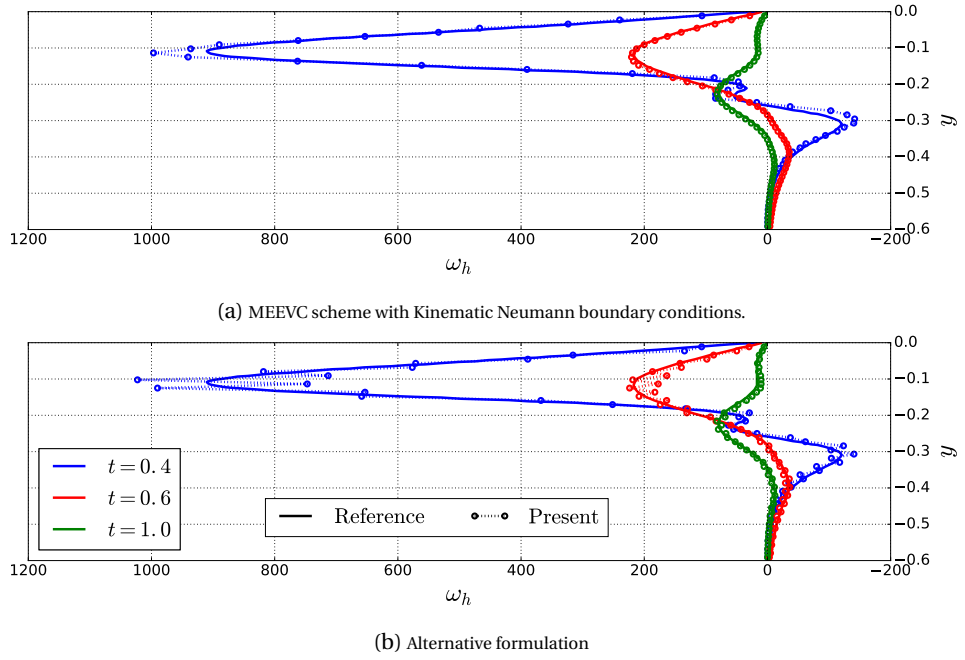


Figure B.3: Vorticity distribution at  $x = 1$  and  $-0.6 \leq y \leq 0$  (lower region of the right wall). The wall vorticity has been plotted for the MEEVC scheme and for the alternative formulation at  $t = 0.4, 0.6$  and  $1$  and is compared to the results given in [39]. These results correspond with the discretization with 5210 cells.

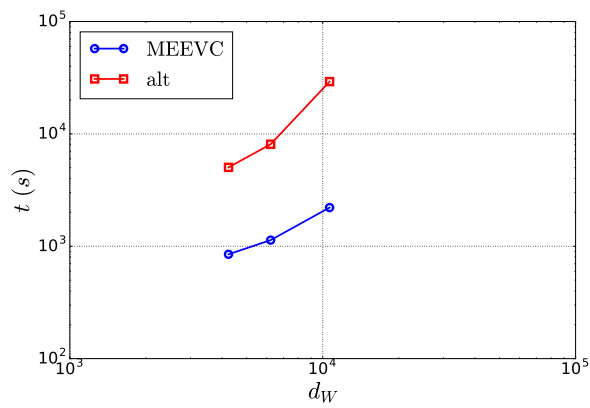


Figure B.4: Variation of the computation time required to solve the dipole collision with the workstation specified in Section 1.5.  $d_W$  represents the number of degrees of freedom of the discrete vorticity.

# C

## TABULATED RESULTS.

### C.1. DIPOLE COLLISION. COMPARISON OF APPROACHES FOR THE PRESCRIPTION OF VORTICITY BOUNDARY CONDITIONS FOR THE MEEVC SCHEME.

Results obtained for the three schemes of Chapter 2 with  $N = 2$  and  $\Delta t = 0.0005$ , together with the compatibility conditions for the kinematic Neumann approach.  $d_W|_\Gamma$  represents the number of degrees of freedom (for  $\omega_h$  in the case of the MEEVC) along the lateral walls.

Table C.1: Values of the kinetic energy  $\mathcal{K}_h$ , enstrophy  $\varepsilon_h$  and palinstrophy  $\mathcal{P}_h$  at  $t = 0.25$  0.5 and 0.75.

Method	$d_W _\Gamma$	$t$	$\mathcal{K}_h$	$\varepsilon_h$	$\mathcal{P}_h$
Kinematic Dirichlet	132	0.25	1.5002	469.7	$3.97 \times 10^6$
		0.5	1.0155	378.1	$5.53 \times 10^6$
		0.75	0.7708	255.2	$5.08 \times 10^6$
Kinematic Neumann	132	0.25	1.5002	467.0	$3.91 \times 10^6$
		0.5	1.0153	378.7	$5.55 \times 10^6$
		0.75	0.7701	254.1	$4.91 \times 10^6$
Kinematic Neumann (compatibility condition)	132	0.25	1.5002	467.0	$3.91 \times 10^6$
		0.5	1.0153	378.7	$5.55 \times 10^6$
		0.75	0.7701	254.1	$4.91 \times 10^6$
Dynamic Neumann	132	0.25	1.5002	469.7	$3.93 \times 10^6$
		0.5	1.0173	389.9	$9.49 \times 10^6$
		0.75	0.7723	260.2	$6.06 \times 10^6$
$N_{SM} = 256$ (reference)	256	0.25	1.5022	472.6	$3.99 \times 10^6$
		0.5	1.0130	380.6	$5.53 \times 10^6$
		0.75	0.7673	255.2	$4.87 \times 10^6$
$N_{FD} = 1024$ (reference)	1024	0.25	1.502	472.7	$3.91 \times 10^6$
		0.5	1.013	380.4	$5.49 \times 10^6$
		0.75	0.767	255.0	$4.73 \times 10^6$

Table C.2: Values of the first two maxima of the enstrophy, which occur at  $t_1$  and  $t_2$ .

Method	$d_W _\Gamma$	$t_1$	$\varepsilon_{h,1}$	$t_2$	$\varepsilon_{h,2}$
Kinematic Dirichlet	132	0.371	923.35	0.650	303.67
Kinematic Neumann	132	0.372	950.33	0.648	306.57
Kinematic Neumann (compatibility condition)	132	0.372	950.33	0.648	306.57
Dynamic Neumann	132	0.374	934.83	0.654	306.42
$N_{SM} = 256$ (reference)	256	0.3711	933.6	0.6479	305.2
$N_{FD} = 1024$ (reference)	1024	0.371	932.8	0.647	305.2

Table C.3: Values of the first two maxima of the palinstrophy, which occur at  $t_1$  and  $t_2$ .

Method	$d_W _\Gamma$	$t_1$	$\mathcal{P}_{h,1}$	$t_2$	$\mathcal{P}_{h,2}$
Kinematic Dirichlet	132	0.365	$1.47 \times 10^7$	0.656	$7.16 \times 10^5$
Kinematic Neumann	132	0.365	$1.42 \times 10^7$	0.652	$7.01 \times 10^5$
Kinematic Neumann (compatibility condition)	132	0.365	$1.42 \times 10^7$	0.652	$7.01 \times 10^5$
Dynamic Neumann	132	0.369	$1.46 \times 10^7$	0.655	$8.10 \times 10^5$
$N_{SM} = 256$ (reference)	256	0.3624	$1.389 \times 10^7$	0.6521	$6.777 \times 10^5$
$N_{FD} = 1024$ (reference)	1024	0.363	$1.296 \times 10^7$	0.653	$6.561 \times 10^5$

## C.2. DIPOLE COLLISION. COMPARISON OF THE MEEVC AND ALT SCHEME.

Results obtained with the MEEVC scheme with kinematic Neumann boundary conditions and with the alternative scheme presented in Appendix B; the computations have been carried out with  $N = 2$  and  $\Delta t = 0.001$ .  $d_W|_\Gamma$  represents the number of degrees of freedom (for  $\omega_h$  in the case of the MEEVC) along the lateral walls.

Table C.4: Values of the kinetic energy  $\mathcal{K}_h$ , enstrophy  $\varepsilon_h$  and palinstrophy  $\mathcal{P}_h$  at  $t = 0.25$  0.5 and 0.75.

Method	$d_W _\Gamma$	$t$	$\mathcal{K}_h$	$\varepsilon_h$	$\mathcal{P}_h$
MEEVC scheme (kinematic Neumann b.c.)	132	0.25	1.4984	468.7	$3.93 \times 10^6$
		0.5	1.0149	376.7	$5.50 \times 10^6$
		0.75	0.7709	253.1	$4.89 \times 10^6$
	100	0.25	1.4954	465.6	$3.82 \times 10^6$
		0.5	1.0142	376.4	$5.44 \times 10^6$
		0.75	0.7741	256.5	$5.00 \times 10^6$
	80	0.25	1.4932	457.1	$3.64 \times 10^6$
		0.5	1.0232	386.0	$6.06 \times 10^6$
		0.75	0.7807	272.0	$6.22 \times 10^6$
alt scheme	132	0.25	1.5017	470.9	$3.93 \times 10^6$
		0.5	1.0157	381.1	$5.61 \times 10^6$
		0.75	0.7699	256.8	$5.14 \times 10^6$
	100	0.25	1.4986	468.4	$3.87 \times 10^6$
		0.5	1.0162	379.5	$5.69 \times 10^6$
		0.75	0.7735	250.2	$4.36 \times 10^6$
	80	0.25	1.4963	460.5	$3.73 \times 10^6$
		0.5	1.0186	381.1	$5.92 \times 10^6$
		0.75	0.7779	251.4	$4.57 \times 10^6$
$N_{SM} = 256$ (reference)	256	0.25	1.5022	472.6	$3.99 \times 10^6$
		0.5	1.0130	380.6	$5.53 \times 10^6$
		0.75	0.7673	255.2	$4.87 \times 10^6$
$N_{FD} = 1024$ (reference)	1024	0.25	1.502	472.7	$3.91 \times 10^6$
		0.5	1.013	380.4	$5.49 \times 10^6$
		0.75	0.767	255.0	$4.73 \times 10^6$

Table C.5: Values of the first two maxima of the enstrophy, which occur at  $t_1$  and  $t_2$ .

Method	$d_W _\Gamma$	$t_1$	$\varepsilon_{h,1}$	$t_2$	$\varepsilon_{h,2}$
MEEVC scheme (kinematic Neumann b.c.)	132	0.372	947.93	0.648	305.39
	100	0.376	955.17	0.664	294.47
	80	0.387	799.97	0.691	296.53
alt scheme	132	0.372	925.28	0.651	304.57
	100	0.375	915.46	0.599	300.76
	80	0.380	906.94	0.599	295.31
$N_{SM} = 256$ (reference)	256	0.3711	933.6	0.6479	305.2
$N_{FD} = 1024$ (reference)	1024	0.371	932.8	0.647	305.2

Table C.6: Values of the first two maxima of the palinstrophy, which occur at  $t_1$  and  $t_2$ .

Method	$d_W _\Gamma$	$t_1$	$\mathcal{P}_{h,1}$	$t_2$	$\mathcal{P}_{h,2}$
MEEVC scheme (kinematic Neumann b.c.)	132	0.364	$1.41 \times 10^7$	0.651	$6.99 \times 10^5$
	100	0.373	$1.27 \times 10^7$	0.669	$6.63 \times 10^5$
	80	0.385	$8.59 \times 10^6$	0.706	$7.50 \times 10^5$
alt scheme	132	0.366	$1.47 \times 10^7$	0.656	$7.18 \times 10^5$
	100	0.369	$1.39 \times 10^7$	0.654	$6.69 \times 10^5$
	80	0.377	$1.08 \times 10^7$	0.665	$6.28 \times 10^5$
$N_{SM} = 256$ (reference)	256	0.3624	$1.389 \times 10^7$	0.6521	$6.777 \times 10^5$
$N_{FD} = 1024$ (reference)	1024	0.363	$1.296 \times 10^7$	0.653	$6.561 \times 10^5$



# BIBLIOGRAPHY

- [1] E. Meiburg and B. Kneller, *Turbidity currents and their deposits*, Annual Review of Fluid Mechanics **42**, 135 (2010).
- [2] E. Meiburg, S. Radhakrishnan, and M. Nasr-Azadani, *Modeling gravity and turbidity currents: computational approaches and challenges*, Applied Mechanics Reviews **67**, 040802:1 (2015).
- [3] C. J. Budd and M. D. Piggott, *Geometric integration and its applications*, Handbook of Numerical Analysis **11**, 35 (2003).
- [4] R. W. C. P. Verstappen and A. E. P. Veldman, *Symmetry-preserving discretization of turbulent flow*, Journal of Computational Physics **187**, 343 (2003).
- [5] L. G. Rebholz, *Conservation laws of turbulence models*, Journal of Mathematical Analysis and Applications **326**, 33 (2007).
- [6] J. B. Perot, *Discrete conservation properties of unstructured mesh schemes*, Annual Review of Fluid Mechanics **43**, 299 (2011).
- [7] F. Harlow and J. Welch, *Numerical calculation of time-dependent viscous incompressible flow of fluid with free surface*, Physics of Fluids **8**, 2182 (1965).
- [8] P. Bochev, *A discourse on variational and geometric aspects of stability of discretizations*, in *33rd Computational Fluid Dynamics Lecture Series*, ISSN0377-8312, edited by H. Deconinck (VKI LS, Von Karman Institute for Fluid Dynamics, 2003-05).
- [9] P. Bochev and M. Hyman, *Principles of mimetic discretizations*, in *IMA*, Vol. 142 (Springer Verlag, 2006).
- [10] A. Palha, P. P. Rebelo, R. Hiemstra, J. Kreeft, and M. I. Gerritsma, *Physics-compatible discretization techniques on single and dual grids, with application to the Poisson equation of volume forms*, Journal of Computational Physics **257**, 1394 (2014).
- [11] A. Palha and M. I. Gerritsma, *A mass, energy, enstrophy and vorticity conserving (MEEVC) mimetic spectral element discretization for the 2D incompressible Navier-Stokes equations*, Journal of Computational Physics **328**, 200 (2017).
- [12] J. E. Simpson, *Gravity Currents. In the environment and in the laboratory*, 2nd ed. (Cambridge University Press, 1997).
- [13] C. Geuzaine and J. Remacle, *Gmsh: a three-dimensional finite element mesh generator with built-in pre- and post-processing facilities*, International Journal for Numerical Methods in Engineering **79**, 1309 (2009).
- [14] A. Logg, G. N. Wells, and J. Hake, *DOLFIN: a C++/Python finite element library*, in *Automated Solution of Differential Equations by the Finite Element Method*, Lecture Notes in Computational Science and Engineering, Vol. 84, edited by A. Logg, K. Mardal, and J. Hake (Springer, 2012) pp. 173–225.
- [15] F. Brezzi and M. Fortin, *Mixed and Hybrid Finite Element Methods*, Springer Series in Computational Mathematics 44 No. 15 (Springer, 1991).
- [16] P. M. Gresho, *Incompressible fluid dynamics: some fundamental formulation issues*, Annu. Rev. Fluid Mech **23**, 413 (1991).
- [17] T. B. Gatski, *Review of incompressible fluid flow computations using the vorticity-velocity formulation*, Applied Numerical Mathematics **7**, 227 (1991).
- [18] J. Z. Wu and J. M. Wu, *Vorticity Dynamics on Boundaries*, Advances in Applied Mechanics **32**, 119 (1996).

- [19] M. J. Lighthill, *Chapter II. Introduction: Boundary Layer Theory*, in *Laminar Boundary Layers*, edited by L. Rosenhead (Oxford at the Clarendon Press, 1963).
- [20] A. J. Chorin, *Vortex sheet approximation of boundary layers*, *Journal of Computational Physics* **27**, 428 (1978).
- [21] J. C. Wu, *Fundamental solutions and numerical methods for flow problems*, *International Journal for Numerical Methods in Fluids* **4**, 185 (1984).
- [22] B. R. Morton, *The generation and decay of vorticity*, *Geophys. Astrophys. Fluid Dyn.* **28**, 277 (1984).
- [23] J. Z. Wu, H. Y. Ma, and M. D. Zhou, *Vorticity and Vortex dynamics* (Springer, Berlin, 2006).
- [24] J. Z. Wu, X. H. Wu, H. Y. Ma, and J. M. Wu, *Dynamic vorticity condition: Theoretical analysis and numerical implementation*, *International Journal for Numerical Methods in Fluids* **19**, 905 (1994).
- [25] C. Taylor and P. Hood, *A numerical solution of the Navier-Stokes equations using the finite element technique*, *Computers & Fluids* **1**, 73 (1973).
- [26] G. Guevremont, W. Habashi, and M. Hafez, *Finite element solution of the Navier-Stokes equations by a velocity-vorticity method*, *International Journal for Numerical Methods in Fluids* **11**, 611 (1990).
- [27] G. Guevremont, W. Habashi, P. Kotiuga, and M. Hafez, *Finite Element Solution of the 3D Compressible Navier-Stokes Equations by a Velocity-Vorticity Method*, *Journal of Computational Physics* **107**, 176 (1993).
- [28] M. A. Olshanskii, T. Heister, L. G. Rebholz, and K. J. Galvin, *Velocity - vorticity - helicity formulation and a solver for the Navier-Stokes equations*, *Journal of Computational Physics* **229**, 4291 (2010).
- [29] H. K. Lee, M. A. Olshanskii, and L. G. Rebholz, *On error analysis for the 3D Navier-Stokes equations in velocity-vorticity-helicity form*, *SIAM J. Numer. Anal.* **49**, 711 (2011).
- [30] M. Benzi, M. A. Olshanskii, L. G. Rebholz, and Z. Wang, *Assessment of a vorticity based solver for the Navier-Stokes equations*, *Comput. Methods Appl. Mech. Engrg.* **247-248**, 216 (2012).
- [31] M. A. Olshanskii, T. Heister, L. G. Rebholz, and K. J. Galvin, *Natural vorticity boundary conditions on solid walls*, *Computer Methods in Applied Mechanics and Engineering* **297**, 18 (2015).
- [32] T. Heister, M. A. Olshanskii, and L. G. Rebholz, *Unconditional long-time stability of a velocity-vorticity method for the 2d navier-stokes equations*, *Numer. Math.* **135**, 143 (2017).
- [33] J. Trujillo and G. Karniadakis, *A Penalty Method for the Velocity-Vorticity Formulation*, *Journal of Computational Physics* **149**, 32 (1999).
- [34] S. Charnyi, T. Heister, M. A. Olshanskii, and L. G. Rebholz, *On conservation laws of Navier-Stokes Galerkin discretizations*, *Journal of Computational Physics* **337**, 289 (2017).
- [35] S. Brenner and R. Scott, *The mathematical theory of finite element methods*, (2007).
- [36] C. Kirby, A. Logg, M. E. Rognes, and A. R. Terrel, *Common and unusual finite elements*, in *Automated Solution of Differential Equations by the Finite Element Method*, *Lecture Notes in Computational Science and Engineering*, Vol. 84 (Springer, 2012) pp. 95–119.
- [37] E. Hairer, C. Lubich, and G. Wanner, *Geometric numerical integration: structure-preserving algorithms for ordinary differential equations*, Vol. 31 (Springer Science & Business Media, 2006).
- [38] R. Temam, *Navier Stokes Equations* (Amsterdam-New York-Oxford, 1977).
- [39] H. J. H. Clercx and C. H. Bruneau, *The normal and oblique collision of a dipole with a no-slip boundary*, *Computers & Fluids* **35**, 245 (2006).
- [40] J. Ferry and S. Balachandar, *A fast Eulerian method for disperse two-phase flow*, *International Journal of Multiphase Flow* **27**, 1199 (2001).

- [41] C. Härtel, L. Kleiser, M. Michaud, and C. F. Stein, *A direct numerical simulation approach to the study of intrusion flows*, Journal of Engineering Mathematics **32**, 103 (1997).
- [42] C. Härtel, E. Meiburg, and F. Necker, *Analysis and direct numerical simulation of the flow at a gravity-current head. part 1. flow topology and front speed for slip and no-slip boundaries*, Journal of Fluid Mechanics **418**, 189 (2000).
- [43] F. Necker, C. Härtel, L. Kleiser, and E. Meiburg, *High-resolution simulations of particle-driven gravity currents*, International Journal of Multiphase Flow **28**, 279 (2002).
- [44] F. Necker, C. Härtel, L. Kleiser, and E. Meiburg, *Mixing and dissipation in particle-driven gravity currents*, Journal of Fluid Mechanics **545**, 339 (2005).
- [45] F. Blanchette, M. Strauss, E. Meiburg, B. Kneller, and M. E. Glinsky, *High-resolution numerical simulations of resuspending gravity currents: Conditions for self-sustainment*, Journal of Geophysical Research **110**, C12022 (2005).
- [46] M. I. Cantero, S. Balachandar, M. H. Garcia, and J. P. Ferry, *Direct numerical simulations of planar and cylindrical density currents*, Journal of Applied Mechanics **73**, 923 (2006).
- [47] J. E. Birman, V. K. Martin and E. Meiburg, *The non-boussinesq lock-exchange problem. part 2. high-resolution simulations*, Journal of Fluid Mechanics **537**, 125 (2005).
- [48] M. I. Cantero, S. Balachandar, and M. H. Garcia, *An eulerian-eulerian model for gravity currents driven by inertial particles*, International Journal of Multiphase Flow **34**, 484 (2008).
- [49] S. D. Parkinson, J. Hill, M. D. Piggott, and P. A. Allison, *Direct numerical simulations of particle-laden density currents with adaptive, discontinuous finite elements*, Geoscientific Model Development **7**, 1945 (2014).
- [50] L. F. R. Espath, L. C. Pinto, S. Laizet, and J. H. Silvestrini, *Two- and three-dimensional direct numerical simulation of particle-laden gravity currents*, Computers and Geosciences **63**, 9 (2014).
- [51] S. Elghobashi, *On predicting particle-laden turbulent flows*, Applied Scientific Research **52**, 309 (1994).
- [52] S. Balachandar, *A scaling analysis for point-particle approaches to turbulent multiphase flows*, International Journal of Multiphase Flow **35**, 801 (2009).
- [53] D. D. Joseph, T. S. Lundgren, R. Jackson, and D. A. Saville, *Ensemble averaged and mixture theory equations for incompressible fluid—particle suspensions*, International journal of multiphase flow **16**, 35 (1990).
- [54] J. C. André and M. Lesieur, *Influence of helicity on the evolution of isotropic turbulence at high reynolds number*, Journal of Fluid Mechanics **81**, 187 (1977).
- [55] Y. Saad, *Iterative methods for sparse linear systems*, (2003).